UiT The Arctic University of Norway

Faculty of Science and Technology
Department of Geoscience

Characteristics and failure mechanisms of the unstable rock slope Dusnjárga

Interpreting failure mechanisms at Dusnjárga from slope morphology, structural analysis and InSAR/dGNSS surface displacement

Simen Bekkevoll

Master's thesis in Geology, GEO-3900, May 2022

Cover photo from Dusnjárgas head domain by Simen Bekkevoll

Abstract

Large slowly creeping rock slope deformations, with an annual displacement in the range of millimeters to centimeters, have been prone to rapid catastrophic failures in the past. This master thesis focuses on the unstable rock slope of Dusnjárga in Northern Norway. A sudden rapid failure of Dusnjárga would pose a threat to the local society in Lille Altafjord and Burfjord, due to potential secondary effects such as displacement waves. The Geological Survey of Norway (NGU) has identified Dusnjárga as a location of interest as it shows evidence of active gravitational-driven deformation with a large backscarp visible at the head of the slope and well-defined lateral limits. Dusnjárga differs from other nearby unstable rock slopes with a flowing-type geometry. However, to properly assess its hazard, a detailed investigation of the rock slope is needed, to understand its mechanical and kinematic characteristics.

A two-dimensional (2D) satellite-based method, based on Synthetic Aperture Radar Interferometry (InSAR) from two satellite geometries (ascending and descending orbits), was combined with morphological and structural analyses to assess the kinematics and failure mechanisms of the slope. The 2D InSAR results were decomposed into vertical and horizontal velocities along terrain profiles and compared with simple finite element simulations of known failure mechanisms. Additionally, 3D InSAR was utilized for a certain part of the slope, by combining InSAR from the two satellite geometries with a ground-based radar (GB-radar). The 3D InSAR provides information about slope velocities in three dimensions, while also being more accurate due to the integration of three complementary Line of Sight (LOS) instead of two.

Displacement data from differential Global Navigation Satellite System (dGNSS) and InSAR, indicates that the slope can be separated into an inactive head domain and an active rock slope underneath. Although the head domain is generally inactive, it contains a minor local block with a noticeable displacement rate between 7–15 mm/year. The active rock slope deformation has a peak velocity of 15–20 mm/year in its central domain, with velocities decreasing downslope until it is halved at the toe domain. From examining morphological structures and carrying out structural analyses, the active parts of the rock slope are found to be joint- and foliation-controlled. The foliation and a single joint set are controlling the morphologic

elements oriented perpendicular to the slope movement, such as the backscarp, while two sub-vertical joint sets are controlling the lateral limits and spatial lateral variations in velocity.

From comparing the 2D InSAR velocity vectors to simple finite element simulations, the rear rupture surface was interpreted to have a roto-translational failure mechanism. The controlling structure of the basal rupture surface was proposed to be the foliation, as velocity vectors follows the orientation of the foliation and strength tests revealed anisotropic properties. The foliation at Dusnjárga follows both an anticlinal and synclinal fold, causing diverse stress-regimes and an upwards moving compressed toe area. The rock slope deformation has been classified as an irregular complex bi-planar compound slide. A hazard rating of medium was proposed, but the special geometry at the toe domain could suggest that Dusnjárga will have increased stabilisation in the future.

Acknowledgements

First, I would like to thank my main supervisor at the University of Tromsø (UiT) Louise Mary Vick for all the helpful advice, readthroughs, and motivation at times when productivity slowed down. I would like to thank my co-supervisor Martina Böhme from the Geological Survey of Norway (NGU) who gave me valuable guidance when I visited NGU in Trondheim and kick-started my writing. I would also like to thank my other co-supervisor Tom Rune Lauknes from the Norwegian Research Center (NORCE), who helped me with all my InSAR related questions.

Thanks to Line Rouyet (NORCE) as my unofficial fourth supervisor, who helped me with both InSAR related challenges and with readthroughs. And thanks to Jakob Grahn (NORCE) for helping me getting started with the InSAR GIS-tool.

Thanks to Marie Bredal (NGU) who helped me with the three-dimensional InSAR and to Pierrick Nicolet (NGU) for helping me with the photogrammetry.

Thanks to my co-students Emilie and Andreas for the great field trips to Dusnjárga, and for giving me company during the numerous climbs up the mountain.

Lastly, I would like to thank Lisa, who made my time as a student in Tromsø so much better than expected and who supports me no matter what.

Simen Bekkevoll

Tromsø, May 2022

Table of Contents

List of abbreviations

InSAR - Interferometric Synthetic Aperture Radar

LOS – Line of Sight

GNSS – Global Navigation Satellite System

dGNSS – differential Global Navigation Satellite System

TTOP – temperatures at the top layer of permafrost or the bottom layer of a seasonal frost

SIP – Seiland Igneous Province

SIS – Scandinavian Ice Sheet

GIS – Geographical Information System

RSD – Rock Slope Deformation

MSD – Mountain Slope Deformation

CSD – Combined Surface Displacement

DEM – Digital elevation model

LGM – Last Glacial Maximum

M.a.s.l. – Meters above sea level

M.b.s.l. – Meters below sea level

GB-radar – Ground Based radar

GPS – Global Positioning System

1 Introduction

1.1 Motivation

In Norway, documented deposits from large prehistoric rock avalanches has shown that the western coastline of Norway, with its steep mountains and deep fjords, are most prone such events (Blikra et al., 2002, Braathen et al., 2004). Rock avalanches in Norway has historically had fatal consequences, both from the initial impact from the rock mass, and from secondary effects. Generated displacement waves in fjords and damming of valleys with sudden bursts and flooding, are some of the possible secondary effects (Furseth, 2006, Hermanns et al., 2012a). Based on statistical data, large catastrophic rock avalanches is expected to happen in the near future as well (Braathen et al., 2004, Hermanns et al., 2012b).

In Norway, the municipalities have a responsibility to protect its inhabitants from natural disasters such as rock avalanches, supported by the Norwegian Water Resources and Energy Directorate (NVE). NGU also contributes to this work by monitoring, mapping, databases and expertise (Hermanns et al., 2012a). As NGU has an obligation in providing geological information to the Norwegian society, a systematic mapping of unstable rock slopes in Norway is being conducted by NGU in collaboration with NVE. Mapping of these slopes involves a hazard analysis in which the probability of failure, and consequence (if necessary) is being evaluated (Hermanns et al., 2012b). To assess failure probability of a large rock slope, mapping of internal structures, morphological elements and spatial variations in displacement rates are usually needed (Hermanns et al., 2012b, Vick et al., 2020). Displacement rates can be measured with in-field methods, or by remote sensing like InSAR and GNSS (Hermanns et al., 2012b).

Dusnjárga is one of the unstable rock slopes identified in NGU's systematic mapping, but has until now only been roughly mapped, without extensive research regarding kinematic characteristics and failure mechanisms (Redfield et al., 2011, Blau, 2020). Dusnjárga clearly show gravitational driven deformation with its distinct morphological features. A comprehensive analysis of the structural, morphological and kinematic characteristics of Dusnjárga will contribute to NGUs systematic mapping of unstable rock slopes in Norway and give valuable information to nearby settlements in Lille Altafjord and Burfjord about the

potential hazard. Additionally, a study of Dusnjárga will contribute to the general knowledge regarding large unstable rock slopes in Norway.

1.2 Objectives

The objective of this study is to determine the rock slope failure mechanisms at Dusnjárga, by investigating slope morphology, structural geology and surface displacements from InSAR and dGNSS data. Multiple methods, both based on remote sensing and fieldwork activities, will be utilized to exploit their complementarities. A detailed morphological mapping of the deformed rock slope will be performed and combined with 2D InSAR data to interpret kinematics of the rock slope. Failure mechanisms are then to be interpreted from 2D InSAR kinematics, aided by to simple finite element simulations of known failure types. 3D InSAR data from three different geometries (spaceborne and ground based InSAR) will further strengthen the understanding of displacement rates and showcase local variations in velocity and orientation. To achieve the main objectives of the study, the study includes secondary objectives fulfilled by performing six specific tasks:

I. Provide a theory chapter on large unstable rock slopes and their failure mechanisms, with a focus on characteristics that applies to Dusnjárga.
II. Produce a complete morphostructural map of Dusnjárga above and below the waterline.
III. Produce a detailed DEM of the transition zone of the rock slope with a UAV, and map morphostructures at a higher resolution in this area.
IV. Analyse existing and collected structural data from the area of interest, and summarize the findings with a stereonet spatial analysis
V. Generate and interpret 2D and/or 3D InSAR maps of the site to document the magnitude, distribution and orientation of the movement.
VI. Produce detailed cross-sections of the rockslide by linking movement vectors from InSAR with morphostructures. Interpret where zones of compression/extension are occurring in the slope and suggest which failure mechanism is taking place in Dusnjárga

2 Theoretical background

2.1 Rock-slope failures

Rock-slope failures can be defined as gravitational mass movement of rock-masses down a mountain slope, while rock-slope instabilities can be identified as the source leading to these failures (Böhme et al., 2011, Braathen et al., 2004). The failure of a large unstable rock slope cannot be controlled or negated by physical measures and can have catastrophic consequences due to its potentially enormous size, velocity and reach (Hermanns and Longva, 2012). In addition to the destructive powers of the initial failure, secondary effects such as da damming of rivers and landslide-triggered displacement waves (tsunamis) (Clague and Evans, 1994, Tappin, 2010, Evans et al., 2011) can be very detrimental.

2.1.1 Classification of landslide types

Landslides are essentially gravitational mass movements of different sized particles, such as boulders, rocks, gravel or soil moving down-slope (Cruden, 1991). The most known classification of landslides comes from Varnes (1978), which later had new concepts added in Cruden and Varnes (1996), and an update with Hungr et al., (2014). In the updated classification system, there is a total of 32 classes of landslides, each with their own formal definition.

Landslides are often comprised of several stages of deformation. There are pre-failure deformations, syn-failure deformations, and post-failure displacements (Hungr et al., 2014). Failure of a slope can be described as the most significant movement within the slide, which usually corresponds to the first completement of a fully developed rupture surface, however a unstable rock slope does not necessarily have to lead to a single major failure, but can culminate in several smaller failures over time, or even no major failure at all (Leroueil et al., 1996, Hungr et al., 2014, Agliardi et al., 2001). As the deformation of landslides develops with time, many landslides experience several episodes of movement with different characteristics, where the movement is separated by periods of inactivity of variable length (Hungr et al., 2014).

Table 1: Landslide classification system by Varnes (1978) and later updated by Hungr et al. (2014). Those in italics means that only one is used at a time. "" means that the landslide type usually reaches extremely rapid velocities, as defined by Cruden and Varnes (1996), while the other landslide-types usually move at the range of extremely slow to very rapid.*

Type of movement	Rock	Soil
Fall	1. *Rock/ice* fall*	2. *Boulder/debris/silt* fall*
Topple	3. Rock block topple*	5. *Gravel/sand/silt* topple*
	4. Rock flexural topple	
Slide	6. Rock rotational slide	11. *Clay/silt* rotational slide
	7. Rock planar slide*	12. *Clay/silt* planar slide
	8. Rock wedge slide*	13. *Gravel/sand/debris* slide*
	9. Rock compound slide	14. *Clay/silt* compuond slide
	10. Rock irregular slide*	
Spread	15. Rock slope spread	16. *Sand/silt* liquefaction spread*
		17. Sensitive clay spread*
Flow	18. *Rock/ice* avalance*	19. *Sand/silt/debris* dry flow
		20. *Sand/silt/debris* flowside*
		21. Sensitive clay flowside*
		22. Debris flow*
		23. Mud flow*
		24. Debris flood
		25. Debris avalanche*
		26. Earthflow
		27. Peat flow
Slope deformation	28. Mountain slope deformation	30. Soil slope deformation
	29. Rock slope deformation	31. Soil creep
		32. Solifluction

Landslides are also categorized based on velocity. One can characterize landslides based on their velocity from different stages of their process, as suggested by Cruden and Varnes (1996). Since a landslide might have several reactivations and complex structures on its path downslope, which can change its identity, it can be hard to categorize. To make it easier, one can identify the main aspects of a landslide and categorize it based on the mean velocities of the most representable parts of the landslide (Hungr et al., 2014).

Table 2: Landslide velocity classification showing seven velocity-classes, ranging from extremely slow to extremely rapid. Adapted from Hungr et al., (2014),(Cruden et al., 1996).

Velocity class	Description	Velocity(mm/s)	Typical velocity
7.	Extremely rapid	$5x10^{3}$	5 m/s
6.	Very rapid	$5x10^{1}$	3 m/m
5.	Rapid	$5x10^{-1}$	1,8 m/h
4.	Moderate	$5x10^{-3}$	13 m/month
3.	Slow	$5x10^{-5}$	1,6 m/year
2.	Very slow	$5x10^{-7}$	16 mm/year
1.	Extremely slow	$<5x10^{-7}$	<16 mm/year

Slope deformation

When dealing with slope deformations, it can be challenging to differ between Mountain Slope Deformations (MSDs) and Rock Slope Deformations (RSDs), both can be large in size, but they have some characteristics that can separate one from the other (Hungr et al., 2014). MSDs are large scale deformations that were first described by A. Heim (1932).

From the Varnes classification system MSDs are described as large-scale gravitational deformations with steep mountainsides that displays morphologic structures such as scarps, trenches, bulges, cracks, and benches, without a fully defined rupture surface. Rate of movement is ranging from extremely slow to unmeasurable (Hungr et al., 2014).

RSDs are slow to extremely slow-moving deformations of valley or hill slopes without well-defined rupture surfaces. They are deep seated and tend to display sagging of slope crests and development of cracks and faults (Hungr et al., 2014). Main differences between RSDs and MSDs are the scale. RSDs can be within the range of a few tens and up to a couple of hundreds of meters in hight, while also often occurring in weak rock. MSDs are large scale deformations that often show complex structural deformations. These large slope deformations, are often described with the term: Deep Seated Gravitational Slope Deformations (DSGSDs), which typically has a considerable thickness and can extend along the whole mountain slope, from the top ridge to the bottom of the valley/fjord (Agliardi et al., 2012, Crosta et al., 2013).

Structurally controlled basal and rear rupture surface

During the process of slope deformation, rupturing fractures develops underneath, at the rear and laterally to the deforming body. These fractures develop based on the orientation and intensity of pre-existing structural features such as foliation, joints, folds and faults (fig. 1) (Glastonbury and Fell, 2010). Detailed descriptions and classification of these internal pre-existing structures in the rock can therefore be used to understand the overall deformation in a rock slope.

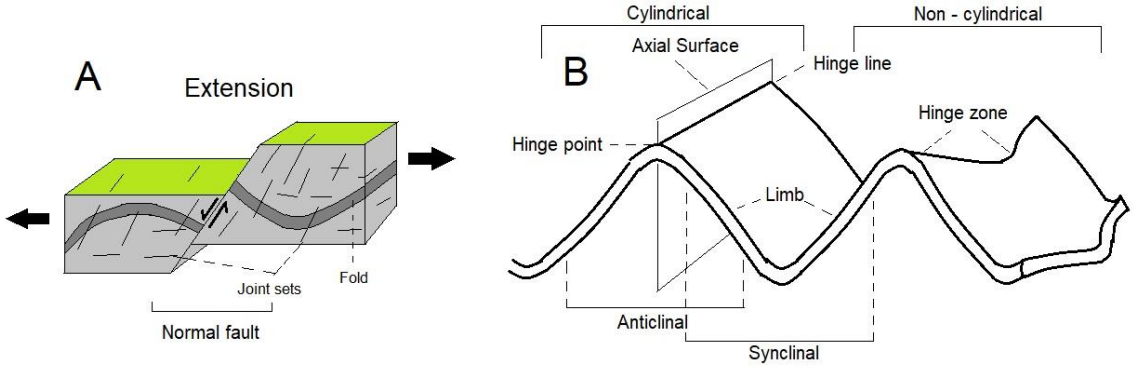

Figure 1: A: An example of structures appearing in rock bodies which can be useful to examine during geological mapping, inspired by (Glastonbury and Fell, 2010). B: An example of fold characteristics. Inspired by (Nabavi and Fossen, 2021)

As demonstrated by Glastonbury and Fell (2000), structures, composition and geometry of a rock slope can subsequently determine kinematic mechanisms within the slope. Geometry of the basal rupture surface, developed between underlying intact bedrock and the displaced moving body above, can be used to describe slope deformations, ranging from simple planar translational to highly complex multi-mechanism failures (fig. 2) (Stead and Wolter, 2015), as illustrated by (Braathen et al., 2004, Hermanns and Longva, 2012, Vick et al., 2020).

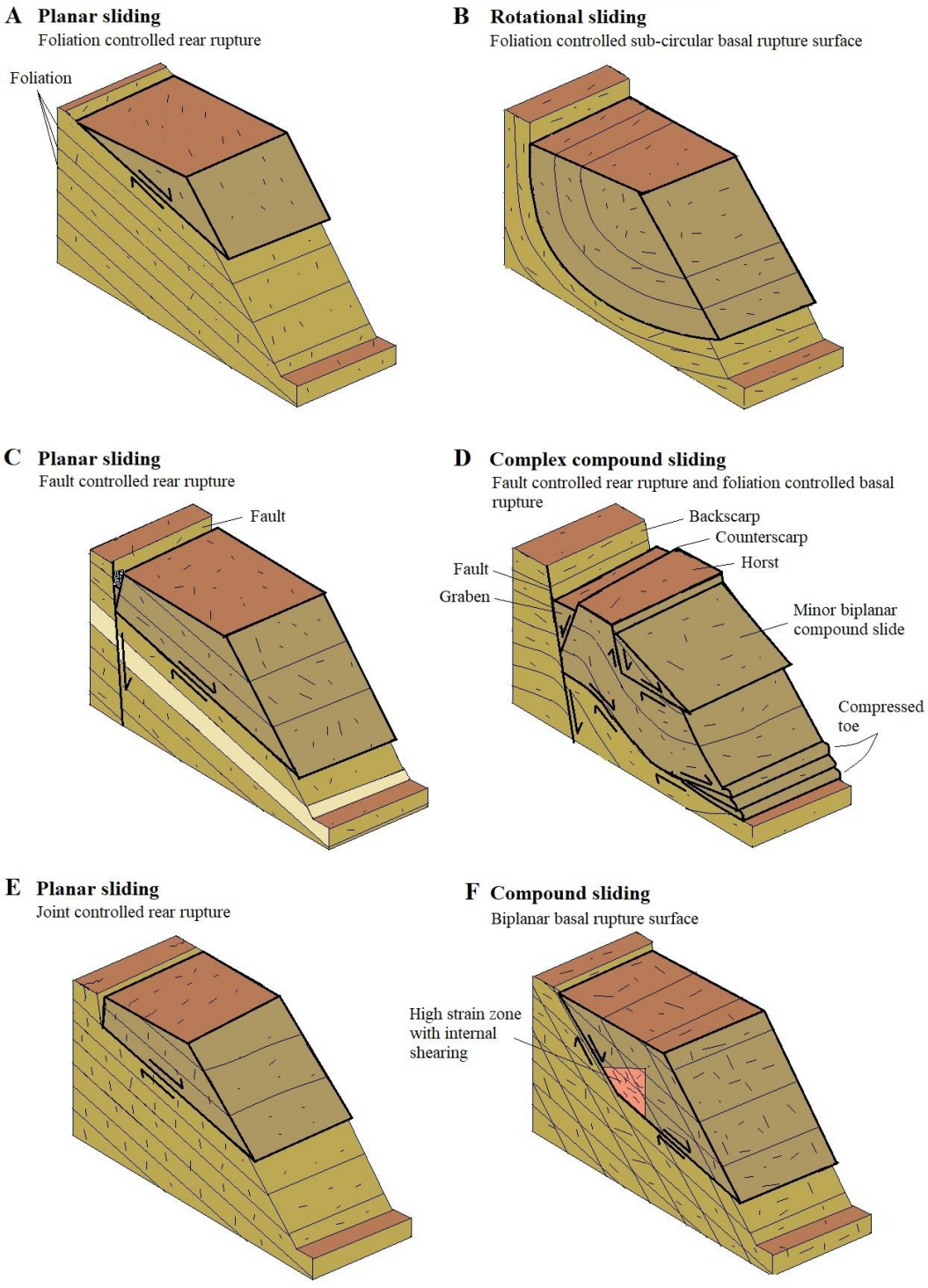

Figure 2: Examples of structurally controlled slope deformations. A, C and E: Translational planar slides with different structural control at rear rupture. B: Rotational slide along a sub-circular basal rupture surface. D: Complex compound slide with fault controlled rear rupture, which transitions into an irregular foliation controlled basal rupture plane. F: Biplanar compound sliding where the basal rupture surface goes along two planes with different inclination. Inspired by: (Glastonbury and Fell, 2000, Vick et al., 2020)

2.1.2 Unstable rock slopes in Troms and Finnmark County

Unstable rock slopes in Norway have been studied for quite some time, but only during the last 16 years has there been a systematic mapping of these rock slopes (fig. 3), implemented by NGU. The purpose of systematic mapping is to characterise unstable rock slopes that are prone to failure, so that future catastrophic events can be identified beforehand and necessary measures can be taken (Hermanns et al., 2013).

Southwestern and Northern Norway have the highest density of unstable rock slopes, due to being a post-glacial landscape with tall alpine mountains diving steeply into the deep fjords below. Naturally this makes the western and northern parts of Norway the most examined areas come unstable rock slopes (Vick et al., 2020). In Troms and Finnmark county alone there has been mapped over 130 unstable rock slopes during the last years of systematic mapping (NGU, 2022a). Linking inherited bedrock structures with failure mechanisms of unstable rock slopes has mostly been done in studies of the southwestern parts of Norway (Henderson and Saintot, 2011, Saintot et al., 2011, Penna et al., 2017). Studies regarding this topic has been done for Northern Norway as well, but they are more limited (Braathen et al., 2004, Vick et al., 2020).

Many unstable rock slopes in Troms and Finnmark are dominated by the metamorphic rock mica schist, a medium grade rock with relatively low strength and anisotropic (Vick et al., 2020). Majority of the unstable rock slopes are also facing west on moderate to steep slopes (20–35°) which is thought to be explained by the structural properties of the thrusted nappes and the associated orientation of major fault systems (Bunkholt et al., 2013, Vick et al., 2020). Based on its lithology, a mafic metagabbro of high strength, and a south-east facing slope, Dusnjárga does not have common characteristics compared to other unstable rock slope in Troms and Finnmark,

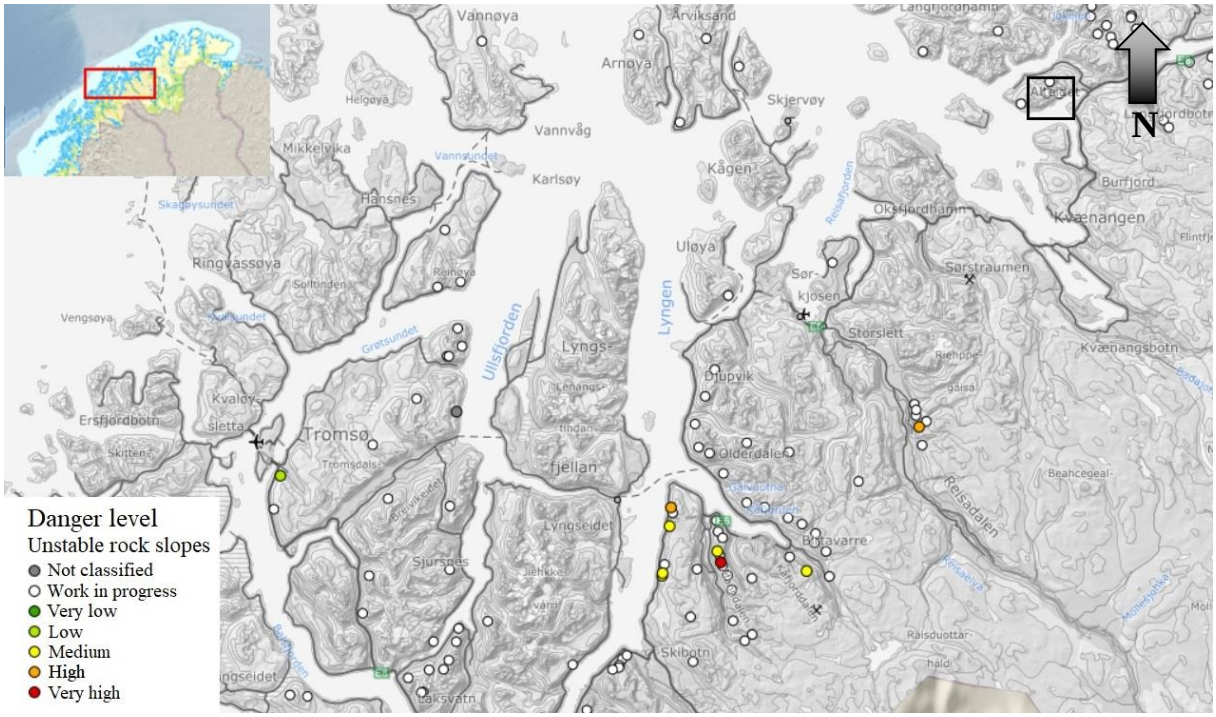

Figure 3: Topographic map of Troms and Finnmark county, displaying unstable rock slopes mapped by NGU, with interpreted danger levels. Red square in upper left corner shows area on a larger scale. Black square shows the location of Dusnjárga. A lot of mapped unstable rock slopes in Troms and Finnmark county has not been investigated thoroughly yet and is being worked on. Adapted from: (NGU, 2022b).

There are clusters of unstable rock slopes in northern Norway, and while the ones redeemed as most critical have been examined and potentially monitored, a lot of the sites are yet to be examined in detail.

From a study of structurally controlled rock slope deformations in Troms and Finnmark county, Vick et al. (2020) was able to interpret different failure mechanisms and characteristics at several sites in Troms (now Troms and Finnmark) to determine regional trends. Basal and rear ruptures of RSDs in Troms appeared along pre-existing structural patterns such as faults, the angle of foliation and joint sets. Rock slopes with a shallow inclination (around 20°) and a steeper foliation (around 30–40°) following the slope, seemed to have a foliation-controlled rear rupture (Vick et al., 2020). On steep slopes with a shallow or in-slope dip of the foliation, joint sets tend to form the rear rupture surface, while the displaced block tend to move as a more coherent unit than in the foliation-controlled sites. At places where faults were present, the rear rupture could be fault-controlled. None of the identified rear rupture surfaces found on localities in Troms would naturally reappear down-slope, something that suggests a transition

to a basal rupture surface downslope, forming a compound slide deformation. Additionally there was discovered thrusting and compression at several sites near the foot of the RSDs, supporting the theory of a basal rupture surface, likely following existing structures like foliation and joints with step-fractures in between (Vick et al., 2020). Step-fracturing means that it transitions from old inherited fractures to new ones as the deformation develops.

2.1.3 Slow rock slope deformations

Large unstable mountain slopes are largely controlled by lithological and structural conditions such as foliation, joints and active faults, as well as climate (Hermanns and Longva, 2012). Slow rock slope deformations are characterized by creeping slow displacement rates of millimetres or centimetres per year (Rott et al., 1999, Wasowski and Bovenga, 2014, Frattini et al., 2018). Even though slow rock slope deformations don't necessarily end up as a sudden catastrophic rock slope failure, the creeping displacement can damage infrastructure within its proximity, and can also lead to smaller secondary failures within the slope (Crippa et al., 2021).

Development of internal deformation within a slow-moving rock slope is limited to its inherited tectonic features, which can be both on a regional scale (following major tectonic lineaments) or a local scale (faults, folds, fractures etc.) (Agliardi et al., 2001, Stead and Wolter, 2015, Crippa et al., 2021). In postglacial unstable rock slopes, structural properties and orientations, controlling the slide, are often inherited from pre-tectonic events and/or from glacial debuttressing (Evans and Clague, 1994, McColl, 2012, Böhme et al., 2015).

Weather and climate are important for slope stability, especially regarding precipitation, snow melt and median air temperatures (Crozier, 2010, Moore et al., 2011, Blikra et al., 2012). Precipitation can increase hydrostatic pressures within a slope over different timespans, which causes it to be less stable (Hutchinson, 1988). Changes to air temperatures over long millennials, will affect thermal ground-regimes and can degrade permafrost (Hilger et al., 2021). It is believed that rock or soil with a continuous low temperature can stabilize deep seated rock slopes, while a change to warmer climate can degrade permafrost and decrease effective shear strength and rock stability (Gruber and Haeberli, 2007, Huggel et al., 2012, Krautblatter et al., 2013).

In paraglacial landscapes, such as northern Norway, gravitational driven stress and hydrological factors associated with deglaciation can trigger progressive slope failures and lead to a complex creeping slope with different morphological structures present (Crosta et al., 2013, Riva et al., 2018, Agliardi et al., 2020). Both extensional and compressional morpho-gravitational structures (fig. 4) such as double crested ridges, scarps, counterscarps, trenches (extensional), a bulging toe and folded/thrusted rock units (compressional) can indicate the presence of a deep-seated large slow rock slope deformation (Zischinsky, 1966, Radbruch-Hall et al., 1976, Agliardi et al., 2001).

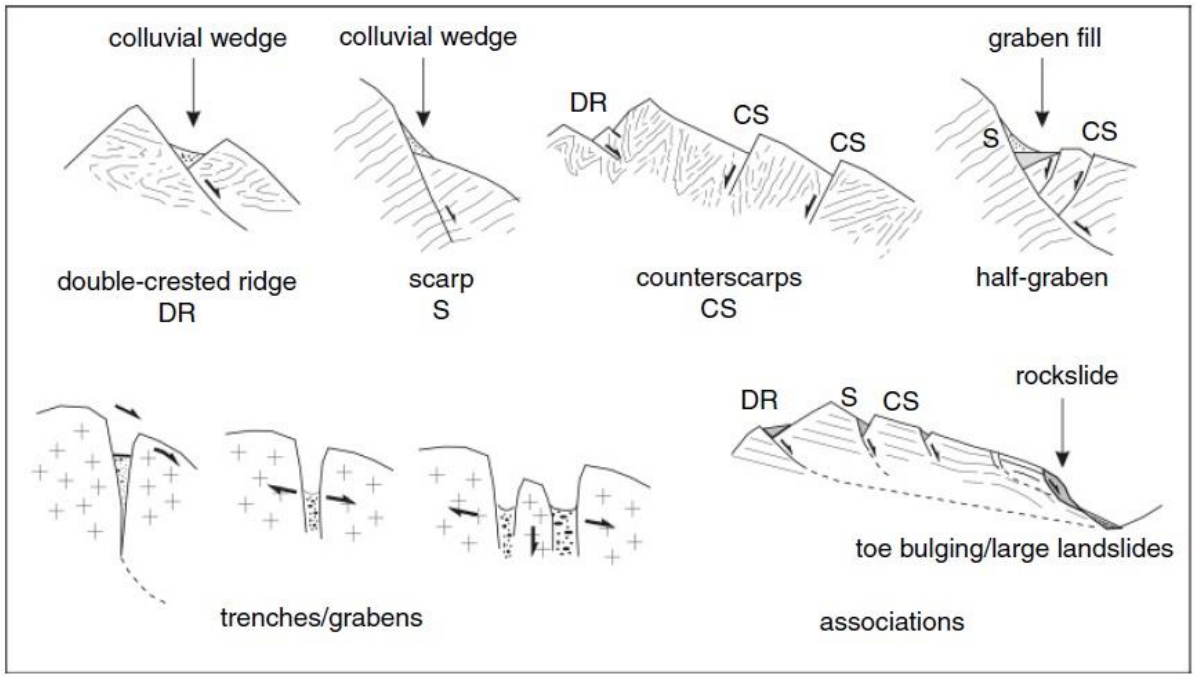

Figure 4: Morphological structures illustrated by Agliardi et al.(2012). Different morphological structures that are common to find at large slow rock slope deformations.

Large slowly deforming rock slopes can range in size, from deep-seated gravitational slope deformations (DSGSD/MSD) reaching across entire mountain flanks, to somewhat smaller, but still large scale landslides, or rock slope deformations (RSD) (Crippa et al., 2021). RSDs can develop independently or as a secondary failure inside a larger DSGSD, in which case the RSD will show more mature morphological elements and a higher degree of internal deformation than the host DSGSD (Agliardi et al., 2012).

2.1.4 Monitoring unstable rock slopes

Even though one cannot physically prevent the failure of a large rock slope, they can be located and monitored in order to reduce risk, by setting up early warning systems and have plans for emergency evacuation (Crosta and Agliardi, 2003). By using methods like the space-based synthetic aperture radar interferometry (InSAR) and global navigation satellite systems (GNSS) it is possible to identify, monitor and evaluate displacement of unstable rock slopes. Generally, in the time preceding an eventual slope-failure, the rate of deformation will accelerate until the final collapse, which can be used to assume when there is an increased chance of failure (Hermanns and Longva, 2012).

The theory of an accelerating rate of deformation until failure was crucial when monitoring the unstable rock slope of Veslemannen which failed on the 5th of September in 2019 (Kristensen et al., 2021), after being monitored since October 2014. During this time Veslemannen had an increase in displacement rate from year to year, especially from 2017, and had periods of acceleration between spring and fall, thought to be linked with seasonal thermal regimes and precipitation events.

The main method used to monitor slope deformations at Veslemannen was ground based InSAR (GB-InSAR), which is used in this thesis as well (see chapter 2.2). In addition, extensometers and timelapse cameras was also used (Kristensen et al., 2021). The GB-InSAR radar was placed in a line of sight close to the slopes interpreted direction of movement to gather as true displacement-data as possible. The combination of gathered quantitative displacement-data and the subjective interpretation by an experienced management was the foundation to what hazard levels were forecasted (Bertolo, 2017, Kristensen et al., 2021). During periods of considerable acceleration, a red hazard level was forecasted, causing the affected community to evacuate. The red hazard level was forecasted a total of 16 times before Veslemannen had its final failure. In the 2018/2019 season an annual displacement of more than 6m/year was measured, and a peak velocity of more than 1m/day after heavy rain. Displacement rates at Veslemannen during its late pre-failure period is pretty extreme when compared to the annual displacement rates of some of todays monitored sites Åknes (2–15cm/year) (Roth and Blikra, 2005) and Gammanjunni (5cm/year) (Kristensen et al., 2021). Åkenes has, among more direct methods like extensometers and laser ranging, been monitored with geophones in order to detect small

seismic events related to the slope-movement (Roth and Blikra, 2005). At Gammanjunni, methods like 2D InSAR and dGNSS displacement-data has been used for monitoring, just like in this thesis (Böhme et al., 2018).

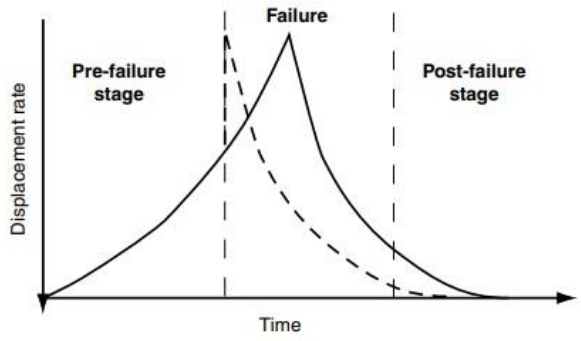

Figure 5: Displacement rate shown on y-axis in relation to time shown on x-axis. Failure of a rock slope will often accelerate close to the point of failure, but with some slopes, a triggering factor like an earthquake can speed up the process and cause failure within seconds. Source: (Hermanns and Longva, 2012).

Even though Veslemannen had a successful warning system which was based on acceleration until collapse, such a system will not be possible for all rock slopes. In seismic active areas a rock slope failure can suddenly become triggered within seconds, with little to no time for acceleration to build up (dotted line fig. 5) (Hermanns and Longva, 2012). For such an area, local planning with restricted zones might have to be implemented instead of warning systems (Welkner et al., 2010).

2.2 Relative dating from deglaciation substages and paleo shorelines

End moraines, deltas, terraces, and shorelines are some of the features that is correlated with advancing and retreating ice sheet, due to glaciation/deglaciation cycles. They often occur in association with each other and can sometimes be traced over long distances along the coast (Romundset et al., 2017, Sollid et al., 1973). Ice marginal deposits like moraines and paleo shorelines have been used for relative dating since quaternary geology in the northern coastal areas was first described by the likes of Hansen (1900) and Tanner (1915). Ice marginal moraine systems has been mapped for northern Norway (fig. 6A) (Sollid et al., 1973). On figure 6A, the age of the ice margins follows their numbering, with 1 being the oldest and 7 the youngest. The shore level can only form distally to an ice margin, so by using the landward extension of a specific shore level one can discover where the ice margin would have been simultaneously to the shore level being created (fig. 6B) (Romundset et al., 2017). Raised shorelines can then be used to correlate ice marginal depositions between fjords.

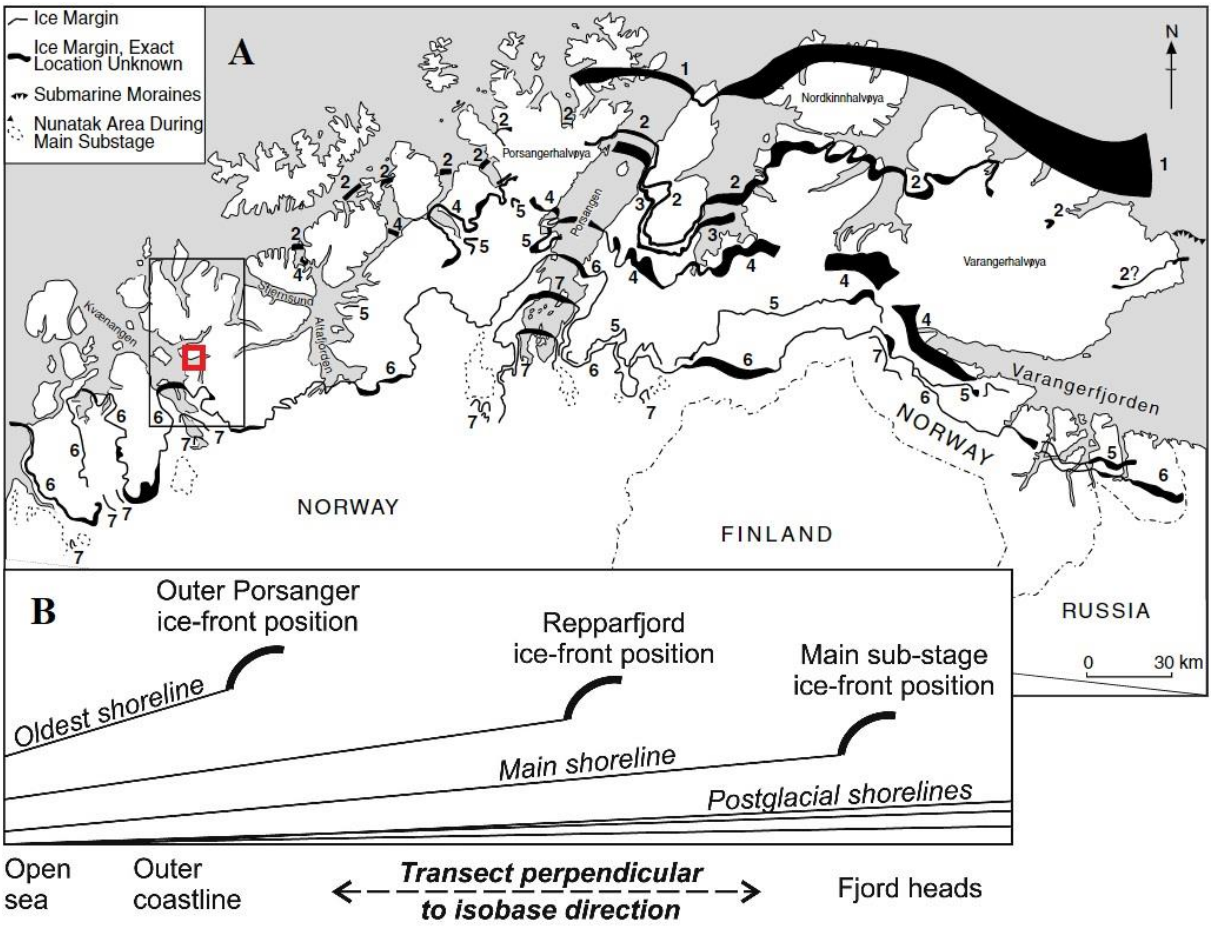

Figure 6: A: Map showing ice marginal moraine systems (sub stages) mapped throughout northern Troms og Finnmark, adapted by Sollid et al. (1973). 1. Risvik substage. 2. Outer Porsanger substage. 3. Korsnes substage. 4. Repparfjord substage. 5. Gaissa substage. 6. Main (Troms-Lyngen) substage. 7. Post main (Stordal) substage. Red square marks Dusnjárga. B: Shoreline diagram by Romundsen et al. (2017), showing different raised shorelines that has been mapped up against different major ice marginal deposits. This can then be used to reconstruct deglaciation sub-stages from different fjords, based on the elevation-correlation between raised shoreline-sets (Romundset et al., 2017).

Isobase maps can be used to date morphological structures that intersects paleo shorelines or known moraines by comparing them to other dated sites along the same isobase-line.

2.3 InSAR

InSAR is a technique that has shown to be very useful in order to categorize slow ground-based deformation rates (Crippa et al., 2021). Previously, simple in-field measurements like extensometers have been used when monitoring displacement in rock slopes (Bovis, 1990), and later introductions like GNSS has been introduced for assessing rock slope kinematics (Aguado et al., 2006, Eberhardt et al., 2008). While both methods give accurate measurements, they are time consuming and only provide point-based measurements. The InSAR method has risen in

popularity during the last decades with a wide variety of usage and the possibility for remote sensing. Urban displacement mapping (Songbo et al., 2020), seasonal ground-effects in permafrost landscape (Rouyet et al., 2019) and unstable rock slope related movements (Colesanti and Wasowski, 2006, Del Soldato et al., 2019, Vick et al., 2020) are some of the applications where InSAR has shown to be useful.

The spaceborne SAR satellite goes in a polar orbit transmitting electromagnetic waves as microwave pulses, hitting the earth's surface within a certain line of sight (LOS), as shown in figure 7. These pulses are then reflected as scattered signals by the earth and recorded back at the satellite, giving an amplitude and phase component. The amplitude is related to the properties of surface scattering, while the phase is related to the satellite to ground distance. The InSAR method involves studying the phase difference between two radar images of the same spot, but captured at different times, to extract changes in distance which is related to LOS surface displacement (Lauknes, 2011, NGU, 2019).

In relation to unstable mountain slopes and other geologic postglacial processes, field investigations, the use of LiDAR and geomorphological mapping done by aerial photos and such, has been the most common techniques for interpreting their characteristics (Crippa et al., 2021). The introduction of InSAR has made this work a lot cheaper and efficient. In Norway, the use of InSAR has proven to be a valuable tool, especially when trying to map displacement rates and limits of unstable rock slopes over large areas (Lauknes, 2011, Eriksen et al., 2017, Böhme et al., 2018, Vick et al., 2020). Revisiting time of orbiting SAR satellites in northern Norway is only a couple of days. This is due to the path of SAR satellites enclosing towards the poles, which makes it possible to get frequent and consistent new displacement data from both ascending and descending satellites (NGU, 2019).

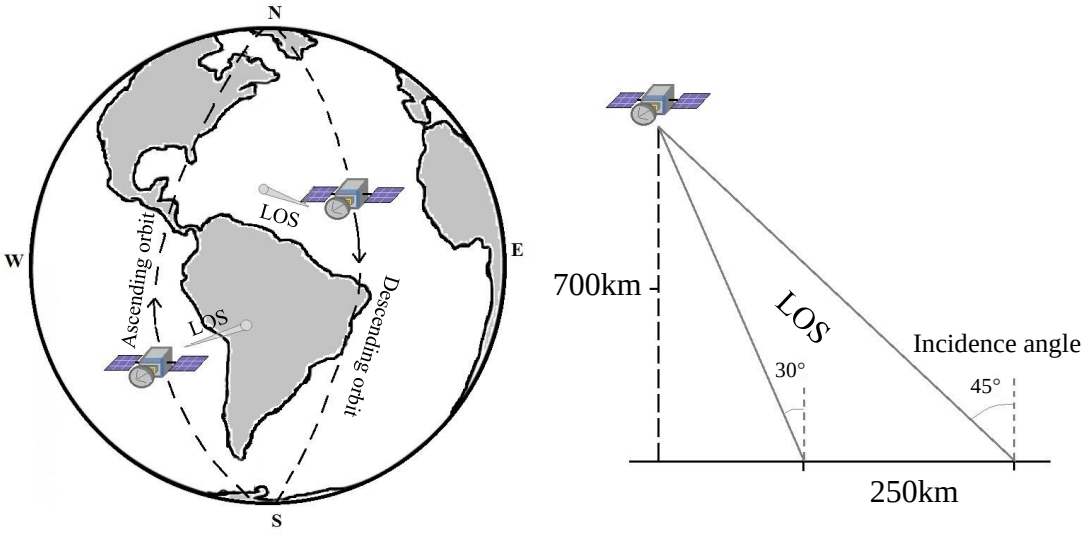

Figure 7: To the left is the ascending and descending paths of a SAR satellite on its polar orbit and its LOS. To the right is a sketch of the LOS from a SAR satellite, covering an area of 250km with an incidence angle of 45°. Inspired by (NGU, 2019, Sandbakken, 2021).

2.3.1 Using 2D and 3D InSAR

One SAR geometry is usually not adequate to get exact information about surface displacement-orientations or velocities of measured points on the ground. This is because measurements will only be done along the LOS of that geometry, which normally does not correspond to the true displacement of measured ground-points. By combining information from two separate SAR geometries, one ascending (moving towards north) and one descending (moving towards south), a 2D presentation can be made showing displacement rates along a cross section (Lauknes, 2011, NGU, 2019, Sandbakken, 2021).

The use of 3D InSAR can be useful for interpreting local variations within a deforming rock slope and gives displacement vectors set in a 3D display. To do this, accurate displacement data must be acquired from a third source, complementing the two satellite sources (fig. 8). LOS from the third source should have a different angle to the measured slope than the other two LOSs, which is typically achieved by a ground based radar (GB-radar), set up at a suitable angle in front of the slope (Eriksen et al., 2017).

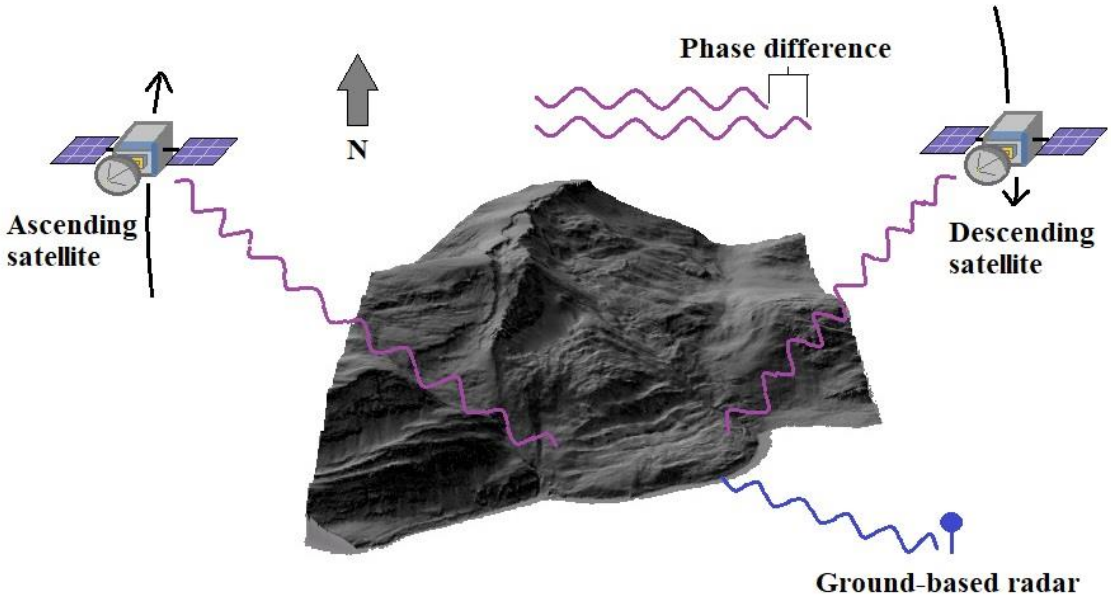

Figure 8: 3D hillshade of Dusnjárga, made in ArcGIS Pro from a 1 m DEM (Kartverket, 2021), with InSAR sources needed to make a 3D vector projection. If the rock slope shows displacement with time, InSAR detects it by a phase difference in the reflected microwaves, sent at different points in time. A GB-radar as a third source of data is needed to make 3D projections of displacement. Inspired by (Lauknes, 2011, NGU, 2019, Sandbakken, 2021).

2.3.2 InSAR limitations

The polar orbiting SAR satellites have a fixed LOS, typically to the right of their movement, which means that ascending geometry have a LOS in an eastern/north-eastern direction, while descending geometry have a LOS in a west/north-western direction. This makes detected displacement rates in the East-West plane good, but also means that detection of displacement close to the North-South plane will be poor, close to zero (Eriksen et al., 2017, NGU, 2019). A ground-based radar placed with a north-south facing LOS is a good way of dealing with this problem if examining north/south facing rock slopes.

InSAR data will have noise caused by various reasons, some easy to filter out, while others are more complex. Changes to the geometrical properties within pixels over time can be due to displacement. If this change in pixel is due to movement in vegetation or some variation in the snow cover etc., instead of an actual movement of seated ground-points, it is noise, which can show abnormal movements. (Eriksen et al., 2017, NGU, 2019). InSAR Norway has dealt with the snow cover problem by only using SAR observations from the snow-free months of June–October, then anticipating annual movement based on measurement during these summer

months. (NGU, 2019). In very steep slopes facing towards the satellite, foreshortening can occur, where distance to the ground is misjudged.

Datasets from InSAR Norway are processed as tiles of around 5x5 kilometres. The alignment of these tiles can be hard to merge properly since each tile is processed separately, which can result in a linear shift of displacement values right where the tiles come together. Atmospheric noise is something that must be filtered out, but can be incomplete in deep valleys, as a layered stratosphere can be present there. Wetlands can also lead to noise as water-levels can change and affect the ground to some extent (NGU, 2019). It is important to keep in mind that noise does happen, so single pixels or strange displacement-results should be interpreted with caution.

2.4 dGNSS

dGNSS is a common technique used when surveying unstable rock slopes and is often used in combination with InSAR (Dehls et al., 2012). Satellite-based radionavigation, positioning and timing systems fall under the general term of GNSS, with well-known systems such as; the American Global Positioning System (GPS) and the Russian GLONASS system (Oppikofer et al., 2013). Roughly, these systems are set up in a three-component structure, with space-born satellites sending signals, stations on ground controlling the system, and a network of signal-receiving antennas that register the electromagnetic signals (Seeber, 2003).

The dGNSS technique registers measured phase-differences between a network of GNSS antennas that enables interpretation of movement-vectors between each antenna. Coordinates of each antenna is calculated by a least squares adjustment of measured movement vectors and movement is expressed based on presumed stable points nearby (Oppikofer et al., 2013). Measured displacements do not always follow a coherent trend, but can sometimes occur rather chaotic, as mentioned by Hermans et al. (2011) and Bøhme et al. (2013). Chaotic trend can suggest opening/closing of cracks due to porewater pressure, thermal expansion (Hermanns et al., 2011) or caused by temporal permafrost-fluctuations. A coherent trend of displacement rates can indicate a certain gravitational-driven movement. Accuracy of GNSS-coordinates are generally said to be 1 mm, but this is found to be too generous, so an increased accuracy (uncertainty "σ") of 2–3 mm should be more realistic. (Oppikofer et al., 2013).

3 Study area

Dusnjárga is an unstable rock slope located in northern Norway, at the municipality of Kvænangen in Troms and Finnmark county (fig. 9). The unstable rock slope sits on the southern side of a peninsula located between Jøkelfjorden in the north and Lille Altafjorden to the south. The peninsula is 11 kilometers long and highly mountainous with Laslettind to the east, followed by several mountains connected by ridges, until you reach Vassnestind to the west. In the middle of this local mountain range stands Koppartinden with its highest point at 930 m.a.s.l. Dusnjárga is located on the southern side of Koppartinden, with its backscarp at an altitude of 830 m.a.s.l. The peninsula of Dusnjárga is a part of the bigger Øksfjorden peninsula, located to the southwest in the Seiland Igeneous Province (SIP) (fig. 14).

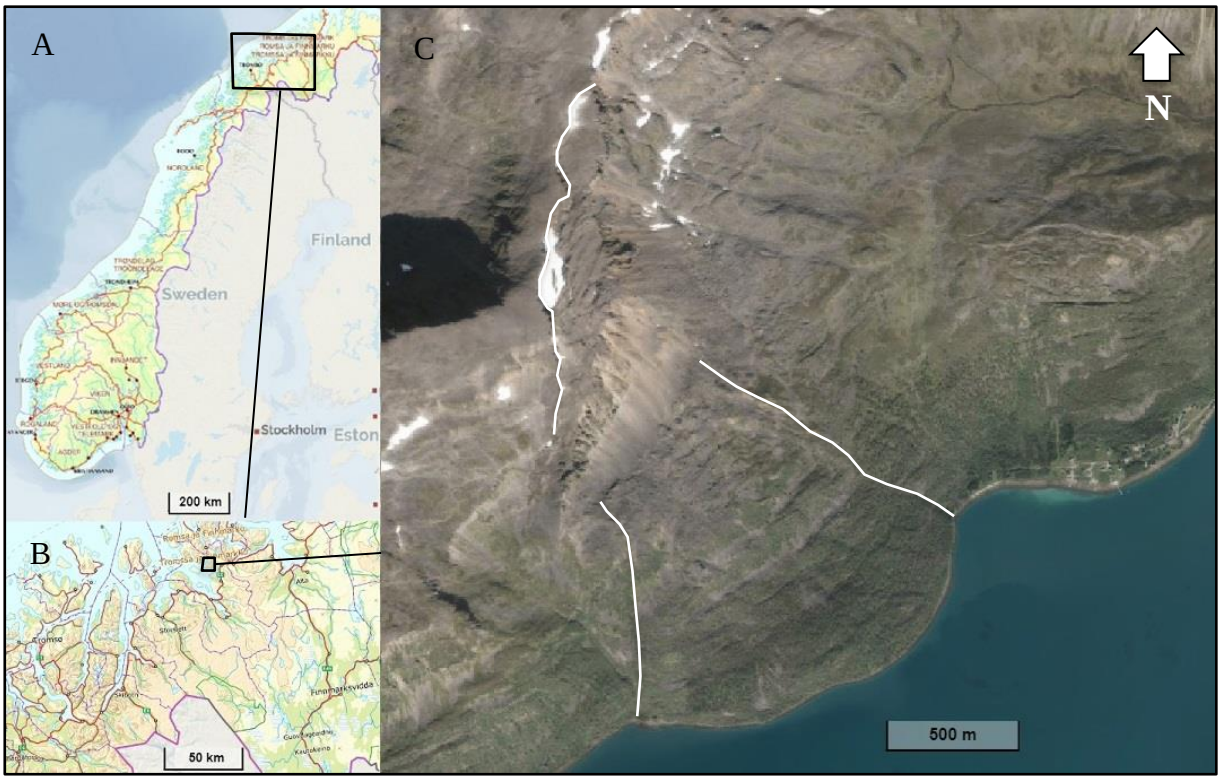

Figure 9: A: Map from Kartverket picturing Norway with its major cities and counties (Kartverket, 2014). B: Map of central part of Troms og Finnmark county, located in northern Norway. Area of interest is found west of Alteidet, in the municipality of Kvænangen (Kartverket, 2014). C: Orthophoto of the area of interest (Kartverket, 2015). White lines depict a backscarp and the lateral limits of the rock slope deformation.

The area around Dusnjárga is sparsely populated. There is a small settlement in the inner parts of Lille Altafjorden, as well as a slightly larger settlement of around 380 people in Burfjord, 10 kilometers to the south (Store Norske Leksikon, 2009). There are 18 houses, some sheds and

other infrastructure located 500 meters east of Dusnjárgas eastern lateral flank, at the foot of Låvan. Låvan is another unstable rock slope located 1 kilometer east of Dusnjárga, which has previously been inspected by NGU (Redfield et al., 2011) and undergone fieldwork in relation to the master thesis of Frederic Blau (Blau, 2020).

3.1 Climate

Dusnjárga is located by the coast and has an annual precipitation of between 1000–1500 mm/y, according to a precipitation-map from the Meteorological Institute of Norway (MET Norway) (fig. 10). Precipitation measurements from nearby weather station Sopnesbukt, located a couple of kilometres to the east, has recorded around 800 mm/y during the last years (Meterologisk institutt, 2022).

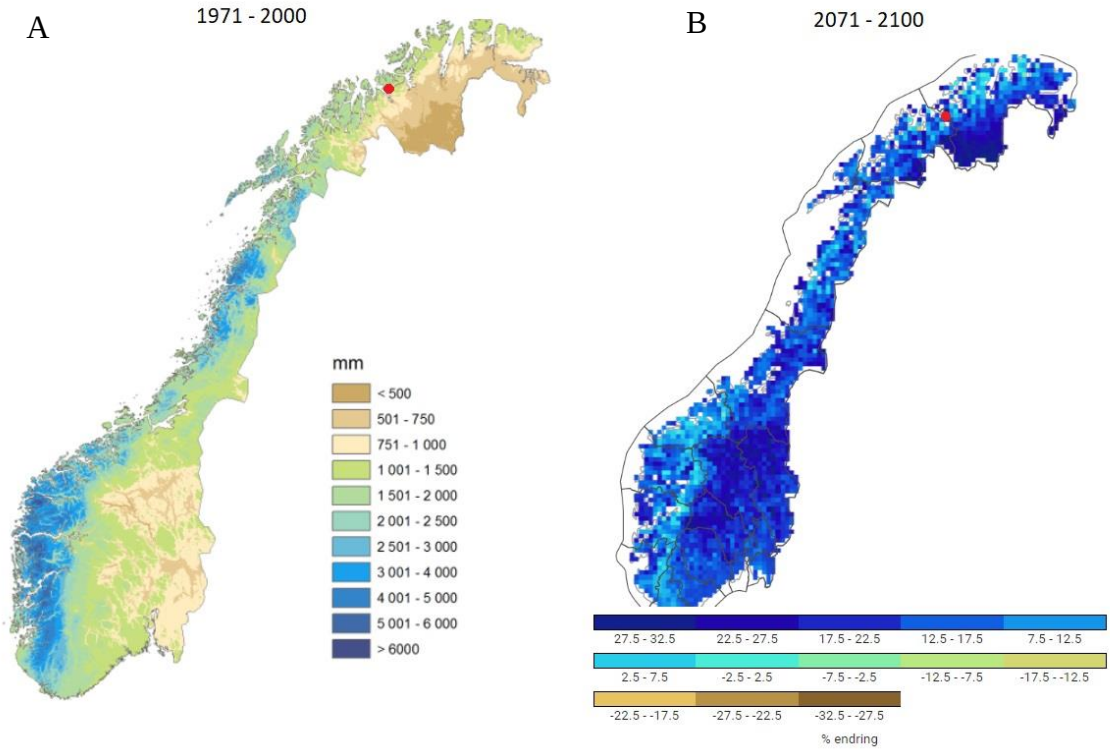

Figure 10: A: Map of annual percipitation based on measurements done across Norway between 1971–2000 with greenhouse emmisions after RCP8.5 (Hanssen-Bauer et al., 2009). Dusnjárga falls in the 1001–1500 mm/y category, but is close to falling into the 751–1000 mm/y category, which suggests it might be closer to 1000 mm/y than 1500 mm/y. B: Expected change in percipitation from 1971–2000 and forward to 2071–2100. Red dots mark the location of Dusnjárga. There is an expected increase in percipitation at Dusnjárga of between 12,5–22,5 percent (%). Figure adapted from: (Meteorologisk Institutt, 2021a).

The annual middle temperature during the last 10 years, from the nearby weather station Sopnesbukt has been between 3 and 4 °C (Meterologisk institutt, 2022). Dusnjárga has a coastal climate with annually more precipitation and humid air than found inland. The winters are relatively mild when compared to other places in the world at such a high latitude (Meteorologisk Institutt, 2021b).

Projections of future climate estimates in Norway have been reported by The Norwegian Centre for Climate Services (NCCS) in the report "Climate in Norway 2100" (Hanssen-Bauer et al., 2009). A report by the Intergovernmental Panel on Climate Change (IPCC) gave three different emission-scenarios set in the future, called the Representative Concentration pathways, or RCPs (Zhongming et al., 2013). RCP2.6 is an emission-scenario where greenhouse gasses must see a drastic cut, starting already before 2020. RCP4.5 is a scenario where greenhouse emissions have a slow increase up until year 2050, while emissions after that start to be reduced. RCP8.5 is based on emissions continuing its upwards trend without any drastic countermeasures (Zhongming et al., 2013).

The climate at Dusnjárga will change in the coming years, the following estimations are based on the RCP8.5 scenario. The average annual temperature can be expected to rise by around 5°C by 2100 (fig. 11). Winter temperatures will increase slightly more than temperatures during the summer months. Vegetation can be expected to expand to new places, due to a warmer climate and less months with snow coverage, meaning more time to grow, which will result in a higher treeline and generally more dense vegetation (Meteorologisk Institutt, 2021b).

According to MET Norway, precipitation is expected to rise with 15 % for Troms and Finnmark. The precipitation will increase differently for each season. Winter and spring will have a c. 10% increase in precipitation, while summer will have a c. 30% increase and fall 20% (Meteorologisk Institutt, 2021b). There is expected to be a 25% increase in days with unusually high amounts of precipitation, and an even higher percent increase in shorter than one day-episodes of unusually high precipitation. (Meteorologisk Institutt, 2021b).

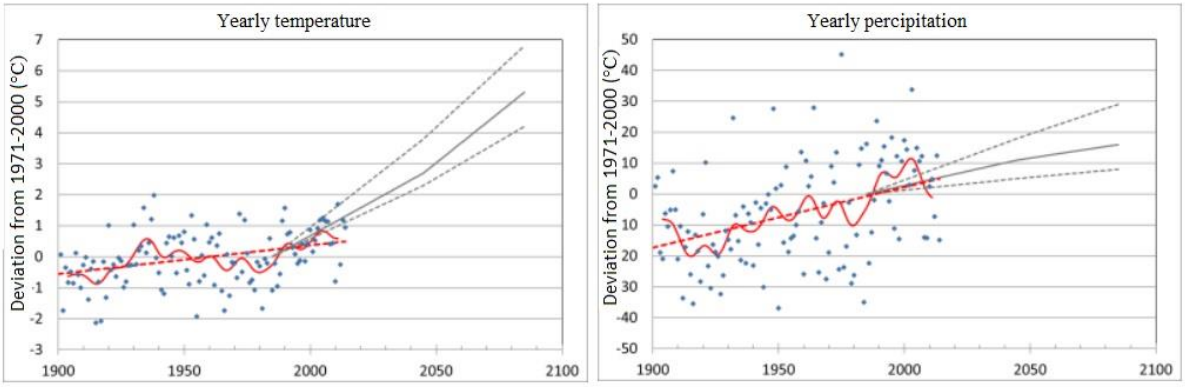

Figure 11: To the left is a graph showing development of annual temperatures in Troms from 1900–2100. The values in the Y-axis show the deviation of temperature (°C) compared to the normal measured period of 1971–2000. Red line shows the trend of temperature deviation per tenth year, while blue dots show the middle temperature of that single year. The solid grey lines show the expected middle value based off high greenhouse-gas emissions until the year 2100. Dotted grey lines show a lower and higher calculated limit of temperature deviation. To the right is the same figure but with precipitation in mind. There is clearly an upwards trend in both temperature and precipitation. Figure adapted from: (Meteorologisk Institutt, 2021b).

3.2 Permafrost

Permafrost is present soil or rock that has had a temperature below 0°C for two or more years in succession (Brown and Kupsch, 1992). From comparing the age of initial deformation in rock slopes with the timing of deglaciation, it is believed that permafrost could have a big part in destabilizing slopes in postglacial environments (Hilger et al., 2021).

The extent of permafrost in Norway (fig. 12) can be viewed on a map, made by using the equilibrium model CryoGRID 1.0 to estimate temperatures at the top layer of permafrost or the bottom layer of a seasonally frozen ground (TTOP), based on the degree of accumulated thawing and freezing-days during a year (Gisnås et al., 2017). From the measured distribution of TTOP within a certain grid, the percentage of permafrost in that grid is defined (Brown et al., 1997).

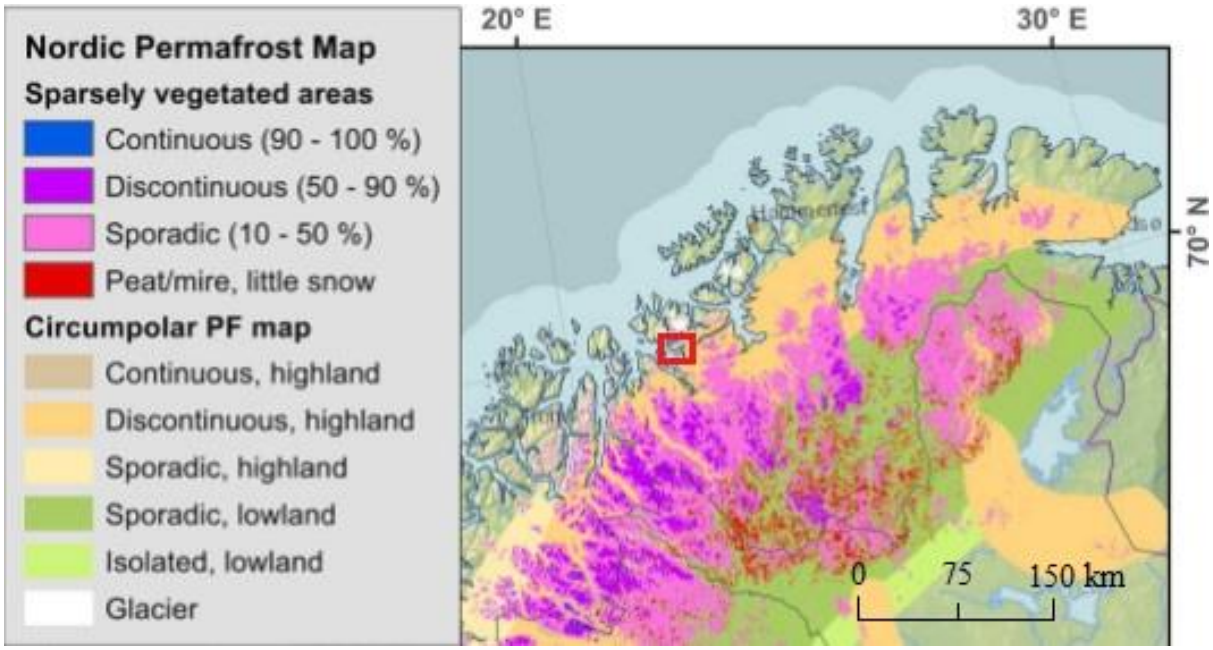

Figure 12: A Nordic permafrost map covering parts of Troms and Finnmark. Purple/blue/red colours represent the interpreted permafrost distribution using CryoGRID 1.0, from Gisnås et al, (2017). Colours from "Circumpolar PF map"-legend shows an earlier version of a Nordic permafrost map by Brown et al. (1997). Red square marks the Dusnjárga peninsula. Adapted from:(Gisnås et al., 2017)

Both permafrost-maps (fig. 12), from Gisnås et al. (2017) and Brown et al. (1997), suggests that permafrost in the mid-coastal areas of Troms and Finnmark does not extend as far to the coast as the Dusnjárga peninsula. There may however be sporadic traces in the slope.

In Norway, the permafrost is restricted to mountainous areas in the south, while appearing sporadically at lower elevated areas at higher latitude (e.g. Troms and Finnmark) (Farbrot et al., 2013). A study of permafrost in steep walls was done by Magnin et al. (2019), which resulted in a CryoWall map, showing the extent of permafrost in steep rock slopes across Norway. Given suitable conditions permafrost can be found at lower altitudes than expected in some steep rock slopes. Slopes that have sub-vertical faces with little cumulation of snow and are oriented in a way that give less sunlight during the warmer summer months, are more susceptible to having permafrost (Magnin et al., 2019). This study showed that in steep slopes of northern Norway, sporadic permafrost could be found all the way down to sea level. Discontinuous permafrost could mainly be found above 750 m.a.s.l. in north facing slopes and above 1050 m.a.s.l. in south facing slopes. While continuous permafrost was usually found above 1100 m.a.s.l. in north facing slopes and above 1400 m.a.s.l. in south facing slopes (Magnin et al., 2019).

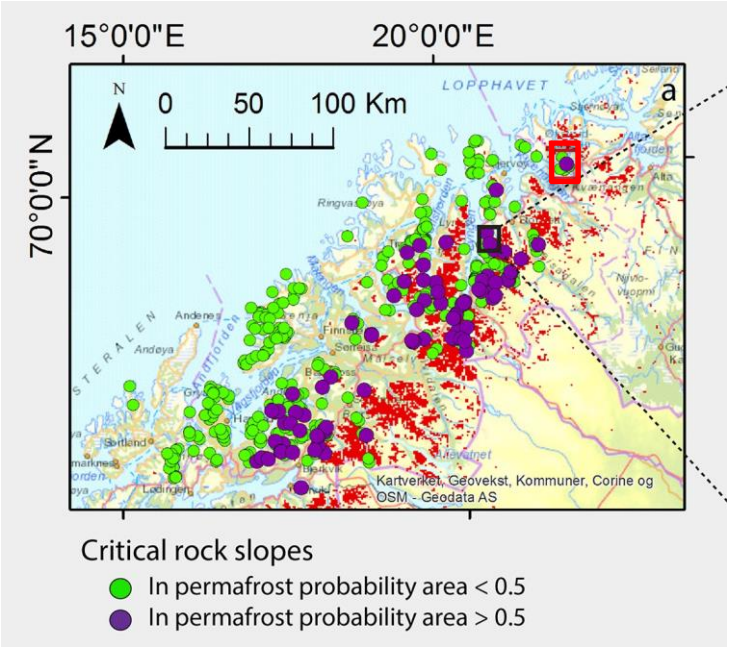

Figure 13: Red areas are estimated to have discontinuous or continuous permafrost in its steep slopes. Green circles mark unstable rock slopes that fall outside the red areas, while purple circles mark unstable rock slopes located within the discontinuous area. Red square marks area of the Dusnjárga peninsula. Black square with dotted lines does not serve any purpose here. Adapted from (Magnin et al., 2019).

There are some unstable rock slopes in the Dusnjárga peninsula that overlap with expected areas for discontinuous permafrost in steep slopes, while some do not, as can be seen as purple/green circles in the red square of figure 13. The northern side of the peninsula is generally steeper than the southern side where the unstable rock slope Dusnjárga resides. NGU are monitoring slopes on both the north and the south side of the peninsula.

3.3 Geological setting

3.3.1 Bedrock geology

The Dusnjárga peninsula is a part of the Seiland Igneous Province (SIP). SIP is a large complex of mafic/ultramafic intrusions located in northern Fennoscandia, with a rare display of deep magmatic root-systems (Pastore et al., 2018). The SIP extends about 100 kilometres in length and is about 50 kilometres wide (fig. 14). Its plutons are mainly consisting with mafic and ultramafic material, like layered gabbro with a tholeiitic or alkali olivine composition. Dykes in the SIP are mostly mafic, and there is also alkaline complexes and carbonatites present (Roberts et al., 2010).

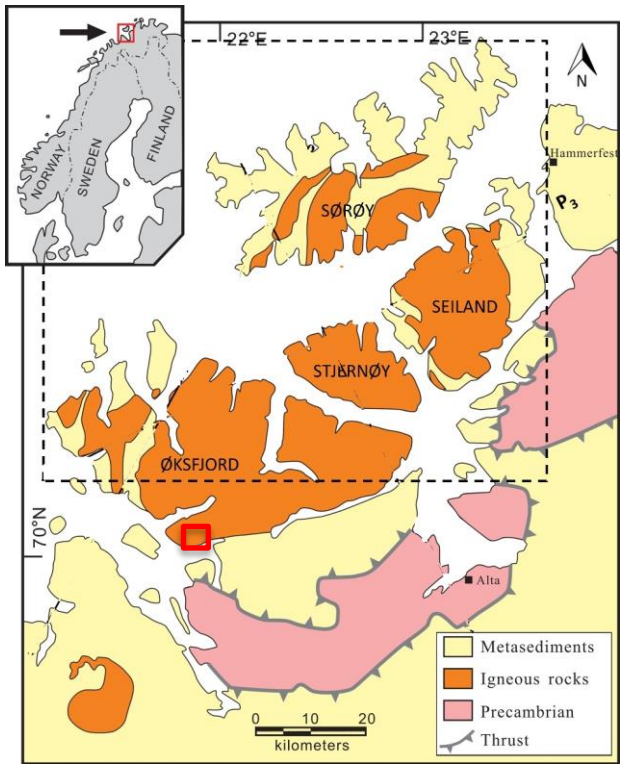

Figure 14: Seiland Igneous province, a large complex of mafic and ultramafic intrusions, located in northern Norway. It starts with Øksfjord peninsula in the southwest and extends to Stjernøy, Seiland and Sørøy in the northeast. Red square marks Dusnjárga. Source: (Pastore et al., 2016).

The SIP was intruded between 580–560 Ma. (Roberts et al., 2006, Pastore et al., 2016). The rock is denser than its surroundings, measuring 3100 kg m^{-3} compared to 2700 kg m^{-3} for the upper crust and 3300 kg m^{-3} compared to 2900 kg m^{-3} for the lower crust (Pastore et al., 2016). The general depth of the SIP is estimated to be within the range of 2–4km, while the deepest roots on Seiland and Sørøy has been estimated to reach a depth of around 9 kilometres (Pastore et al., 2016).

Roberts, et al. (2006) states that the relative short active period of the main plutonic phases suggests that the mechanisms of emplacement of the mafic magma was done by a single tectonic regime, probably extensional. At later stages the mafic intrusions were metamorphosed to at least amphibolite facies, most likely during the Caledonian Orogeny at 420 Ma. The annular root pattern of the SIP is found to be rather undisturbed, which can suggest that it has not been subjected to any major reworkings during the Caledonian Orogeny (Pastore et al., 2016).

The bedrock at Dusnjárga peninsula has only been mapped on a 1:250000 scale (fig. 15-B), which will naturally be less detailed than a map of a smaller scale. Figure 15-C shows a more detailed bedrock map on the scale 1:50000, which is from the same igneous origin as the lithology at Dusnjárga. Which highlights that the bedrock at Dusnjárga likely varies a little more than what the 1:250000 bedrock map depicts.

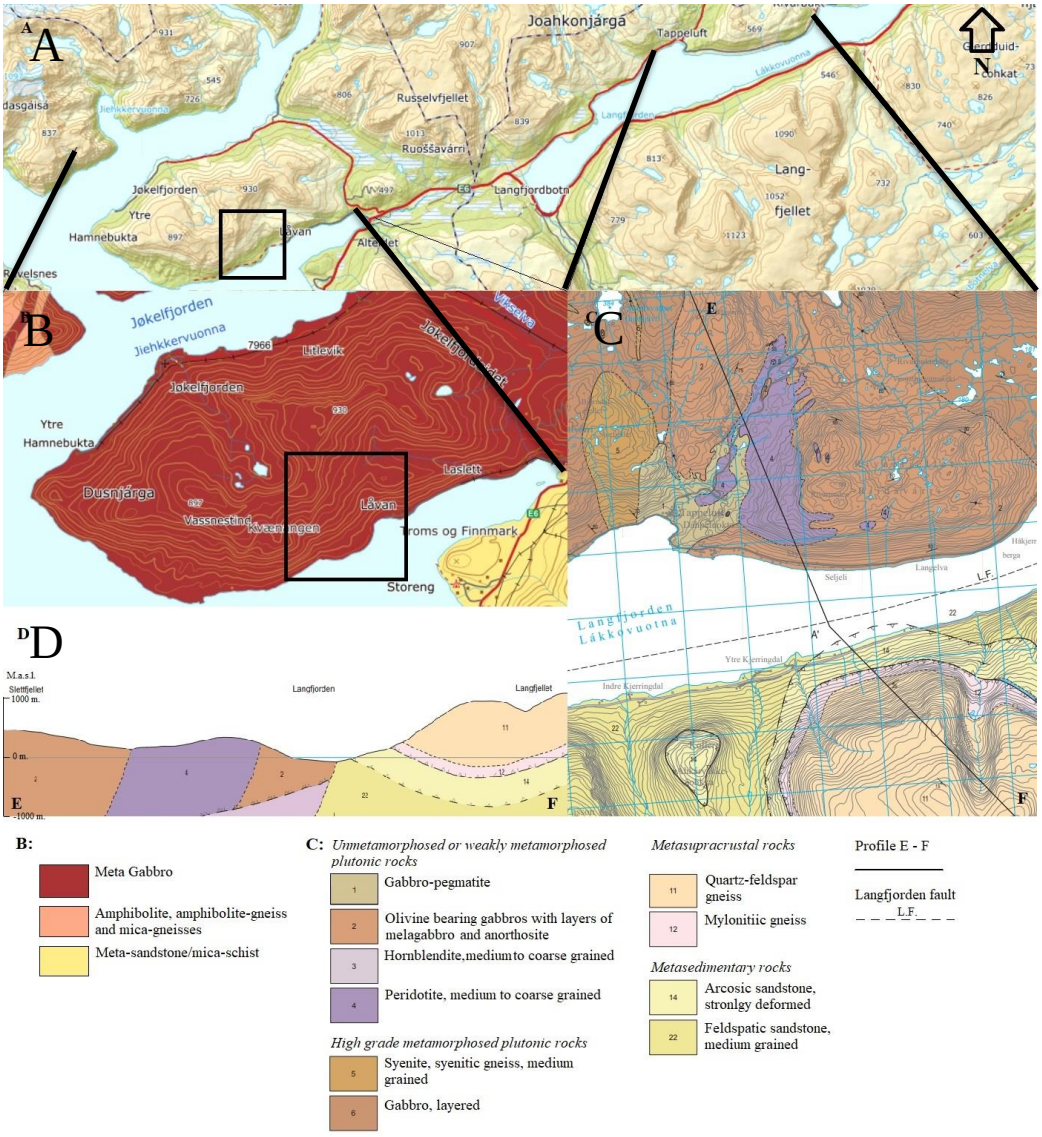

Figure 15: A: Topographic map of the surrounding area. Dusnjárga is marked with a black square while black lines marks where map B and C are placed. Source: (Kartverket, 2014). B: A bedrock map in a 1:250000 scale, displaying Dusnjárga peninsula with the unstable rock slope inside the black square. Adapted from (NGU, 2020b). C: A detailed bedrock map on a scale of 1:50000, displaying parts of Langfjorden, located a couple of kilometres to the east of Dusnjárga. This map displays the local bedrock in more detail than the 1:250000 map of Dusnjárga. Both B and C are parts of the Seiland Igneous Province, which makes them somewhat comparable. D: A interpretation of the E-F profile as marked in C, with the Langfjorden fault in the middle. Adapted from Roberts and Elvevold (2018).

In the available bedrock map from NGU (2020b), the whole peninsula is one unit comprised of layered sets of clinopyroxene-gabbro, gabbro-gneisses and pyroxene-granulite, or simply put as meta-gabbro. Some kilometres to the east, Roberts and Elvevold (2018) has made a more detailed 1:50000 map, which displays a more diverse bedrock setting, which could be representative to Dusnjárga aswell.

3.3.2 Structural geology

The layered gabbro at Øksfjorden peninsula is a heterogeneous sequence of layering that is mainly defined by variations in its plagioclase and pyroxene ratio (Mørk and Stabel, 1990). The different layering sequences are also very much defined by grainsize, amounts of hornblende and biotite and a varying degree of foliation (Krauskopf, 1954). The layering described at Øksfjorden peninsula can vary in scale between one-crystal thick bands and up to metres thick lithological variations. Foliation related to deformation-events tends to be sub-parallel to the igneous layering. Structures that stem from an igneous origin tends to be most common close to ultramafic rocks, while layered gabbros/meta-gabbros tends to be strongly metamorphic foliated both in the northern and southern parts of Øksfjorden peninsula (Mørk and Stabel, 1990).

Folds in the Øksfjorden peninsula are according to Krauskopf (1954), limited to wide, open synclines with small scale contortions near intrusive contacts and faults. The Langfjorden fault (fig. 16), running parallelly with Lille Altafjord, is a part of the Vargsund-Langfjorden fault and separates the plutonic SIP rocks in the north from the Kalak Nappe Complex in the south (Roberts and Elvevold, 2018). The fault is believed to have been created during the Permo Carboniferous or Devono Carboniferous and later reactivated during the Mesozoic (Roberts and Lippard, 2005).

The general trend in foliation-strike at Øksfjorden peninsula, at a 1:250000 scale, is N-S trending, and in some places NV-SE trending, with local variations (fig. 16). As can be seen on figure 16, the strike at the Dusnjárga peninsula differs from the general trend of Øksfjorden peninsula and follows an ENE-WSW trend.

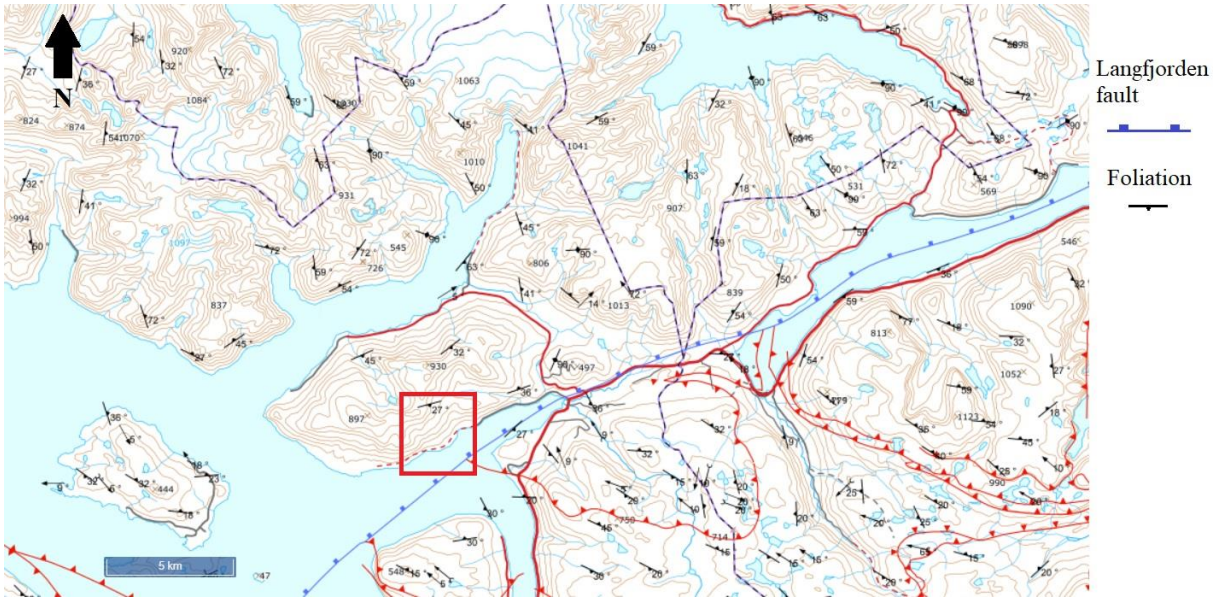

Figure 16: A topographic map from NGU, displaying structural measurements of the southern parts of Øksfjorden peninsula and areas to the south of the Langfjord fault, on a 1:250000 scale (NGU, 2020a). Area of interest is marked with a red square and the Langfjorden fault can be seen as a blue line going through Langfjorden in the east, across Alteidet and towards Lille Altafjorden.in the west.

3.3.3 Quaternary geology

The area around Dusnjárga is dominated by weathered materials, landslide deposits, daylighting bedrock and occasional moraine materials (fig. 17). The deformed rock slope is highly dominated by disintegrated and disaggregated rocks. The western area of the slope has more disintegrated material and is less vegetated than the eastern side. Outcrops of displaced daylighting bedrock are uncommon, with most of them being in the steeper parts of the slope. During a previous master project, a detailed quaternary mapping of Dusnjárga and its surrounding area was performed (Appendix 1). This study also looked at structural and morphological elements of the neighbouring rock slide Låvan. (Blau, 2020).

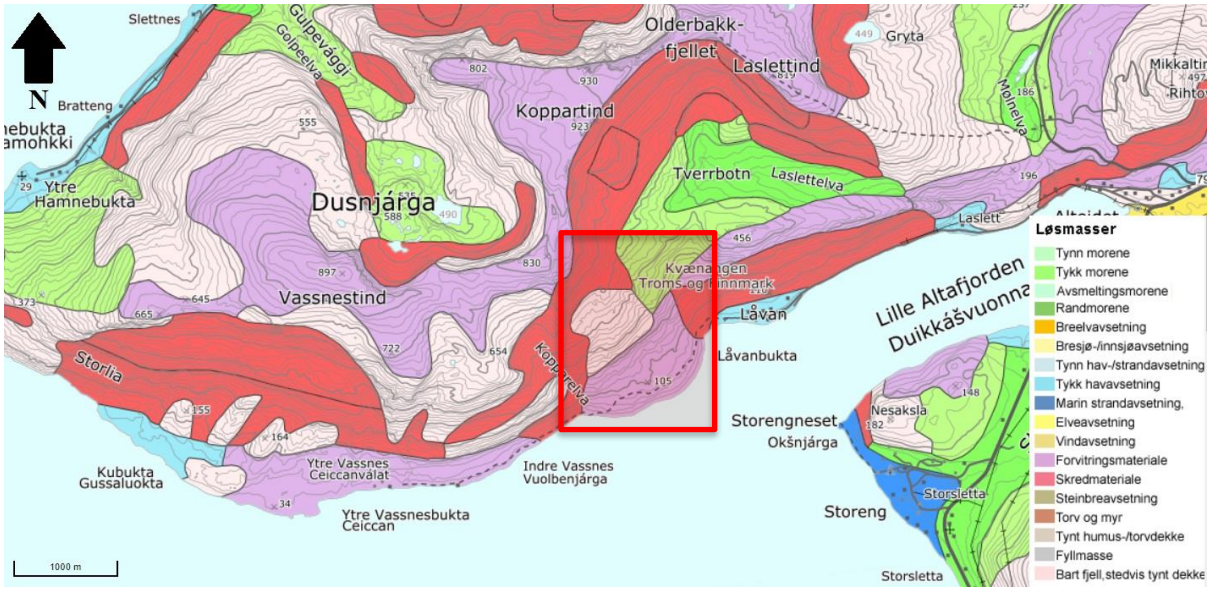

Figure 17: Quaternary map from NGU, depicting Dusnjárga peninsula in a 1:250000 scale. Coloured polygons represent different deposits overlaying a topographic backgroundmap. Red square marks our area of interest. Source: (NGU, 2017).

Regional glaciation and deglaciation

The ice sheet covering parts of Norway, Sweden and Finland is termed as the Scandinavian Ice Sheet (SIS), or Fennoscandian Ice Sheet. There are some uncertainties regarding the thickness of SIS at glacial maximum, although at its core it is estimated to have been around 3 kilometres thick at some point (Fredin et al., 2013). SIS reached its largest point during the Last Glacial Maximum (LGM), 21–23 ka ago, in which it was a part of a larger ice sheet, known as The Eurasian Ice Sheet complex. LGM marks the maximum extent of ice during the last 40 ka, which can vary slightly between different parts of different ice sheets (Hughes et al., 2016, Svendsen et al., 2004, Clark et al., 2012).

Block fields located at higher altitudes and flat mountaintops of similar hight, as can be seen in parts of Troms and Finnmark, suggests that nunataks probably existed during the late Weichselian period (Kverndal and Sollid, 1993, Fredin et al., 2013). Another theory suggests that the preglacial landscape might have been covered by a cold-based ice sheet with an internal thermal boundary (Kleman, 1992, Kleman et al., 1997). The nunatak theory might suggest an unreasonably thin inland ice-cover (Näslund et al., 2003, Fredin and Follestad, 2011), while the cold-based theory might over-estimate the ice sheet thickness in coastal paleo-environments (Fredin et al., 2013).

Hughes et al. (2016) presented a modelled time-slice reconstruction (DATED-1) of the Eurasian Ice Sheet extent during four periods from 25 ka–40 ka and every 1000 years between 10 ka and 25 ka. Their data utilizes published numerical data concerning ice sheet advances and retreats, as well as geological and geomorphological evidence from existing literature. They have then estimated three different scenarios per time-slice, one that is their expected result based on all available data plus a maximum and minimum extent (Hughes et al., 2016). According to DATED-1 by Huges et al. (2016), Dusnjárga would have been covered in ice at 15 ka, and becoming ice-free at around 14 ka. At 13 ka it would likely be completely ice free (fig. 18).

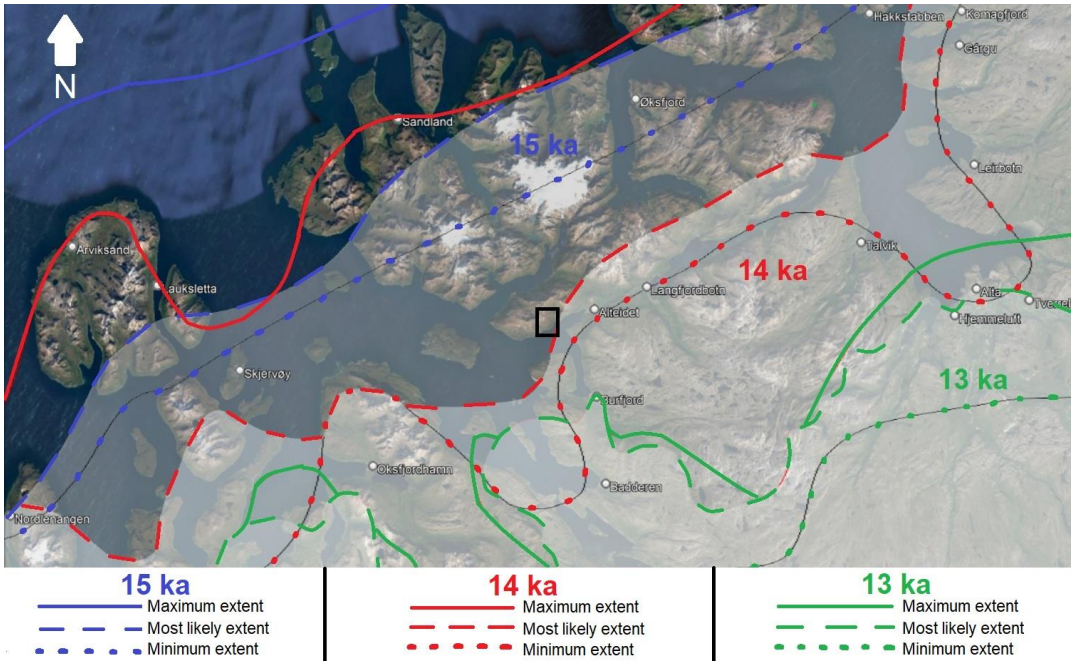

Figure 18: Orthophoto from google earth of central parts of Troms and Finnmark, overlayed with the time-slice reconstruction of 13, 14 and 15 ka, adapted from DATED-1 by Huges et al. (2016). Blue lines represent the estimated ice-sheet coverage at 15 ka, red lines represent 14 ka and green lines represent 13 ka. Solid lines represent a maximum estimation, dotted lines represent a minimum estimation, while dashed lines represent the expected extent of the icesheet. Dusnjárga is marked by a black square on the map.

Substages and paleo shorelines at Dusnjárga

The Tromsø-Lyngen (main) moraine is often more distinct than other substages in northern Norway and is dated to Younger Dryas, or perhaps even later, at around 10000–12000 ^{14}C years before present day. Parts of the Tromsø-Lyngen (main) moraine is found in the inner parts of Kvænangen, just south of Dusnjárga, as can be seen on figure 5 A.

The Tapes shoreline is often found along with the Tromsø-Lyngen substage and sometimes intersecting it. It was created by a transgression that reached its maximum around 5600–7600 cal BP, where the supply of meltwater was greater than the isostatic uplift (Bondevik et al., 2019).

Around Dusnjárga peninsula and south towards Burfjorden there seems to be two distinct shoreline elevations (fig. 19) (Evans et al., 2002, Blau, 2020). An interpolation of the marine limit (main shoreline) from estimated point-locations, given by the Geological Survey of Norway (NGU), displays the expected location of the marine limit at Dusnjárga (Blau, 2020). An elevation of between 65–66 m.a.s.l. was interpreted for the marine limit, however this is just an interpolation without nearby field-observations to support the interpretation. Shoreline 2 was about 60–62 m.a.s.l. and was found in Laslett, east of Dusnjárga (Blau, 2020). The interpolated marine limit matched shoreline 2's elevation well. Shoreline 1 was found at a lower elevation than shoreline 2, but was constantly between 23–25 m.a.s.l. and could be seen along large parts of the southern peninsula (Blau, 2020).

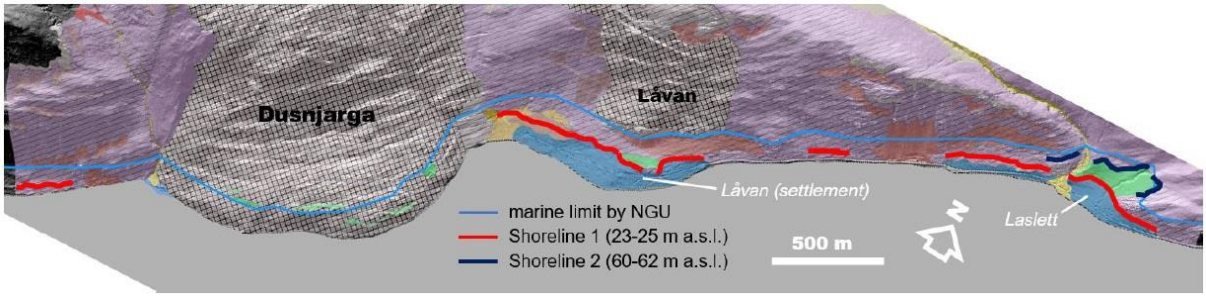

Figure 19: A shoreline map depicting shoreline 1 (red), shoreline2 (dark blue) and the interpolated main shoreline by NGU (light blue). Source: (Blau, 2020)

In Ullsfjord, Lyngen, the Tapes shoreline had been identified as terraces at 21–22 m.a.s.l. by Corner and Haugane (1993), which is on a similar isobase-line (fig. 20) as Dusnjárga and therefore shoreline 1 at Dusnjárga was interpreted as a Tapes shoreline by Frederic (2020).

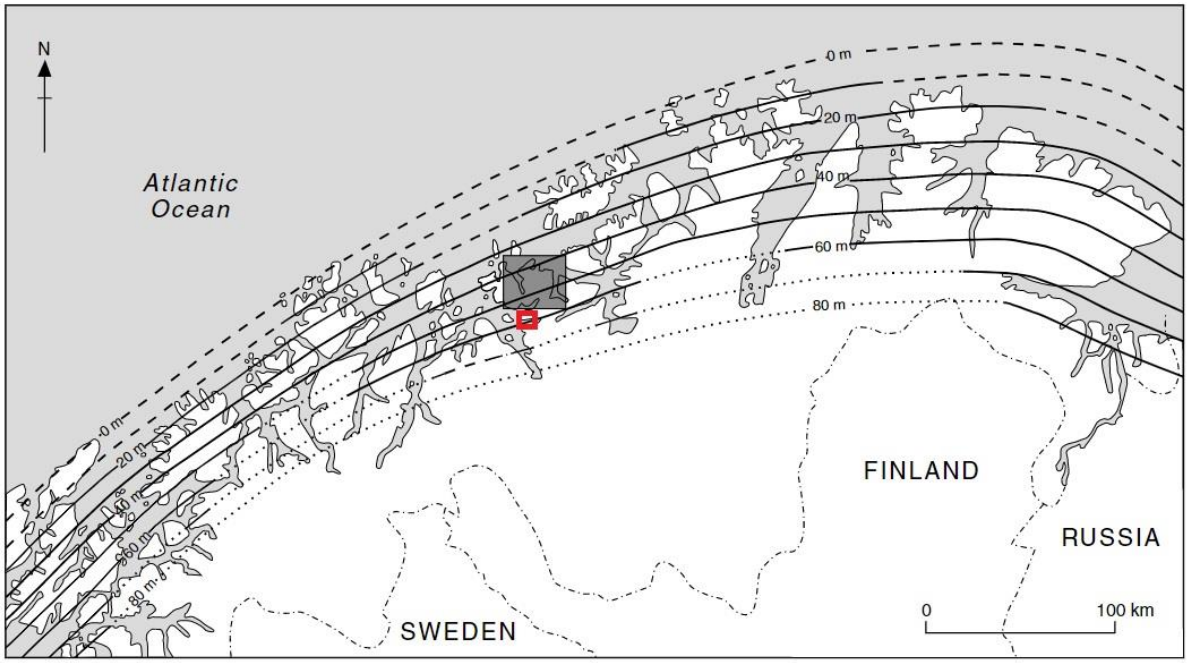

Figure 20: Map depicting isobases for the Main shoreline, after Marthinussen (1960). Red square show Dusnjárga, Solid lines indicated by dated raised marine evidence, while there is a lack of evidence in areas with broken line. Line with dashes is offshore, while dots is onshore. Black polygon is not of relevance to this thesis.

4 Data and methods

A lot of information and data is necessary when investigating an unstable rock slope. All data compiled from external sources and gathered from the field, along with different methods used for interpretation purposes will be listed and explained in this chapter.

4.1 Datasets

4.1.1 Fieldwork

The purpose of this fieldwork was to gather as much information as possible from the rock slope before winter set in. In my case, structural measurements were of priority, along with identification of morphological features and acquiring drone photos from the area. In addition to my own work, I also helped two fellow students with rock-sampling for their thesis. Field work was started early September and lasted until the 10th of October 2021, with five trips to Dusnjárga, each lasting between 3–6 days.

4.1.1.1 Structural measurements and morphological elements

Sampling of structural measurements was done with the app Clino Fieldmove (Limited, 2021), downloaded to an iPad from Google Play. Structural measurements like foliation, joint sets, faults, and such were of particular interest. Identification of morphological structures and exploration of the extent of the slide was also of high interest. Linking controlling structures to morphological elements was an essential part of the fieldwork. In total data was gathered from 3511 structural measurements that is used in this thesis. 2294 of these structural orientations are my own measurements, while the remaining 1217 are from co-students Emilie Jensen Aamodt and Andreas Grumstad, who joined me in the field, and from previous fieldwork done by prior students Frederic Blau and Ellen Tyldum Skogen in the same area.

In addition to my own sampling of structural data, NGU shared newly acquired bathymetry data from the shallow marine areas outside of Dusnjárga. Data that will be used to continue the morphological mapping under sea level and get an accurate assessment of where the basal rupture surface daylights.

4.1.1.2 Drone imagery

Drone photos were needed to make a detailed digital elevation model (DEM) from photogrammetry, while also providing a detailed overview of the slope. A DJI Mavic pro drone was used, with a 2.3" CMOS 4k camera and a 28mm f/2.2 lens with a 78.8° field of view. Drone flights were performed 8th–10th of October, in order to wait for a lower density in vegetation. Due to challenging weather, limited days with the drone and limited battery capacity, only the eastern part of the targeted zone was covered, which luckily was the part with more morphological elements. The flight-route was done with the DroneDeploy app (DroneDeploy, 2021) and executed over two days where light conditions were as consistent as possible. A total of 13 GPS-measured ground control-points (fig. 21) were placed throughout the planned flight-area to have an additional positional reference to the drones built-in GPS.

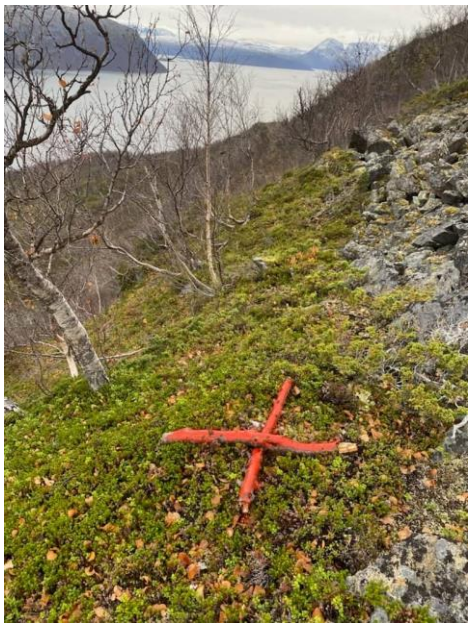

Figure 21: Ground control points for additional positional reference of the photogrammetry-map. A total of 13 ground control points were set, evenly distributed throughout the eastern side of the transition zone. The points were made up by logs sprayed with red paint for good visibility from the air. Each point was manually measured for its location by GPS. To get a precise location, the GPS lay in the middle of the intersecting logs for 5 minutes before the coordinates was written down. Photo: Simen Bekkevoll

A total of 1551 photos were taken along the set flight route (Fig. 22-B), while an additional 666 available photos of the western part of the transition zone was supplied by NGU.

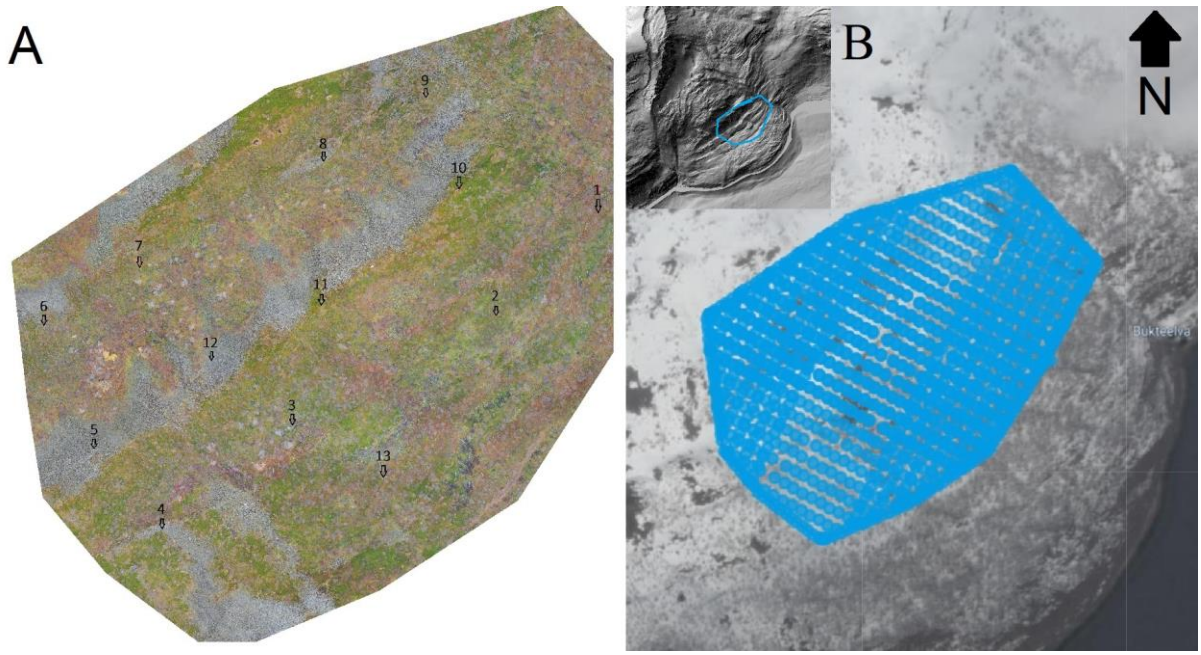

Figure 22: A) A detailed orthophoto captured with the drone. The small, numbered arrows show the exact location for the measured GPS-points. B) Screenshot of the flightpath and aerial photo from the Dronedeploy app (DroneDeploy, 2021). The flightpath followed the blue dots in a cross-pattern getting shots from various directions, with a constant angle of incidence and maintaining a 100-meter elevation above the ground below.

4.1.2 Satellite-based InSAR data

InSAR data used in this thesis comes from the public service *InSAR Norway (NGU, 2018)*, a service launched in 2018 with InSAR datasets available for the public. InSAR Norway uses a method called Persistent Scatterer Interferometry (PSI), which utilizes stacking interferograms to search for pixels containing dominant persistent scatterers. The result is a network of persistent scatterers (fig. 23) showing displacement rates along LOS. The Sentinel-1A and -1B satellites from the Copernicus program gathered the data used in this thesis between 2015 and 2019. Each satellite has a return period of 12 days, but since their field of view is overlapping, a return period of 6 days is possible (NGU, 2019). There are

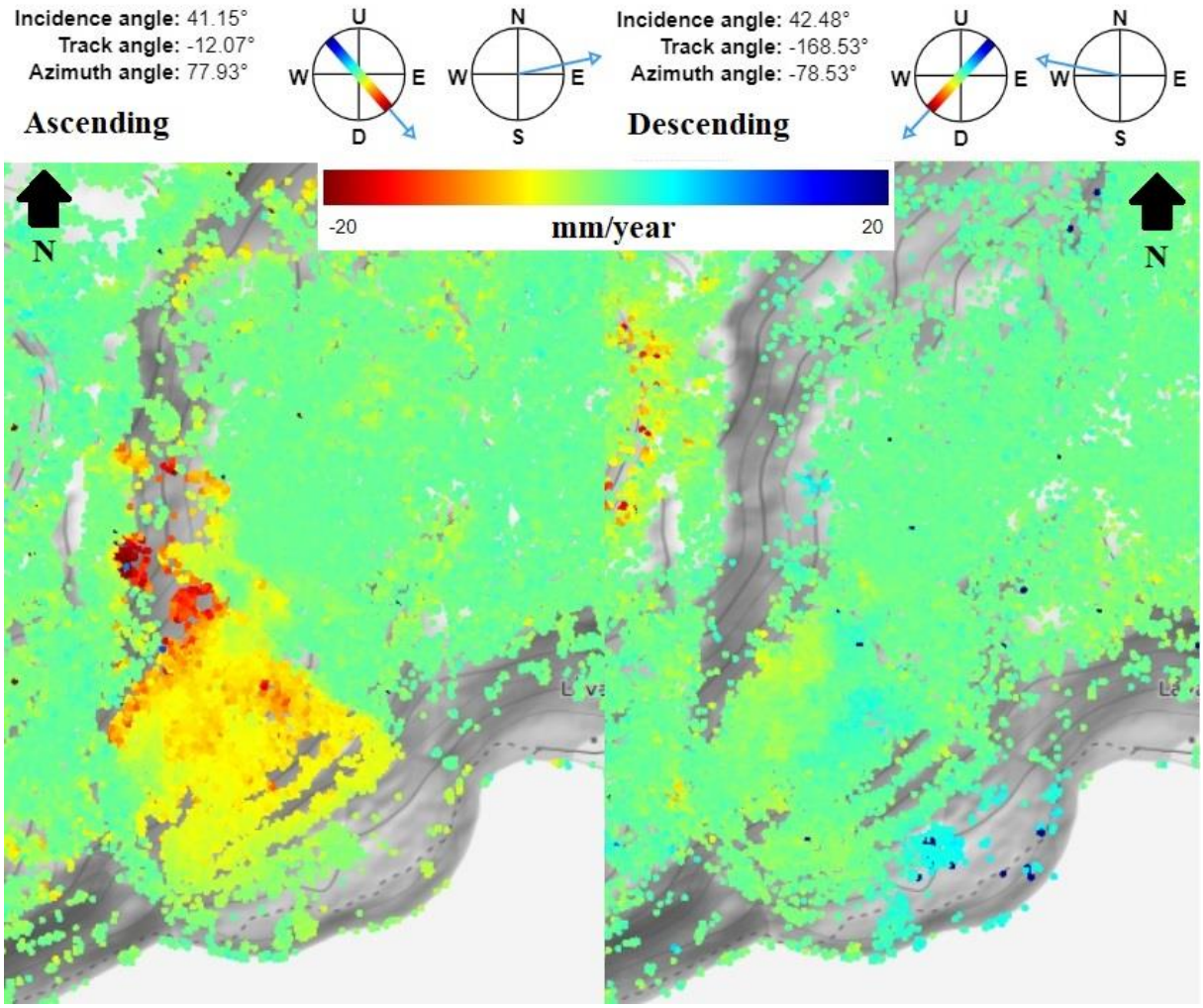

Figure 23: A single geometry display of displacement rates at Dusnjárga, adapted from: https://insar.ngu.no/(NGU, 2018). Figure shows the displacement along LOS from both ascending and descending geometries. Colours display movement towards respective LOS (blue colour) and away from LOS (red colour, in millimetres per year. Each satellites direction of LOS can be seen from the top of the figure, ascending LOS being towards ENE (East-Northeast) and descending LOS being towards WNW (West-Northwest). Incidence angles, track angles and azimuth angles are also displayed.

The path of the Sentinel satellites is in a polar oriented orbit, which makes SAR-imagery increasingly overlap the higher the latitude. This results in three available datasets for Dusnjárga, each with a small unique change in LOS (NGU, 2019), which makes it possible to compare datasets based on which LOS compliments the geometry of Dusnjárgas slope best.

4.1.3 Ground-based InSAR data

Data gathered by the GB-radar (fig. 24) at Dusnjárga was supplied by NVE and sampled during a 56-day period from the 17 July to 11 September 2019. The GB-radar data shows displacement from a single geometry and has to be merged with the InSAR geometries in order to get proper directional movement of the slope.

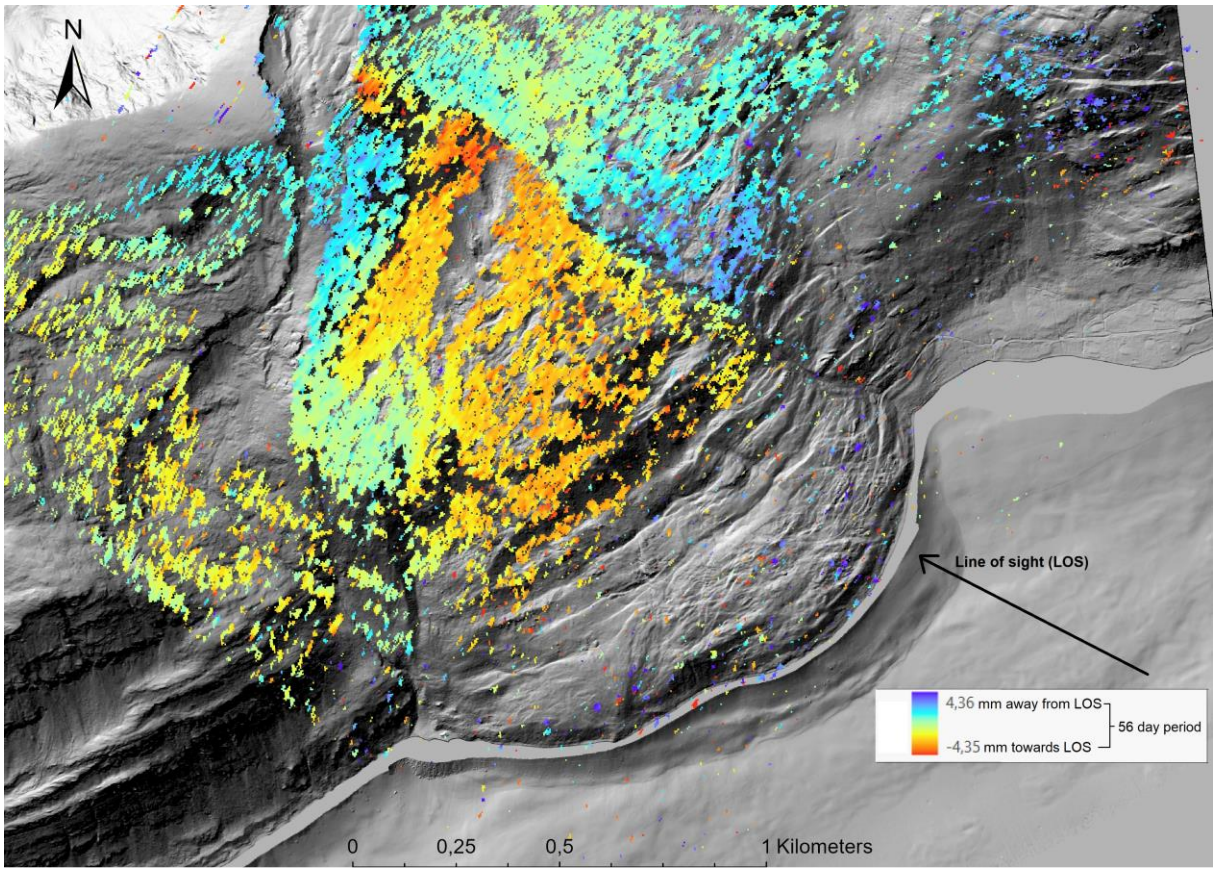

Figure 24: Input data from GB radar, provided by NVE. Legend shows how many millimetres the slope moved away or towards the LOS during the 56-day period of monitoring. The ground-based radar, in which the LOS was directed from, was located about 2 kilometres across the fjord, marked with the black arrow. Background: hillshade from 1 meter DEM (Kartverket, 2021).

4.1.4 dGNSS data

All data involving dGNSS measurements belongs to NGU and NVE. Dusnjárga has been considered as an unstable slope of interest and monitored with dGNSS by both NVE and NGU. The slope shows features linked to gravitational deformation and has local changes in displacement rates at certain areas. (Redfield et al., 2011).

Available data from 10 different dGNSS points from in or around the mountain slope of Dusnjárga is mentioned in this thesis. They are located from the head of Dusnjárga and all the way towards the foot of the deformed slope. Some locations have a displacement rate which falls short of the uncertainty set as 3σ (uncertainty "σ" times 3, as explained in chapter 2.4), which means that their data is inadequate for affirming a gravity-driven deformation. Other locations show noticeable displacement that exceeds the uncertainty with a good margin, thus allowing more interpretation. Uncertainties of vertical displacement will be bigger than that of a horizontal displacement, since atmospheric variations affect the accuracy in the z-axis more than the in the x- and y-axis. DUSN_GPS_01–DUSN_GPS_03 was measured for seven years from 2007–2014 in relation to the "ROS fjellskred i Troms" project by NGU (Redfield et al., 2011). DUSN_GPS_04–DUSN_GPS_08 was measured during a one-year period between August 2020 and September 2021. The dGNSS points from NGU displays the average annual displacement. The two dGNSS measurements from NVE stems from a one-year period between the start of January 2021 to the end of December 2022, and contains time series, showing weekly variations in displacement.

4.2 Methods

4.2.1 2D InSAR

2D InSAR is, as explained in chapter 2.3, a method where displacement measurements from two different satellite geometries are combined, in order to view displacements on ground level on a millimeter scale. To view 2D displacements, a Geographical Information System (GIS)-compatible tool, developed by NORCE in 2020 (Lauknes et al., 2020) was employed (Sandbakken, 2021). The tool is utilized in ArcGIS Pro and combines displacement data from overlapping SAR imagery with both ascending and descending LOS to estimate a combined annual mean velocity, called combined surface displacement (CSD). The tool computes CSD-points from intersecting ascending and descending datasets and displays them on a map. If the direction of a slope deformation is anticipated, displacement data can also be viewed as vectors along a chosen profile.

Alignment

To compute a CSD, the used datasets need to be spatially aligned, since measured points from descending and ascending datasets usually do not align perfectly. By setting a sample intersection radius for the dataset-points, it is possible to create CSD-points where the point-radius from different datasets intersect (fig. 25) (Lauknes et al., 2020).

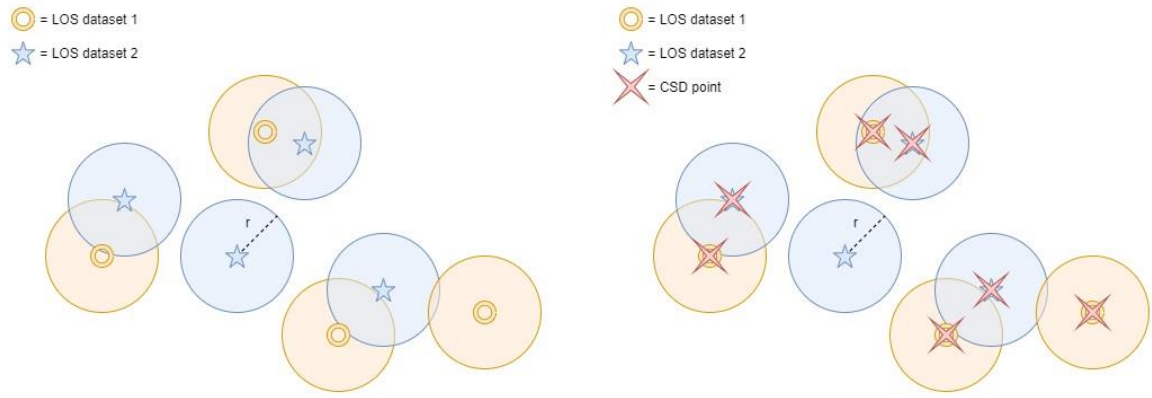

Figure 25: The position of points from different datasets will not stack perfectly. The sample intersection radius around each point allows for CSD points to be computed at each dataset-point that intersects the radius of another dataset-point. Source: (Lauknes et al., 2020)

When utilizing the GIS-tool, a sample intersection radius is manually set to a value that indicates how big an area data-samples will be gathered from. If the sample intersection radius is set too big, the generated CSD point might combine data from vastly different targets, which makes for a less accurate deformation rate. If the sample intersection radius is set narrow, deformation measurements will be accurate. But setting a narrow radius also risks no overlapping point-radiuses, hence no CSD points.

The tool allows for three different interpolators to be used in computing the data from LOS points into CSD points. For these InSAR simulations the Weighted Neighborhood interpolator was used which interpolates the LOS data into CSD points by taking the average measurements from neighboring points within a set radius (Lauknes et al., 2020).

Calibration

Before generating CSD points, it is important to calibrate the single geometry datasets relative to each other, which can be done by finding a mutual area of zero, or as little displacement as possible (Lauknes et al., 2020). For the calibration of the 2D InSAR calculations done in this thesis, a polygon was drawn on a stable mountain area west of the backscarp of Dusnjárga, which showed close to zero displacement and included points from all datasets used.

Regularization

If the InSAR satellite's line of sight doesn't cover all dimensions needed, a regularization, or assumption is needed to get a CSD estimation. InSAR satellites are orbiting in a north-south oriented direction while looking west-east. As mentioned in chapter 2.2, information about displacement is often missing in the northern direction (Lauknes et al., 2020), which is why an assumption of a zero-movement direction is then needed in order to get a proper display of the CSD. This can be done several ways in the toolbox. A direction such as north/south can be set as constantly being zero, a direction along a compass bearing (degrees relative to north) can be set as constant zero and there is also the possibility for drawing a line along the slope, where the direction parallel to the line is set as zero movement. CSD points generated in the GIS-tool will get a conditioning number between 0 and 1, which is based on how well the measured point is supplemented by satellite geometries in relation to the "blind" directions, which for the Sentinel satellites are roughly north.

Using 2D InSAR profiles for interpreting longitudinal displacement trends

It can be challenging to identify the extent of geomorphological elements in the field. On a deformed rock slope, superficial materials may cover parts of the morphological structures, making them hard to recognize, while secondary structures may appear inside primary structures, making it a highly complex slope (Sandbakken, 2021). By using 2D InSAR cross-sections with estimated deformation rates, one can get a better understanding of how movement along the basal-rupture surface is linked with morphological elements and what structures control the deformation (Eriksen et al., 2017, Böhme et al., 2018, Frattini et al., 2018).

When using InSAR for measuring displacement rates, there are mainly four different factors that affect the longitudinal variations along any kind of landslide. Which is; geometry of the rupture surface, both the rear and the basal; the direction of LOS relative to changes in displacement vectors along the slope; secondary landslides or other features such as rock glaciers, scarps or solifluction inside the main body (fig. 26-f, g, h, i, j); and mechanical and local variations in heterogenous materials within the slide (Frattini et al., 2018). With these factors in mind, it is possible to interpret landslide-kinematics from measured displacement rates (Ambrosi and Crosta, 2006, Cascini et al., 2010, Schlögel et al., 2016, Eriksen et al., 2017).

A large change in negative vertical displacement values can suggest for a sub-vertical dominated movement in that area, perhaps by a scarp or secondary landslide. A change in positive vertical displacement suggests for an upwards movement of the slope, which can be the case for rotational toe-domains or compressed toe-domains where layers are thrusted upon each other (fig. 26-h, j) (Frattini et al., 2018).

At the circular centre of a rotational slope or between the extensional and compressional parts of the transition zone in a biplanar slope, the overall displacement can be close to zero. If the dominant superficial slope movement changes from vertical to horizontal it can be due to the slope changing from a rotating/roto-translational movement, to following a planar or sub-planar basal rupture surface, which can happen if the main parts of the slide have a homogenous movement (Frattini et al., 2018).

Internal rock mechanics can also play a part in how displacement vectors are shown, a brittle scarp for instance can have an abrupt change in vertical displacement rates, while a more ductile progressively deformed scarp can have a more gradual, curved displacement trend. Rotational displacements (fig. 26-d, j) can often show greater variations and more complex changes along its longitudinal profile compared to translational, more simple, planar or biplanar basal rupture surfaces (fig. 26-a, b) (Frattini et al., 2018).

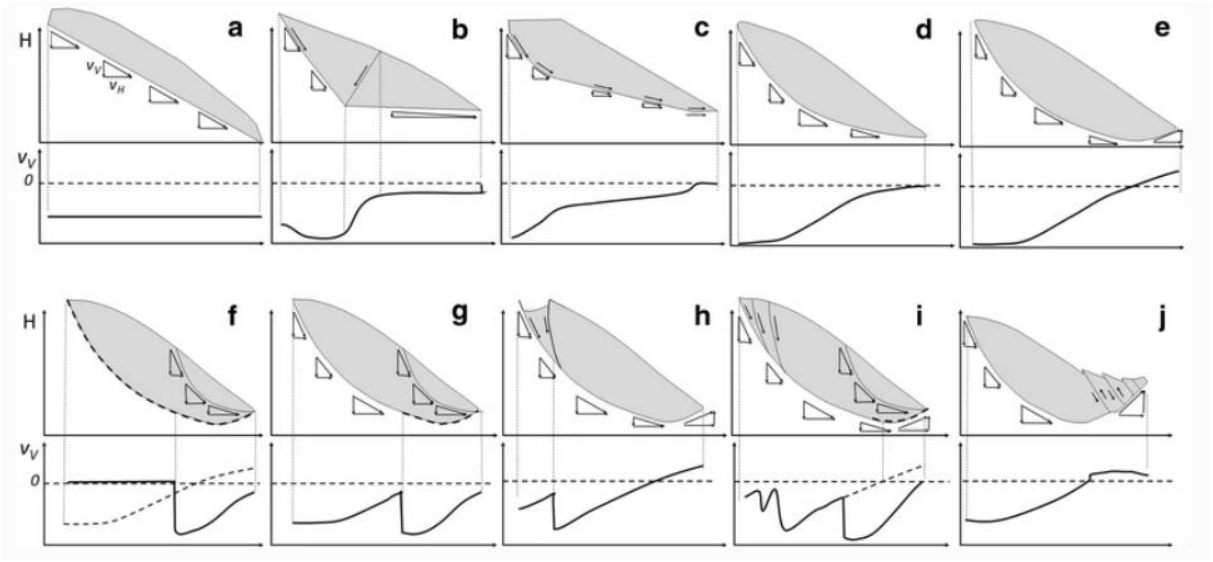

Figure 26: Sketch of how the structural variations of large slope instabilities and internal gravity driven phenomena can affect the vertical velocity measured on the slope surface. Black line underneath the figures shows the change in mean vertical velocity along the profile. ***a), b)*** *Translational slides, a planar slide and biplanar compound slide respectively.* ***c)*** *Roto-translational slide****, d), e)*** *Variations of rotational slides.* ***f) g)*** *Rotational slides with varying activity along the basal rupture surface and in internal secondary landslides.* ***h), i)*** *Variations of rotational slides with semi-graben, multiple scarps and active secondary landslide.* ***j)*** *Rotational slide where the toe is broken up in slices and thrusted upwards. Source: (Frattini et al., 2018).*

In order to verify the concepts from figure 26, simple finite element simulations along a constant slope gradient (fig. 27) has been performed with emphasis on variations in failure surface and specific common landslide structures, such as backscarp and a compressed fractured toe (Nithiarasu et al., 1977, Griffiths and Lane, 1999, Stead et al., 2006, Frattini et al., 2018). These simulations are examples, based on simple geometries and do not cover all possible geometrical examples, but can serve as a baseline for interpreting rupture-surface geometries.

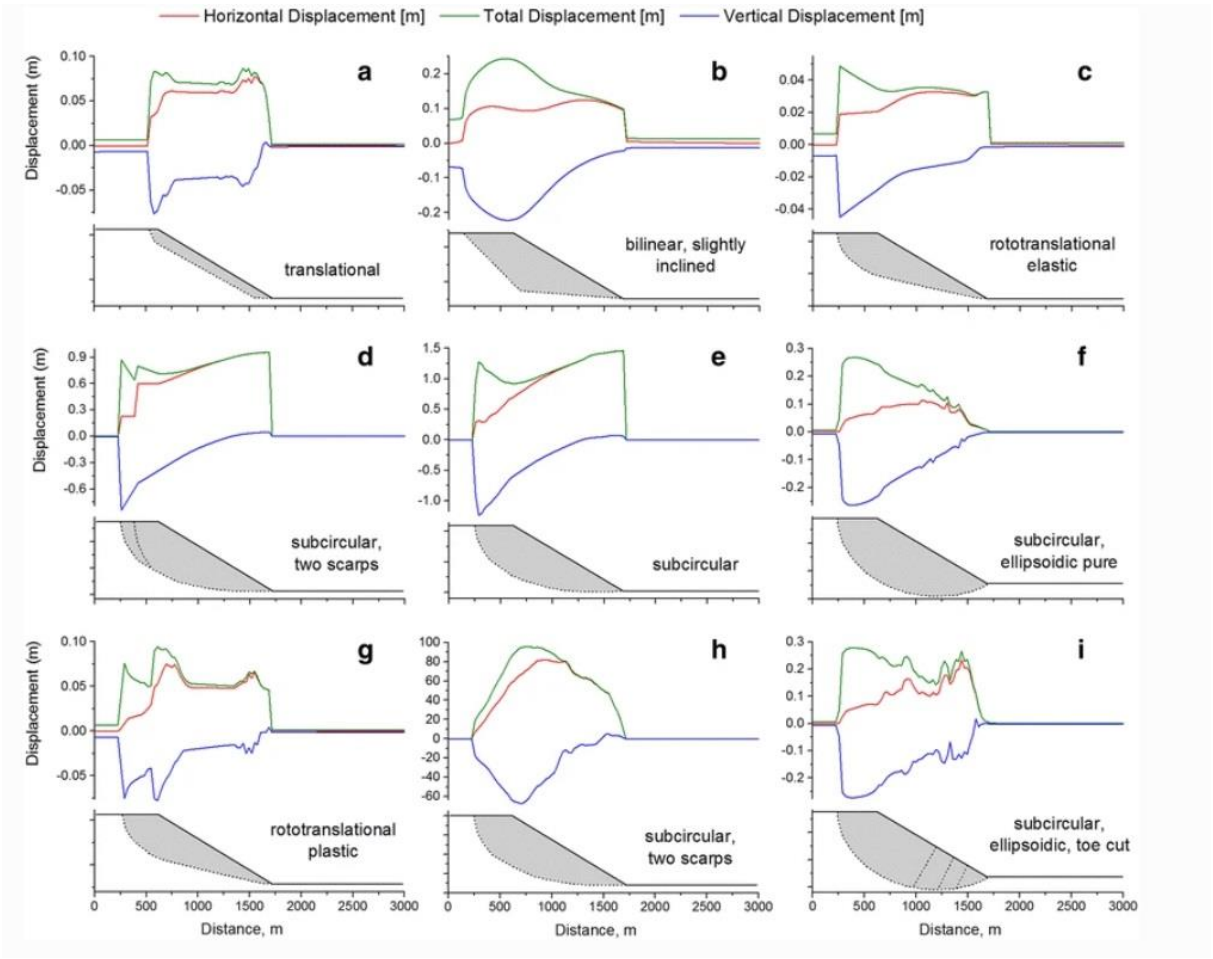

Figure 27: Two-dimensional finite element simulations along a constant slope, depicting different rupture surfaces and typical landslide structures. Horizontal, vertical and total displacement are shown along examples of different slope failures. Source: (Frattini et al., 2018)

4.2.2 3D InSAR

When making a 3D InSAR map of a rock slope, a third source of data, along with the two satellite sources, is needed for the full three-dimensional display. This is typically done with a GB-radar (Fig. 8) that measures displacements along a LOS with different orientation compared to the satellites. Sentinel-1 InSAR data was captured during a 5-month period from the start of June until the end of October each year (2015–2019), while the GB-radar captured data during a 56-day period in the summer of 2019. The discrepancy of temporal measurement windows is an important limitation to consider when comparing and combining various data sources. Satellite InSAR mean velocities from InSAR Norway are based on an assumption of near-linearity through the year, which means that GB-radar data must also be calibrated to an annual movement rate to match the satellite data. Interestingly enough, dGNSS stations from NVE

with a one-year time series, indicate that displacement at Dusnjárga is seasonally controlled and have 2 months of active deformation (fig. 28).

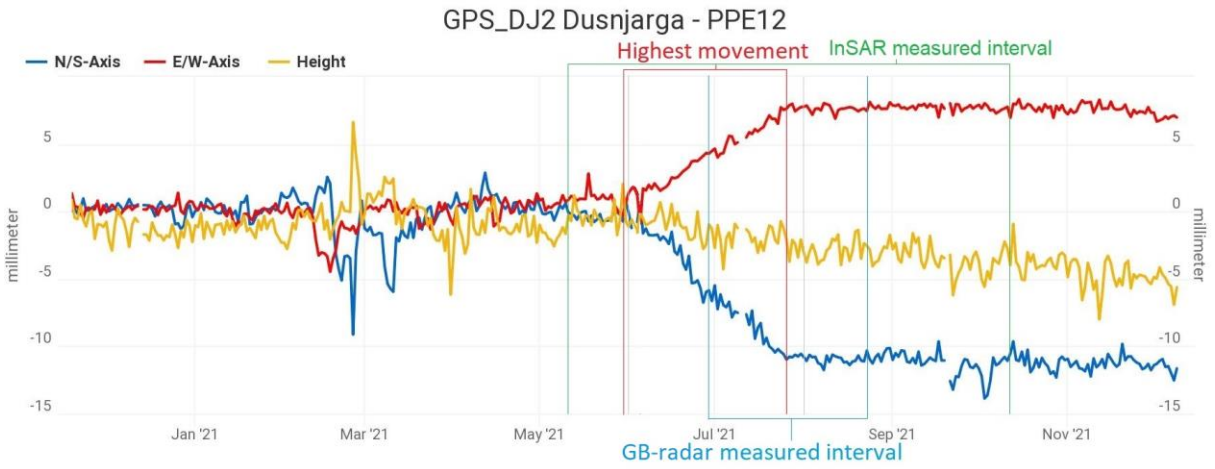

Figure 28: A time series of NVE'S dGNSS station, located in the central domain. An active period between the middle of June to the middle of August can be seen. Green writing with "InSAR measured interval" is the timeframe for InSAR satellite data, while GB-radar measured interval is the time frame for GB-radar measurements. Provided by NGU.

The GB-radar data covers half of the active period over a sub-2-months period, while satellite data covers both 2 months of active deformation over a period of 5 months. When the GB-radar data is calibrated to annual displacement, it has 20 % higher annual displacement than the satellite data, since half of the period with GB-data measurements was during the period of active deformation, versus 2/5 for satellite InSAR. After adjusting for the seasonal active period, displacement vectors seemed to align better with the expected direction of movement of the slope.

Calibration of the 3D InSAR datasets had to include points of small to zero movement from all three datasets. Unlike regularization of 2D InSAR, the assumption of a zero-displacement direction is not needed, since we have sources covering all three dimensions. Regularization is therefore set as "none". 3D InSAR will give the true displacements along the slope, without relying on calculated assumptions as in 2D InSAR. If visualized understandably, 3D InSAR will display how displacement rates and orientation changes throughout the slope, which can then be linked with morphological structures. Sample intersection from table 3 was changed to 1 for the 3D display, in order to get a readable and structured displacement map.

Table 3: Inputs for 3D InSAR using GIS-tool, as well as the dip and velocity figures (fig. 58-A, B).

	3D InSAR	3D InSAR (Dip only)	3D InSAR (Velocity only)
Calibration area	Calibration 3D Insar	Calibration 3D Insar	
Calibration percentile	50	50	50
Sample Intersection radius	1	3	3
Interpolator	Weighted neigbourhood	Weighted neigbourhood	Weighted neigbourhood
Neighbourhood radius [m] (weight)	[10] (uniform)	[10] (uniform)	[10] (uniform)

There were less CSD points on the 3D model than what was available on the 2D model, due to each "point" on the ground now having to register at three different LOS's instead of two. The LOS of the ground-based radar hits the lower altitude-areas, such as the toe-domain, at less optimal angles than the LOS from the SAR satellites. This along with the lower areas being relatively dense in vegetation means that only the central domain and some parts of the head and transition zone are covered.

4.2.3 Photogrammetry

The transition zone is perhaps the most interesting section of the slope. The slope changes drastically from a steep slope with large extensional morphological structures to a flatter section containing sporadic compressional features towards the toe. Therefore, a thorough examination of the transition zone was desired to better cover its change in morphological structures and kinematic patterns. A DEM of 1 meter accuracy was the elevation model of highest resolution available for Dusnjárga, so a drone was used to construct a DEM with finer resolution of the transition zone.

The software DroneDeploy was used for planning the flight path and getting optimal pictures with >80 % overlap and taken at an angle of 65 degrees from several different directions. The result of the flight was first reviewed in the DroneDeploy software where las files, point cloud files and a 3D view of the slope was extracted.

The software Cloudcompare was used for "cleaning" point cloud files of vegetation and noise. Rendering of the whole area in ultra-high definition took 6 days, with 1,5 billion points to render. Rendering and editing of such large data-files were very time consuming and required a certain level of computer-performance. Valuable help with the photogrammetry was given by Pierrick Nicolet at NGU, who processed and provided the final DEM data. Vegetation and other noise, both above and below ground level were filtered out as well as possible by testing different scalar field values. Filtering out all vegetation was unsuccessful, remaining vegetation

can be seen as small “dots” spread out through the hillshade on fig. 29. The created DEM was of 20 cm resolution.

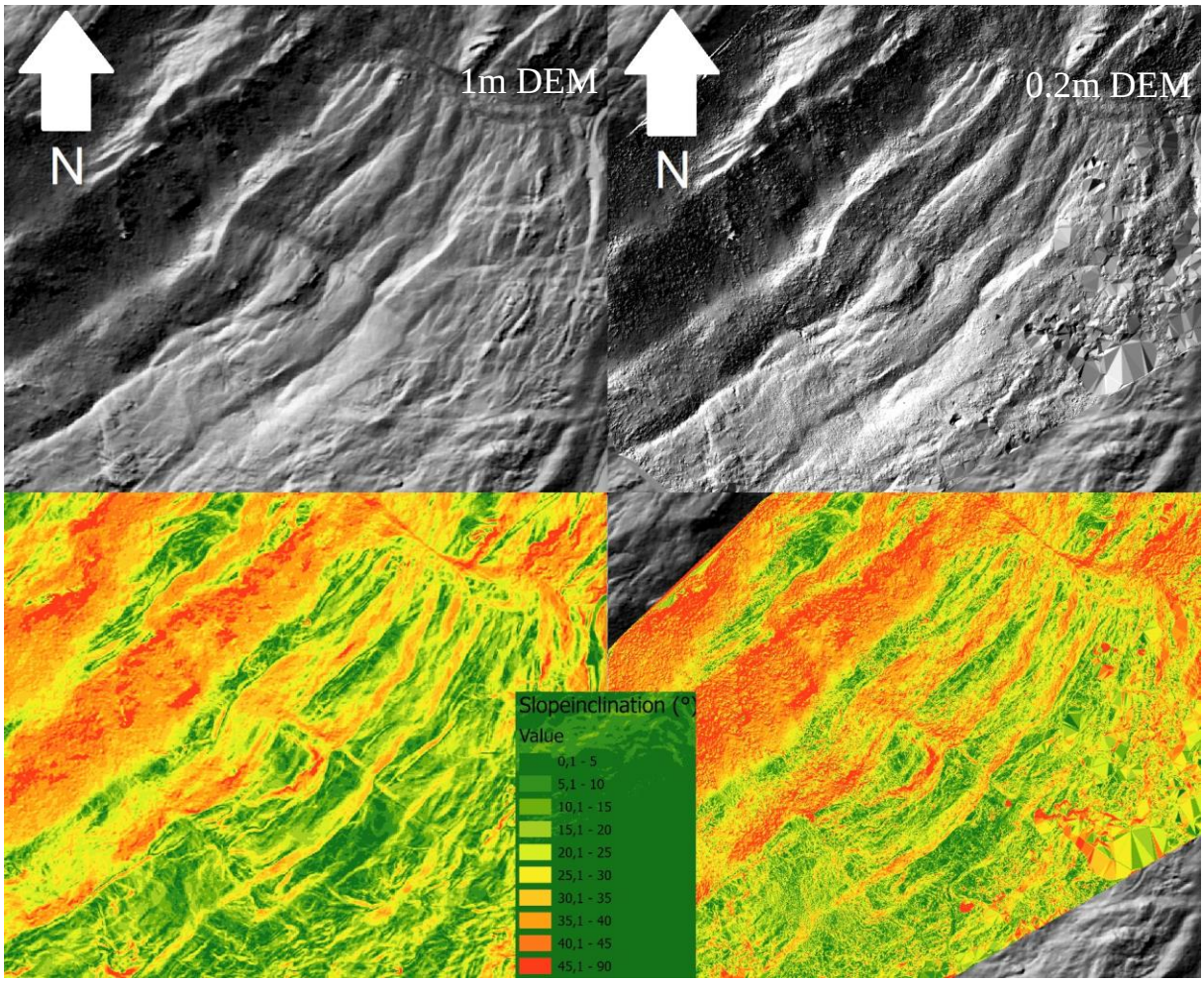

Figure 29: Top left is a hillshade-map overlaying the 1m DEM (Kartverket, 2021) of the eastern part of the transition zone, with a slope-inclination map underneath. Top right is a hillshade-map on a 0,2m resolution DEM made with drone-pictures. Below is a slope-inclination map based on the 0,2m DEM. To the bottom right of the hillshade-map there is visible noise we were unable to filter out.

4.2.4 Morphological mapping

Morphological mapping was done to get a better understanding of the extent of the unstable rock slope, to link morphological elements to longitudinal displacement rate variations and to determine what structures are controlling the deformation. For the morphological mapping, remote observations from orthophotos, drone footage, slope-inclination- and hillshade-maps (created in ArcGIS Pro) were used in combination with notes and observations from the field.

A morphological map without much interpretation, focusing on observed slope-changes throughout Dusnjárga and areas around was firstly created. In addition, a morpho-structural map with interpreted morphological structures (fig. 30) from the deformed slope, was created to better depict gravitational-driven features from each domain.

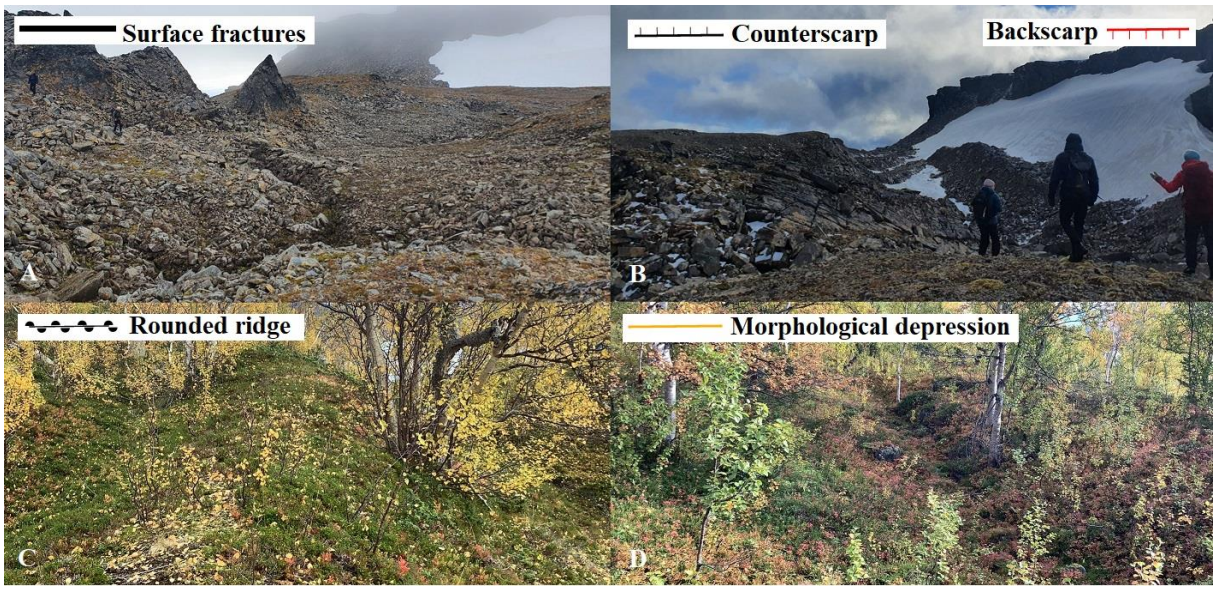

Figure 30: Selected morpho-structures from the deformed slope with belonging symbology. A) Surface fractures from the head domain. B) A large backscarp to the right, with its counterscarp to the left of the trench running between them. C) Rounded ridge on a terrace from the transition zone. D) A morphological depression from the toe domain. Photos: Simen Bekkevoll

Surficial material distribution below the head domain has also been mapped, separated into three different categories, densely vegetated areas, lightly vegetated areas, and disintegrated rock without vegetation. Densely vegetated areas represent all areas with both trees and vegetation covering the ground. Lightly vegetated areas represent locations where hummus, moss etc., covers most of the ground, without the presence of trees. Lastly the disintegrated category includes both rock fields with highly disintegrated material and rockfall/scree from steeper sections of the slope. Sites with un-vegetated disaggregated rock is found evenly distributed throughout the eastern side of the slope, while they are a little harder to find on the western side.

5 Results

The slope of Dusnjárga extends for over 2 kilometers in length and is about 1,5 kilometers in width at its broadest. To study the entire slope, it is necessary to separate it into manageable domains (fig. 31). The uppermost part is hereby termed the head domain, below this is the central domain, followed by the transition zone and the toe-domain in the lowest part of the slope. The transition zone is a part of the slope where the inclination transitions from a steep mid-part to the less steep toe below, with complex structures large lineaments perpendicular to the velocity direction. Surface cover distributions has been mapped in figure 32.

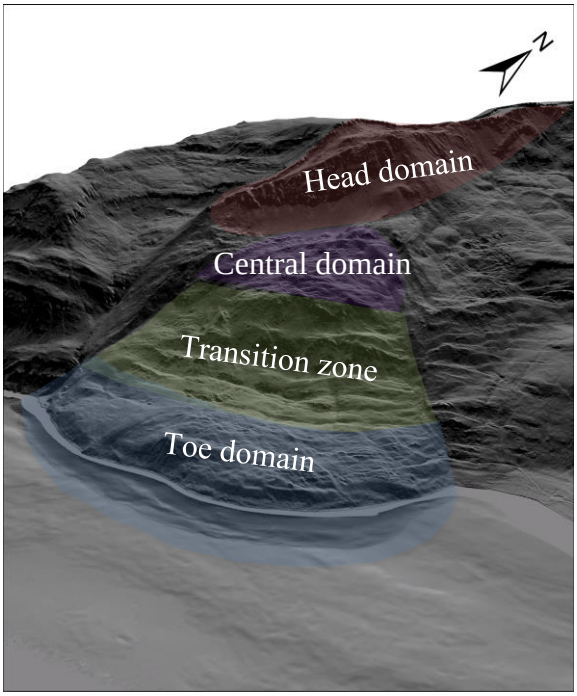

Figure 31: 3D hillshade-map from 1 m DEM (Kartverket, 2021) showcasing the four different domains at Dusnjárga.

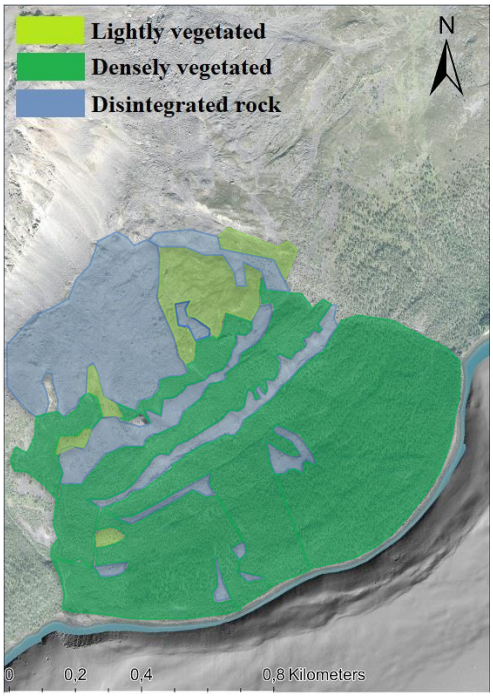

Figure 32: Surface cover distributions below head domain. Categories are explained in chapter 4.2.4. Orthophoto: (Kartverket, 2015).

5.1 Morphology of rock slope deformation

A large-scale geomorphological map of the entire slope with surrounding areas (fig. 33) focusing on displaying slope changes and a geomorphological map of smaller scale (fig. 34), covering the transition zone has been produced, along a map presenting morpho-structures for each domain.

5.1.1 Geomorphological map

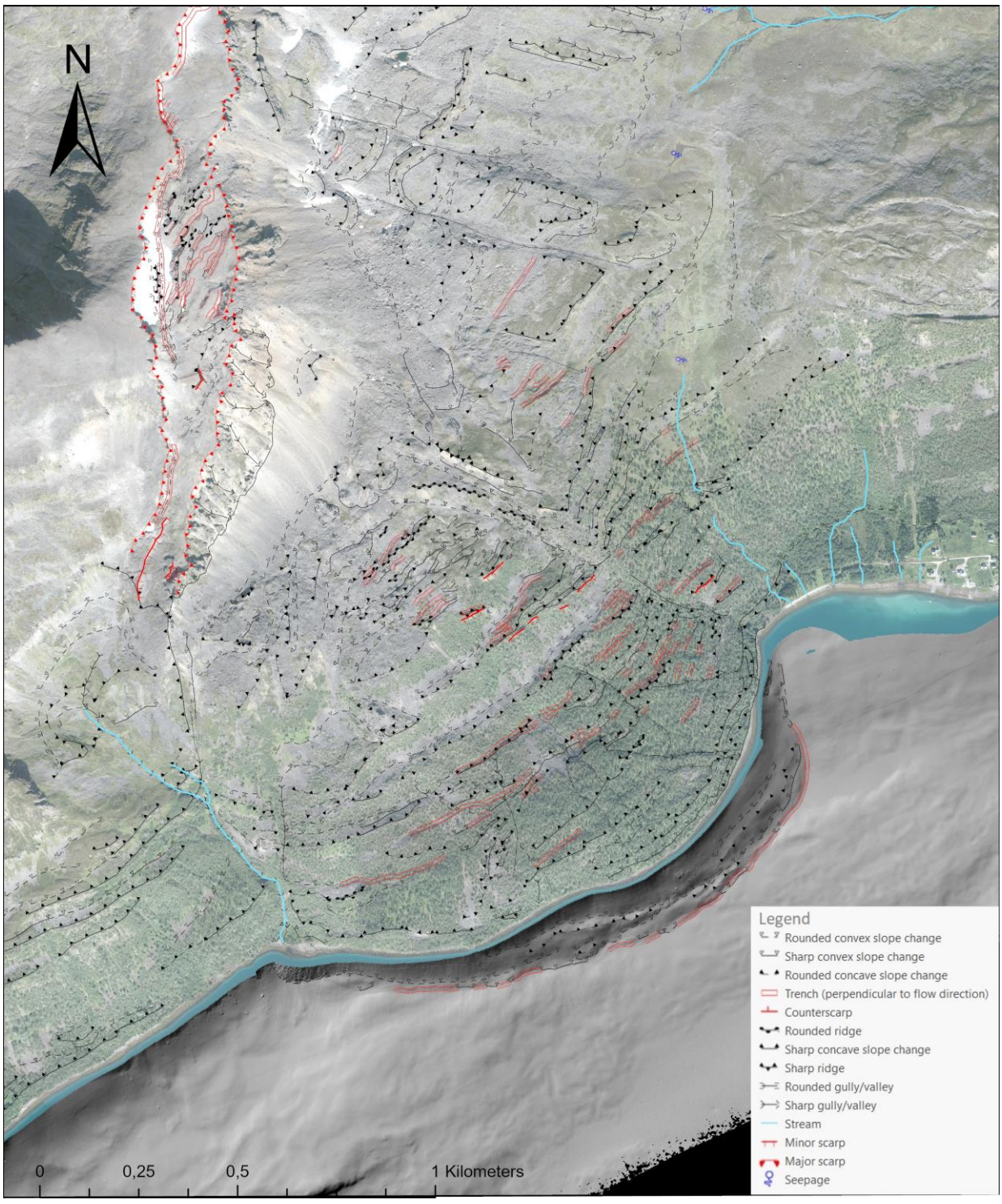

Figure 33: Geomorphological map of the study area woth orthophoto in background (Kartverket, 2015). Red symbology indicates morphological features that clearly shows signs of gravitational deformation, while the black symbology represents slope-changes, or possible gravitational features.

Gullies and trenches are both morphological depressions but mapped separately by their orientation. Trenches are in this case oriented perpendicular to the slope movement, while gullies are oriented parallel or sub-parallel to the slope movement. Slope changes are characterized by sharp or rounded shapes. Continuous streams seem to be absent in the deformed slope, although in seasons with melting/high precipitation it is possible that water could run in some of the gullies. Below sea level there is also noticeable slope changes, especially in the middle and eastern parts where you have a flatter section halfway down the slope. Due to the complex nature of the transition zone, a detailed mapping (fig. 34) was performed to better understand how slope kinematics change in this area.

5.1.2 Detailed geomorphological map of the transition zone

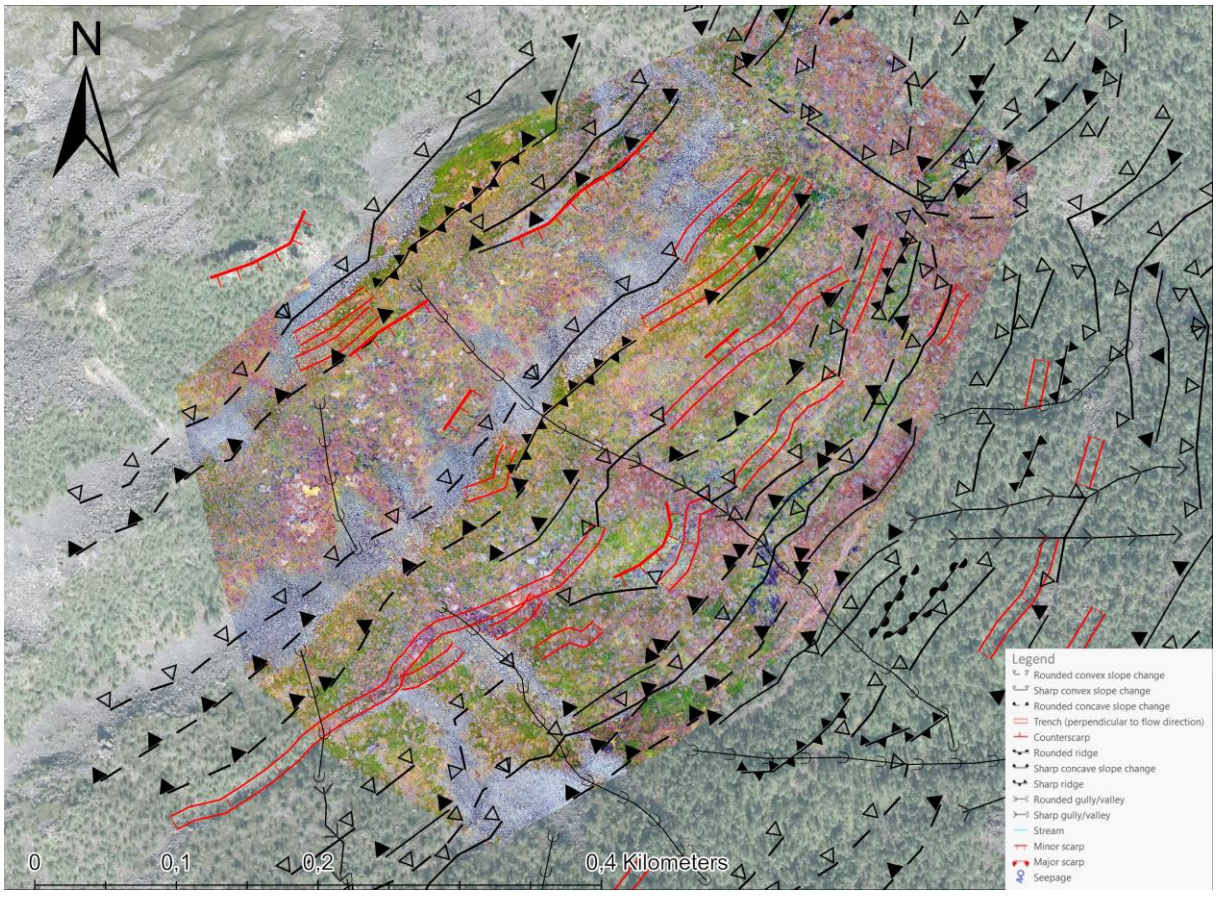

Figure 34: Geomorphological map of the transition zone. A detailed orthophoto captured with the drone is overlaying an aerial-photo in the background (Kartverket, 2015).

5.1.3 Morpho-gravitational structures

The head domain sits between 800 m.a.s.l. and 500 m.a.s.l. The uppermost backscarp separates the area of deformation from the stable mountaintop to the northwest. The block below is offset along the scarp by between 20 and 50 meters at approximately 70 degrees. The block is large (170000 m²) and limited by two major scarps with north-south trending orientations (fig. 35). In front of the backscarp a trench that has a varying width of 10–20 meters follows parallelly to the backscarp, with a counterscarp on the opposite side. Across the offset block there are several smaller morphological depressions and counterscarps (fig. 36), oriented in a sub-parallel direction to the larger structures in the area, oriented in an NNE-SSW direction. Below the large block a second major scarp runs sub-parallel to the backscarp and separates the head domain from the central domain. This major scarp ranges from 150 to 230 meters in height. The scarp dips at 45 degrees and is mostly obscured by unvegetated talus/scree.

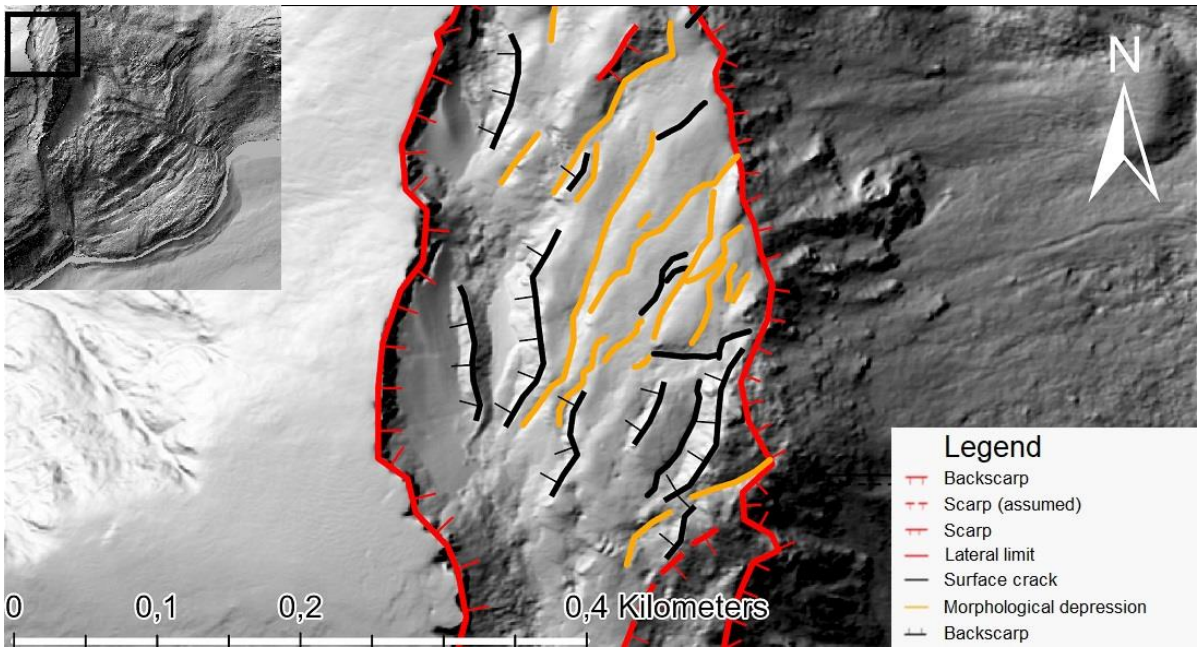

Figure 35: Morpho-structures found at the head domain. Between the two major scarps there are series of morphological depressions, some surface fractures, and counterscarps with parallel to sub-parallel orientations. Maps on a 1:4500 scale. Hillshade from 1 m DEM: (Kartverket, 2021).

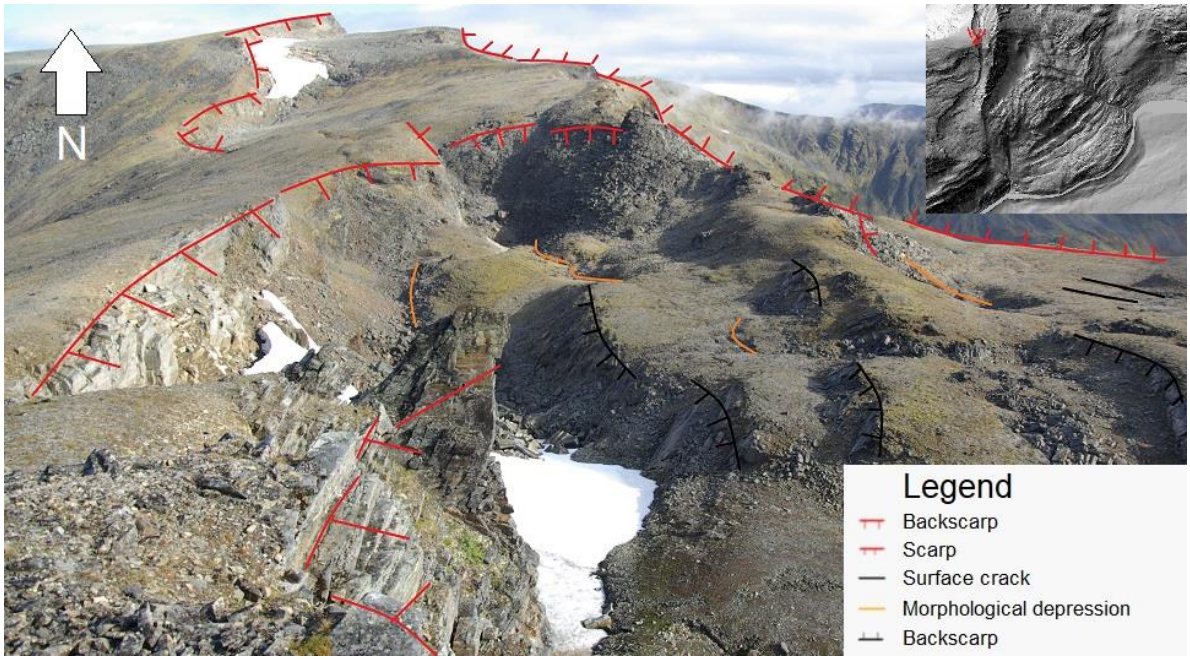

Figure 36: Displaced head block between the two north-south trending major scarps. A selection of morpho-structures from the head domain have been included in the figure. Location of photo and direction of view is shown as red dot on the map in top right corner. Photo by: NGU.

The central domain of the deformed rock slope stretches between 550 and 350 m.a.s.l. and is 260000 m^2. The upper part of this domain is dominated by disaggregated rocks and has few outcrops with bedrock. Sub-circular oriented scarps that transition to the lateral limit is found at the start of the domain (fig. 37). Several ridges and local depressions appear in the central area (fig. 38), along with subtle convex/concave slope changes. The western area has more disintegrated rocks than the eastern side, while the eastern side has parts covered by vegetation. The eastern part shows more structural lineaments than what is present in the western areas. The central domain end at about 350 m.a.s.l., just before the slope-inclination gets steeper and transitions into the transition zone.

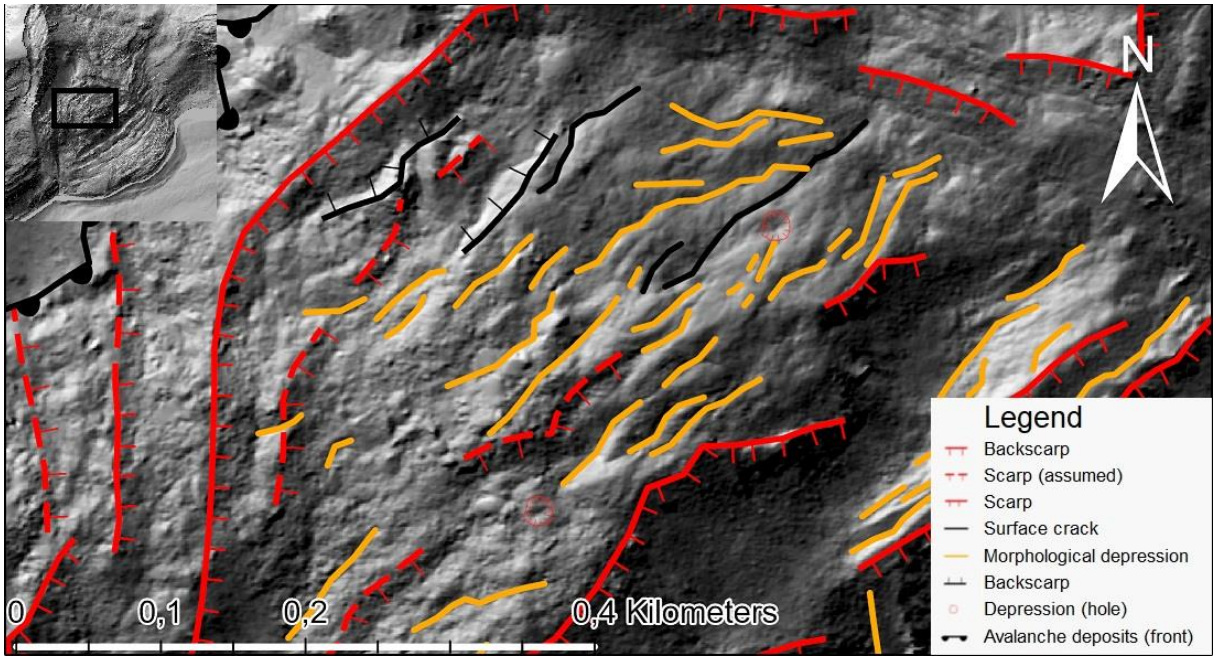

Figure 37: Morpho-structures found at the central domain. At the start there are rounded scarps, followed by counterscarps, morphological depressions, hills and surface fractures oriented perpendicular to the slope movement. Map is on a 1:4500 scale. Hillshade from 1 m DEM (Kartverket, 2021).

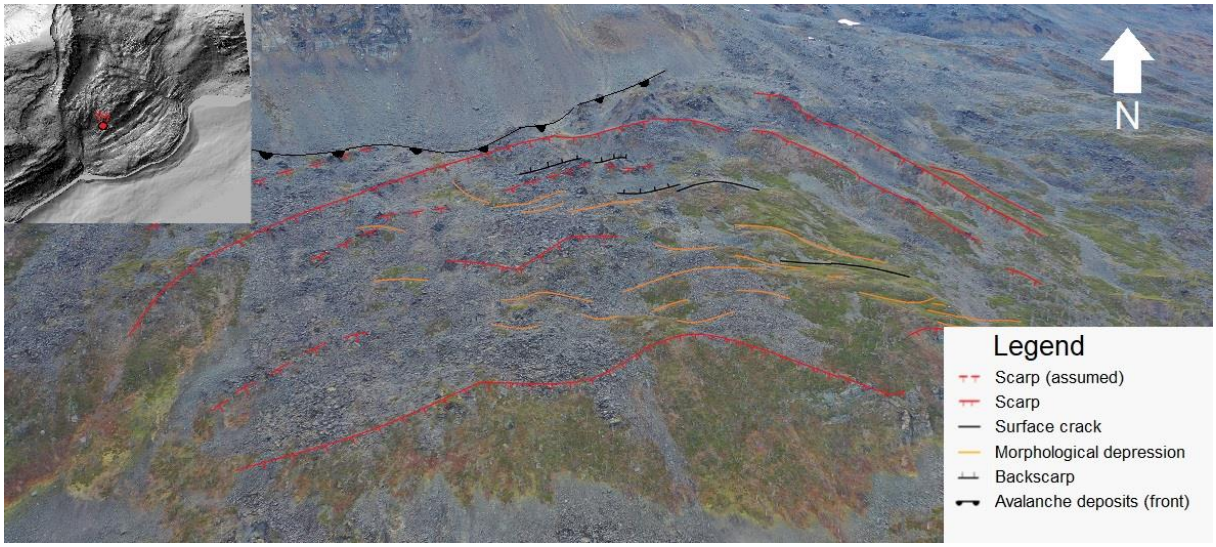

Figure 38: Drone-photo of the central domain. Morphological depressions, rounded scarps, and sudden slope-changes in a disaggregated field of blocks characterizes this area. Location of the photo and direction of view is shown as a red dot on the map in top left corner. Photo: Simen Bekkevoll

The transition zone is located between 300 and 180 m.a.s.l. and covers an area of 480000 m^2. At the start of the Transition zone, there are two steep scarps with terrace-structures at the bottom (fig. 39). Large parts of these steep sections have been covered in rockfall deposits, but several morphological depressions and small ridges can be spotted on these terraces. There can

be found depressions, ridges, gullies, and a variation of slope changes throughout the domain (fig. 40).

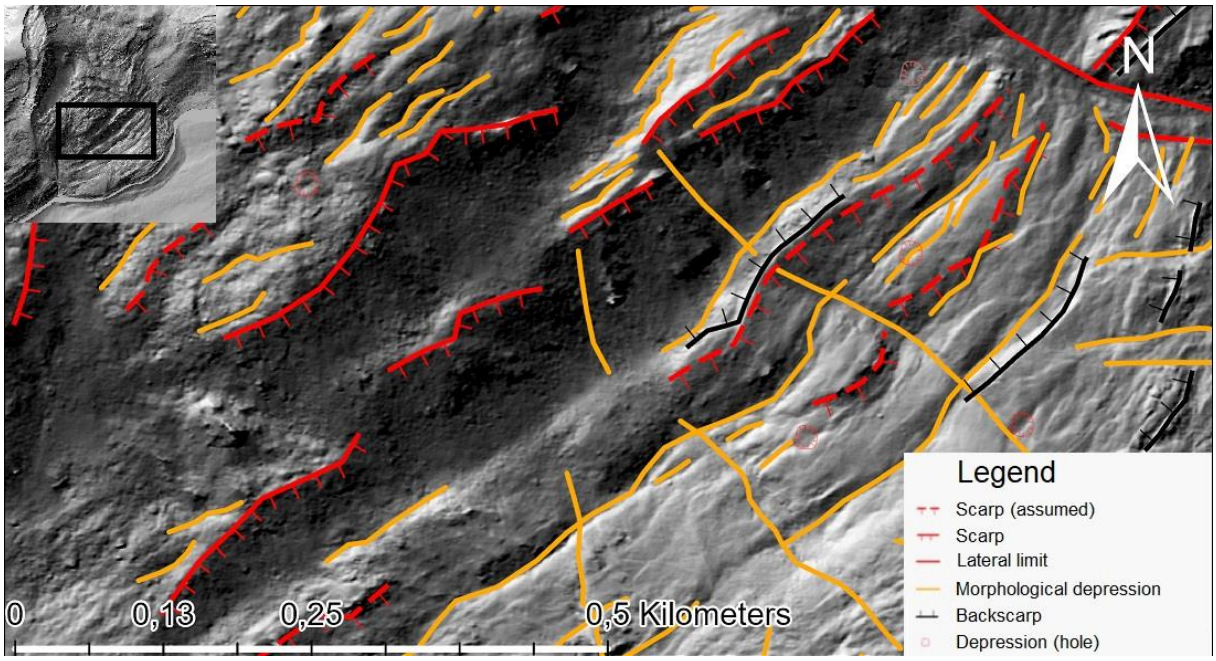

Figure 39: A map of the transition zone, on a 1:6500 scale, with morpho-structural elements found in the domain. Location is shown on map in the top left corner. Hillshade from 1 m DEM (Kartverket, 2021).

Figure 40: Drone photo of the transition zone, showing selected morpho-structures present. Photo: Simen Bekkevoll

The eastern side of the transition zone looks to have more gravitational-driven lineaments of a larger size than the western side of the domain. Lineaments like trenches and ridges (fig. 41)

that goes perpendicular to the direction of the slope movement are more frequent close to the lateral limits. Gullies can be found with certain distances in between and in a sub-parallel direction to the rock slope-movement.

The toe domain represents the last 200 meters of rock slope on land and extends for about 180 horizontal meters beneath sea level. With a width of around 1,5 kilometers, it covers an area of 580000 m^2. As in previous domains, morphological structures are more prominent on the eastern side than on the western side (fig. 41).

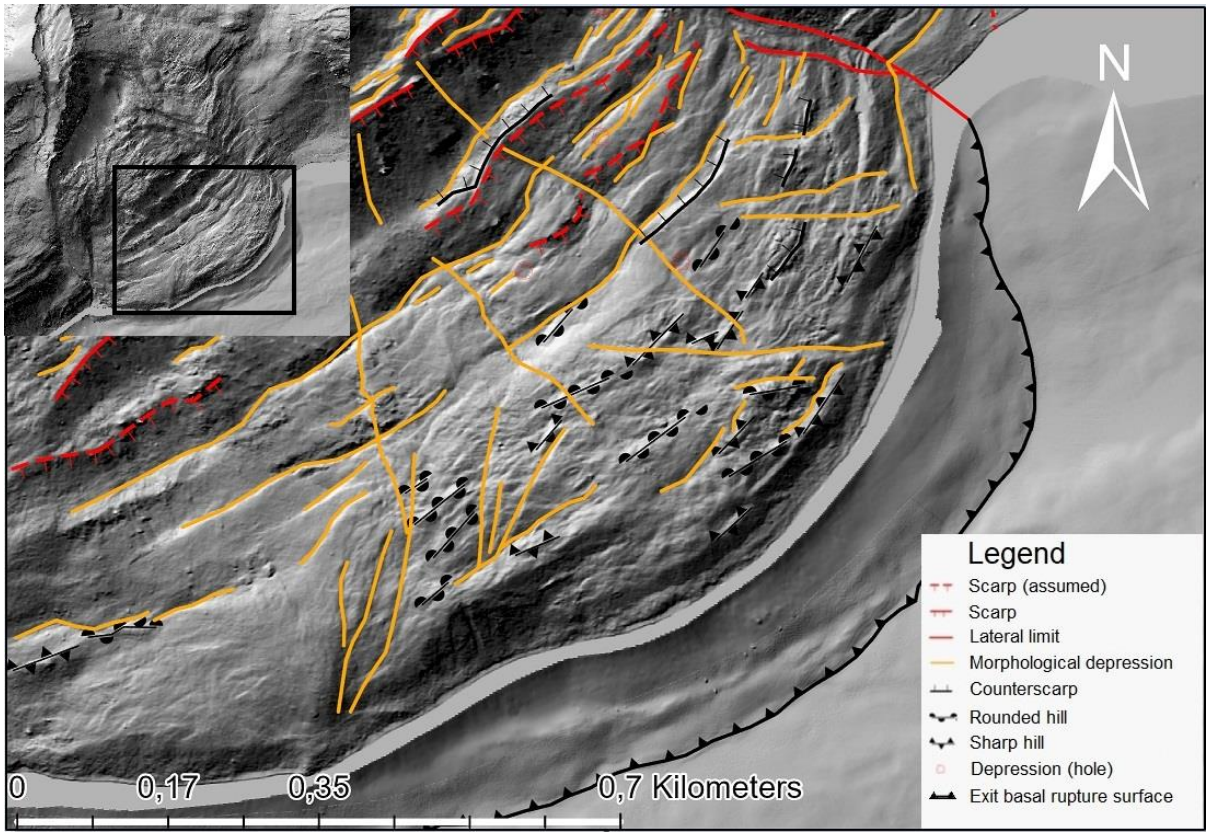

Figure 41: Map with morpho-structures in the toe domain. Map is on a 1:7500 scale. Hillshade from 1 m DEM (Kartverket, 2021).

At the eastern side, morphological structures appear more frequently, and a larger fan-shaped toe is seen beneath sea level. The lateral limit of the deformation continues down from the transition zone and ends in the fjord. There is an outcrop of the lateral limit crossing a woodland-road on the east side of the slope, showing rocks of a higher disintegration-grade than in other parts of the slope. At this outcrop there is also a fine-grained matrix present proximal to the lateral limit, which was absent further in or outside the deformed slope.

Gullies are much more frequent at the toe domain than any other domain. Compared to gullies in the transition zone, gullies at the toe are oriented with a larger offset from the direction of slope movement. Eastern gullies have an offset towards the east, while gullies towards the middle or western parts have an offset to the west. A lot of the toe domain above sea level is made up of hills with sudden morphological depressions in between (fig. 42). Both the hills and depressions are oriented perpendicular to slope movements, but in a "wavier" pattern. There are also found counterscarps at the eastern parts of the toe.

When transitioning to parts of the toe located under sea-level, it is a steep drop down towards the water before a flatter section drags on underneath the water level. There are slope-inclination changes in the underwater section, but not as frequent as above water level. A final toe bulge appears at around 180 meters from the shore, which marks the basal rupture surface exit.

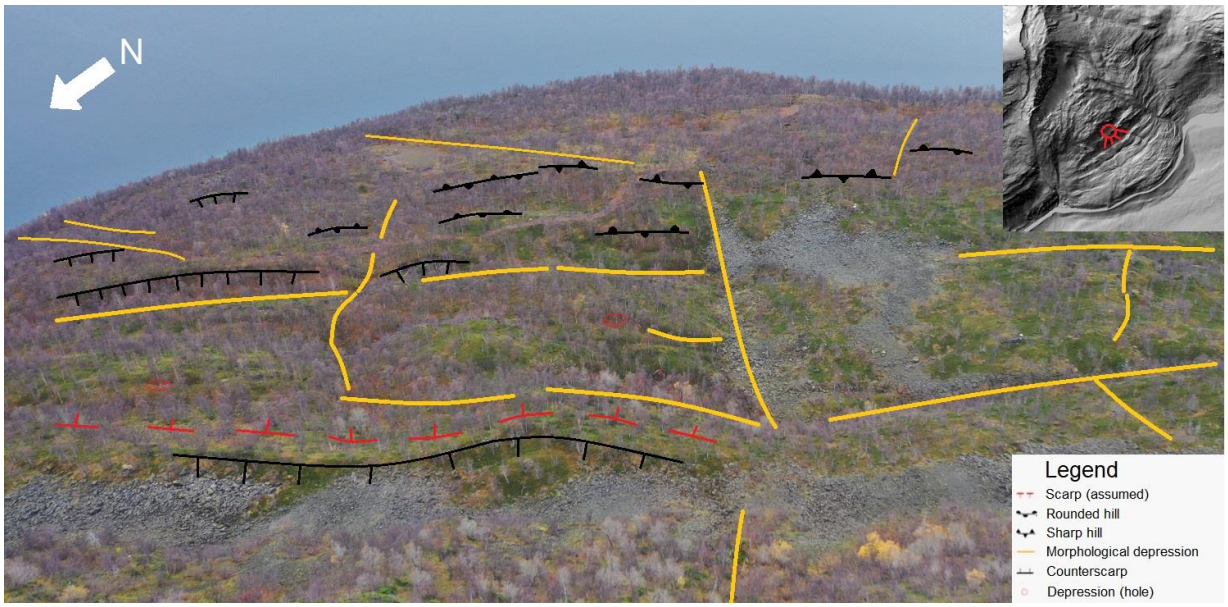

Figure 42: Drone photo of the toe domain with selected morpho-structures present. Photo: Simen Bekkevoll

5.2 Structural analysis

Structures within the rock has been mapped to find what structures are controlling the slope and linking them to the morphology. Since structures and morphology change along the slope, structural measurements are presented from each domain. Structural orientations displayed

from each domain is an average of measurements taken in that domain. A map of measured foliation throughout the slope is displayed in figure 43.

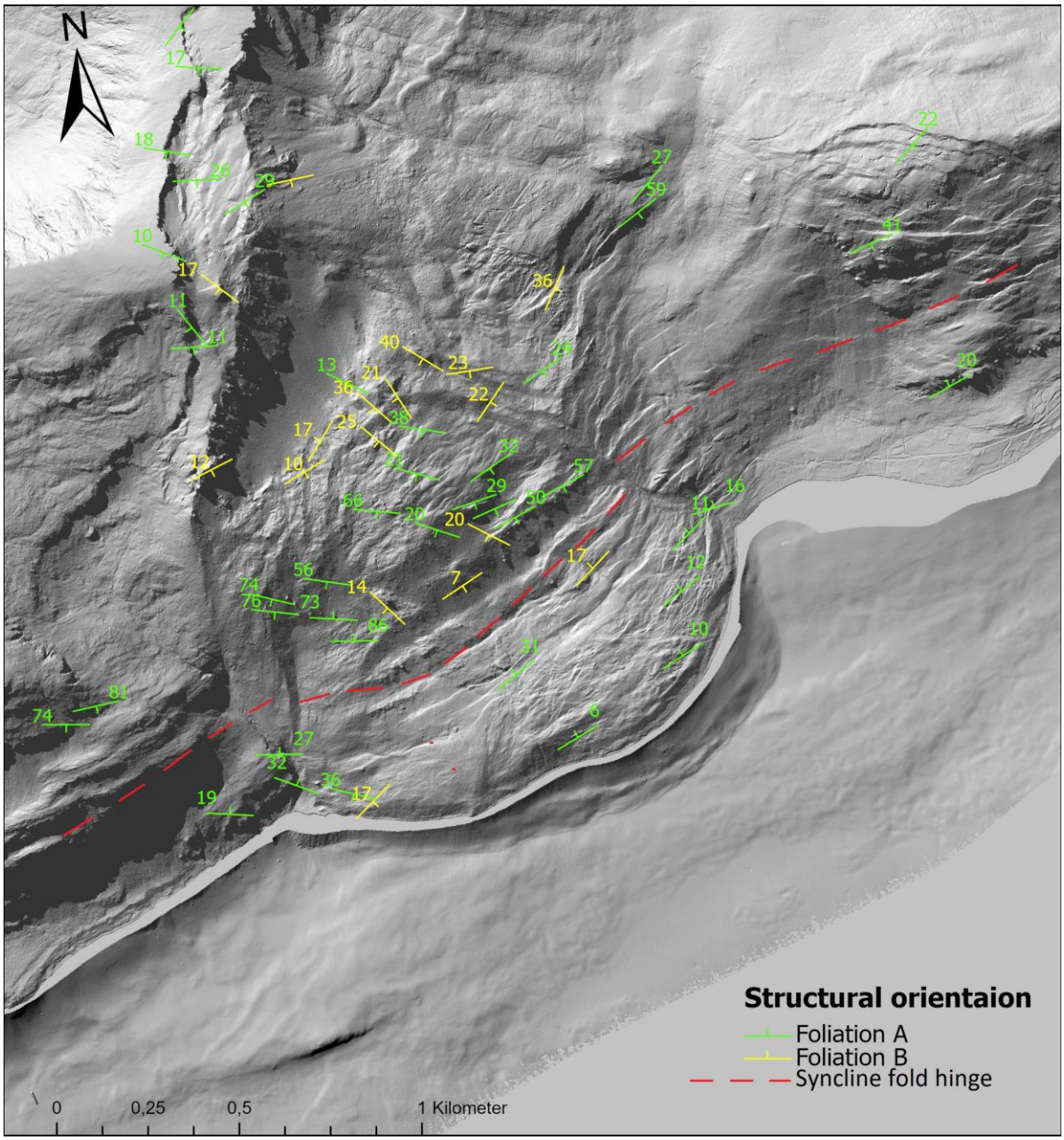

*Figure 43: The two categories **Foliation A** and **Foliation B** are based upon the reliability of the measured foliation. Reliability is in this case based upon the sample size of data and how well the measured data matches with other sites in proximity. If the measurement on a site meets both criteria mentioned above, with high sample rates and a recurring orientation to sites close by, it is put in the green **Foliation A** category. While locations that miss one of these criteria is placed in the less reliable **Foliation B** category. A synclinal fold runs parallel to the fjord, which is verified by measurements from each side of the deformed slope. Hillshade from 1 m DEM (Kartverket, 2021).*

5.2.1 Head domain

At the head of Dusnjárga the two major scarps follow a sub-north/south trending direction and dip sub-vertically at 80° (fig. 44).

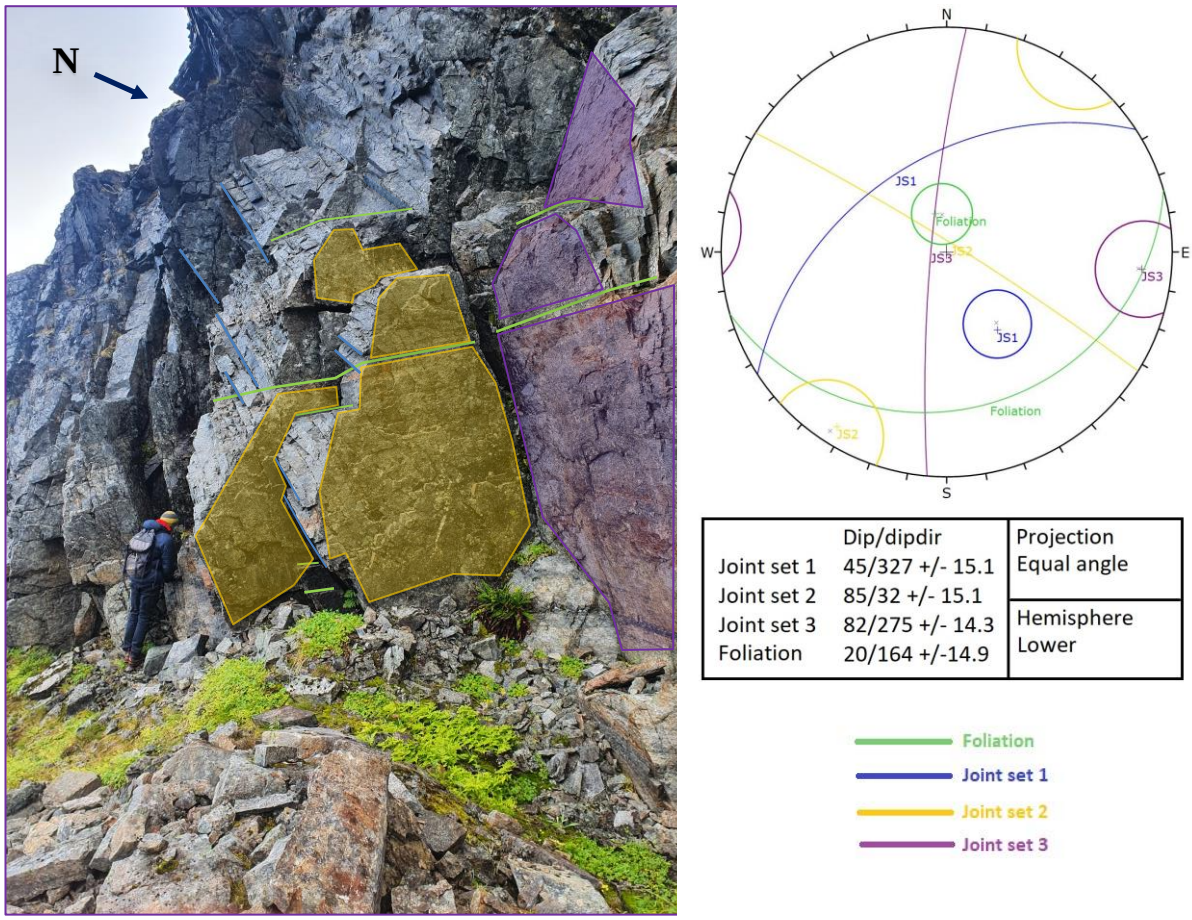

	Dip/dipdir	Projection Equal angle
Joint set 1	45/327 +/- 15.1	
Joint set 2	85/32 +/- 15.1	
Joint set 3	82/275 +/- 14.3	Hemisphere Lower
Foliation	20/164 +/-14.9	

Figure 44: The steep Head Scarp of Dusnjárga. Measured structures are visualised as coloured polygons/lines placed along their respective surface, with an associated table in the bottom right corner. The stereo net-projection shows the average structural orientation and is displayed at the lower hemisphere. Structures are displayed with dip and dip-direction. Photo: Simen Bekkevoll

The fractures in joint set 1, 2 and 3 are more developed than those along the foliation, while set 2 and 3 seems to occur more frequently than the other structures at the backscarp. There is some fracturing along the foliation plane, but it is not too common. The foliation tends to dip slightly more towards SSW in the southern parts of the head.

5.2.2 Central domain

In the central domain, the structures differ in orientation from the western to the eastern parts of the slope. This area is dominated by disintegrated and disaggregated rocks. There are not many places where bedrock-bodies can be found and measured.

In the eastern parts the foliation dips in a south-eastern direction with a dip of around 30°. Joint sets 1 and 2 are easily detectable, with joint set 1 having a sub parallel strike to the foliation. Joint set 1 is dipping at 58° into the slope, towards the northwest. Joint set 2 is sub vertically oriented with a strike that is perpendicular to that of the foliation.

In the midsection of the central domain the foliation is dipping 20° towards SSW. The joint sets have a similar change of orientation as the foliation, compared to the eastern parts. Here both joint sets are sub vertically oriented and stands perpendicular to each other.

The western part of the central domain has a generally much steeper foliation than the other parts. The foliation dips in a southern direction at around 50° inclination on average. The western area is dominated by disintegrated rocks, more so than in the eastern part, and very few rock bodies can be found.

In a small area, at the upper part of the central domain (fig. 45), the orientation of the structures varies a lot. The strike of the foliation can change by 90° and the inclination by 20°.

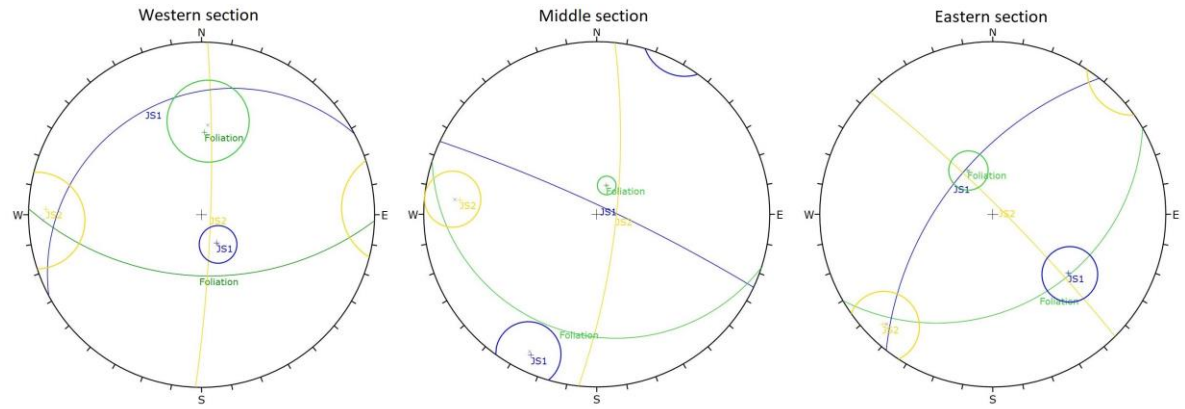

	Dip/dipdir	Projection
Joint set 1	21/232 +/- 12.3	Equal angle
Joint set 2	84/92 +/- 17.1	
Foliation	51/182 +/- 20.6	Hemisphere Lower

	Dip/dipdir	Projection
Joint set 1	84/25 +/- 12.0	Equal angle
Joint set 2	77/96 +/- 10.8	
Foliation	20/198 +/- 6.4	Hemisphere Lower

	Dip/dipdir	Projection
Joint set 1	58/308 +/- 13.8	Equal angle
Joint set 2	84/45 +/- 12.8	
Foliation	33/150 +/- 11.7	Hemisphere Lower

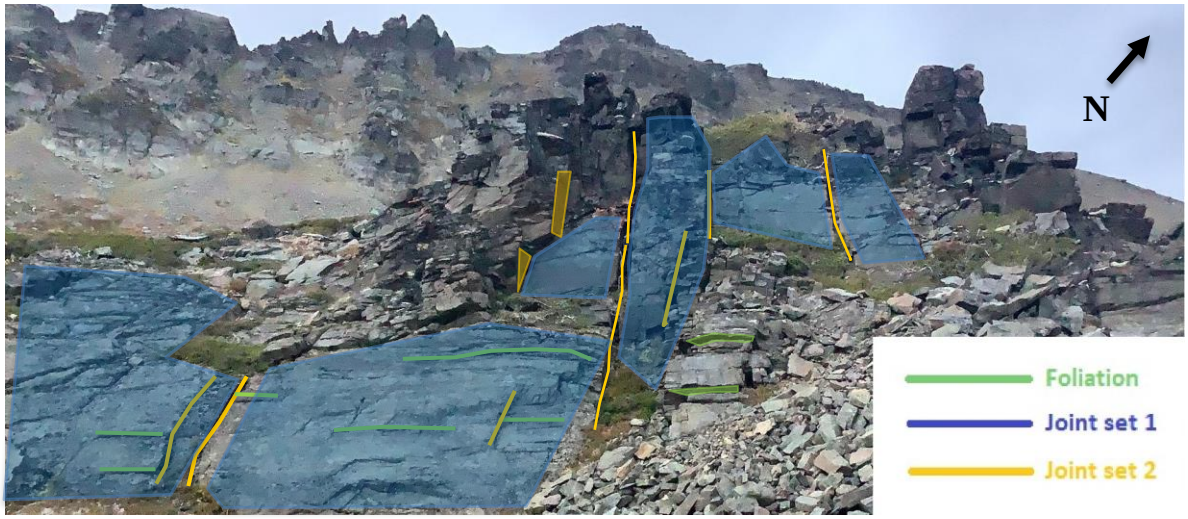

Figure 45: Picture from the upper parts of the Central domain. This spot was abnormal in structural orientations compared to other parts of the same domain but was included for demonstrating how the foliation was oriented relative to the joint sets. The foliation (green) can here bee seen dipping slightly into the slope, which was not the case for the rest of the central domain. Photo: Simen Bekkevoll

5.2.3 Transition zone

At the transition zone, structures differ greatly in orientation from the steep upper section to the flattening lower section and from the western parts to the eastern parts (fig. 46).

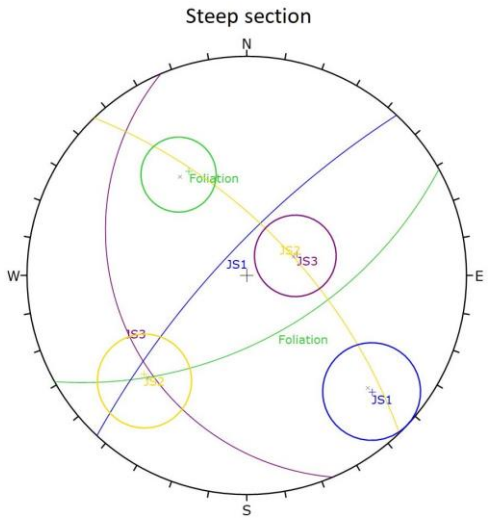

	Dip/dipdir	Projection Equal angle
Joint set 1	76/313 +/-15.7	
Joint set 2	66/46 +/-16.6	
Joint set 3	28/247 +/- 19.6	Hemisphere Lower
Foliation	57/15 +/- 14.9	

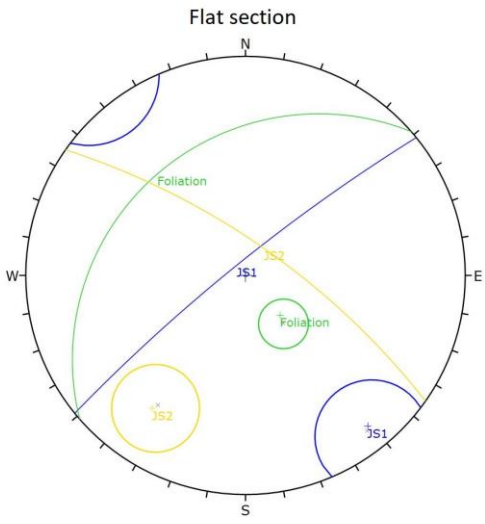

	Dip/dipdir	Projection Equal angle
Joint set 1	83/32 +/- 16.4	
Joint set 2	73/35 +/- 14.8	
Foliation	27/319 +/- 12.4	Hemisphere Lower

Figure 46: Measuring structures at location "scanline 5", located at the steep upper part of the transition zone. Photo: Emile Jensen Aamodt.

In the eastern parts of the steep upper section all three joint sets can be seen together with the foliation. Joint set 3 was well developed compared to other parts of the slope, joint set 1 was similarly developed, while joint set 2 was not. Here the foliation dips in an SSE direction with its inclination increasing downslope, varying from 30° up to 60°.

In the western parts of the upper transition zone the foliation is generally steeper compared to eastern parts with similar altitude, at certain spots sub-vertical. A high amount of disintegrated rocks in the western parts makes it hard to find suitable rock-bodies for measuring structures.

In the flatter parts of the transition zone both the mountain slope and the foliation have a shallower dip than up slope. In fact, the dip direction of the foliation changes by 180° from the steep part to the flat part and starts to dip into the slope. It dips between 15–30° into the slope, in an NNW direction, and becomes slightly more horizontal towards the toe.

5.2.4 Toe domain

The generally weak foliation at the toe in combination with it being a highly vegetated area makes it hard to find measurable structures and especially with visible foliation. From the exposed rock available, the foliation dipped into the slope between 0–10° on average. Joint set 1 and 2 was well developed in the toe, with vertical to sub-vertical dip and almost a perpendicular strike to one another (fig. 47).

The foliation was at its steepest towards the transition zone and it moved gradually to a sub-horizontal orientation closer to the fjord. Far west in the toe, the foliation was steeper than in the middle and eastern parts, which mimics the trend of the other slope-domains. The

dip direction towards southeast seems to be quite uniform throughout the whole toe-domain, except some parts to the west where it changes to an NNE direction. The last part of the toe is underwater and is therefore out of reach for structural measurements.

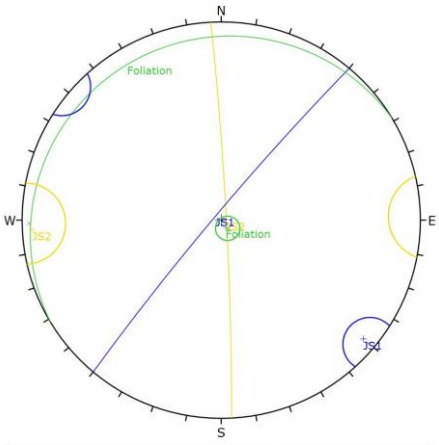

	Dip/dipdir	Projection Equal angle
Joint set 1	86/309 +/- 7.3	
Joint set 2	87/87 +/- 12.2	
Foliation	5/328 +/- 8.1	Hemisphere Lower

Figure 47: Structures at the toe domain. Photo: Simen Bekkevoll

5.2.5 Scanlines

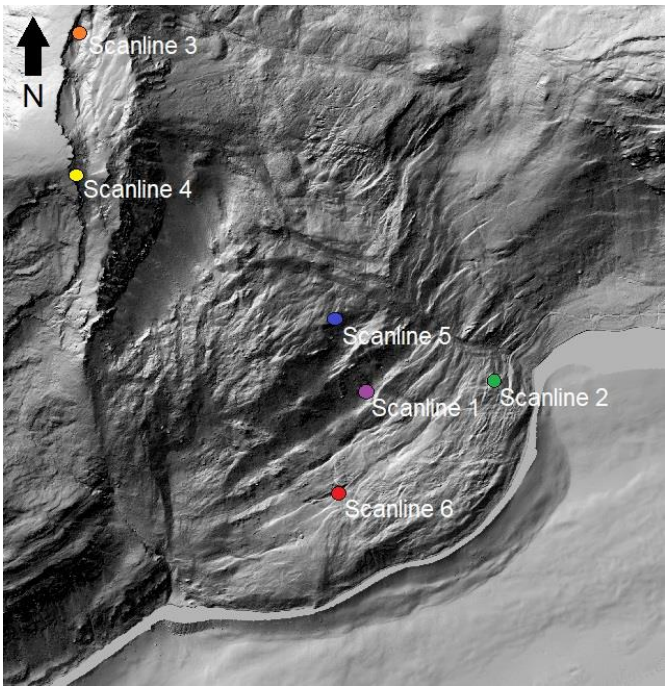

Figure 48: Hillshade-map from 1 m DEM (Kartverket, 2021) with scanline-locations.

Scanlines were taken from evenly spread locations throughout the slope (fig. 48). Most of the locations were uniform in lithology except scanline 3, which had a thin sub-horizontal layer of mylonite. Due to similar lithology, the strength of the rock in each location was found to be unanimously strong. Joints were mostly dry and clean without vegetation or any kind of fill (Appendix 9–14).

Scanline 3 and 4, located in the backscarp of the head domain, had some differences in joint characteristics due to different lithologies. Scanline 3 had 30,6 joint-fractures per 5 m, while scanline 4 only had 13,5 fractures per 5 m. Most joints in scanline 3 had a width of 1 mm, while a few joints were 10 mm wide. Scanline 4 had wider joints between 1–40 mm, and they were longer than in scanline 3.

Located at the steep part of the transition zone, the rock in scanline 5 had the most joints per 5 m out of all the scanlines, with 41,2 joints. The joints were usually 1–2 mm wide and between 20–400 cm long. In the middle of the transition zone, scanline 5 had 26,5 joints per 5 m, and joints with a width of 1–3 mm and a length of 10–40 cm.

Two scanlines in the toe domain were similar in joints per 5 m, with scanline 2 having 23,5 joints and scanline 6 having 21,8 joints. The joint characteristics were somewhat different between the two. Half of the joints at scanline 6 were at 10–50 mm, while the second half were between 0–5 mm wide. Scanline 5 had most of its joints over 100 cm in length. Scanline 2 had tight joints of 1–2 mm and a length of 10–70 cm.

5.3 dGNSS

Displacement rates measured by dGNSS from different parts of the slope. NGU had 8 points of measurements displaying annual movement, while NVE had 2 points of measurements, displaying time series over 1 year. Figure 51 displays all dGNSS locations with valid and invalid measurements, based on the uncertainty (chapter 4.1.4)

DUSN_GPS_01

This dGNSS point, located on the edge of the large frontal scarp of the head block, shows movement both in the horizontal and vertical axis. Displacement on this location was measured over a period of seven years, from 2007–2014. From appendix 2, one can see that the direction of movement is towards southeast at around 124 degrees north, with a dip of around 29 degrees down-slope and with an average annual displacement rate in 3D of 7 mm/y (fig. 51).

DUSN_GPS_02 and DUSN_GPS_03

At dGNSS point 2 and 3, located at the top block of Dusnjárga, displacement rates are too low for interpretation. One can see a trend in the vertical axis (Appendix 3), but none of the annual measured displacements rates made it past the uncertainty, neither in the vertical or horizontal axis.

DUSN_GPS_04

This location shows some noticeable displacement in both the vertical and horizontal axis, with both exceeding the uncertainty. Measurements are done over one year, from late summer of 2020 to late summer of 2021. Data show that displacement at this location is oriented southeast at 137 degrees north and with a 59 degrees dip (Appendix 4). 3D vector shows a displacement rate of 19 mm/y (fig. 51).

DUSN_GPS_05

Measurements are exceeding the uncertainty in both the vertical and horizontal plane at this dGNSS point. Measurements are done over one year, from late summer of 2020 to late summer

of 2021. Orientation of displacement is towards 154 degrees north and with a 41 degrees dip (Appendix 5). Average annual displacement rate in 3D is by 14 mm/y (fig. 51).

DUSN_GPS_06

A site with little movement, so little that in the one year of dGNSS measurements, only data from the N-S horizontal direction can be validated as actual movement, the other measured directions do not exceed the uncertainty (Appendix 6).

DUSN_GPS_07

There is one horizontal direction (N-S) where displacement was larger than the uncertainty at this site (Appendix 7). In the vertical plane there are small indications of a rising trend, but as with the horizontal E-W plane the uncertainty is larger than the measured displacements, making measured data in those directions inadequate for accurate projection.

DUSN_GPS_08

At the location for dGNSS point "DUSN_GPS_08" there is an indication of an upwards trend in the vertical axis. But due to only one year with measurements, the displacement is too small in relation to the uncertainty, to make claims on vertical movement based on these results alone. Displacement in the horizontal axis exceeds the uncertainty in both N-S and E-W direction (Appendix 8). Orientation of displacement is towards 125 degrees north and with an average annual 3D displacement rate of 12.5 mm/y (fig. 51).

DUSN_NVE_1

This dGNSS antenna from NVE is placed in the central domain of unstable rock slope. It shows horizontal movement and some indication of a vertical downwards movement. Interestingly the one-year time series show a distinct increase in displacement over a two-month period from the middle of June (fig. 49). Which suggests active and inactive periods, as opposed to a constant movement through the whole year. Combined horizontal vectors are pointing to 120° north at a velocity of 14mm/y (fig. 51).

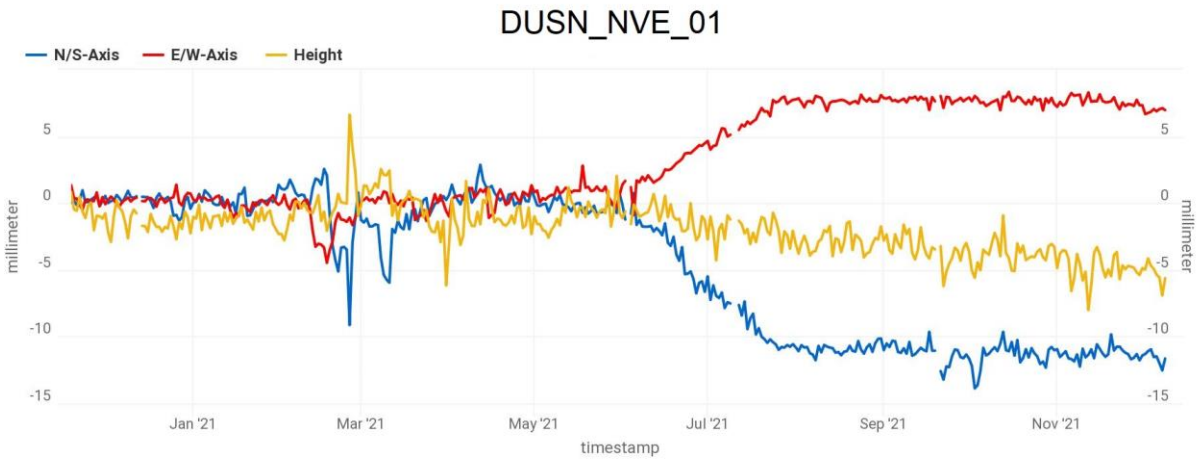

Figure 49: Time series spanning over one year, from the start to the end of 2021. X-axis displays time, while y-axis displays displacement (mm). Provided by NGU.

DUSN_NVE_2

This dGNSS point is in the middle of the toe domain. It does not show the same rate of movement (fig. 50) that were displayed at the higher elevated locations. The vertical displacement data is varying rapidly, which as described chapter 4.1.4, can be due to a combination of atmospheric variations and the result of little movements over a single year of measurements. The combined horizontal data measures in at 8mm/y.

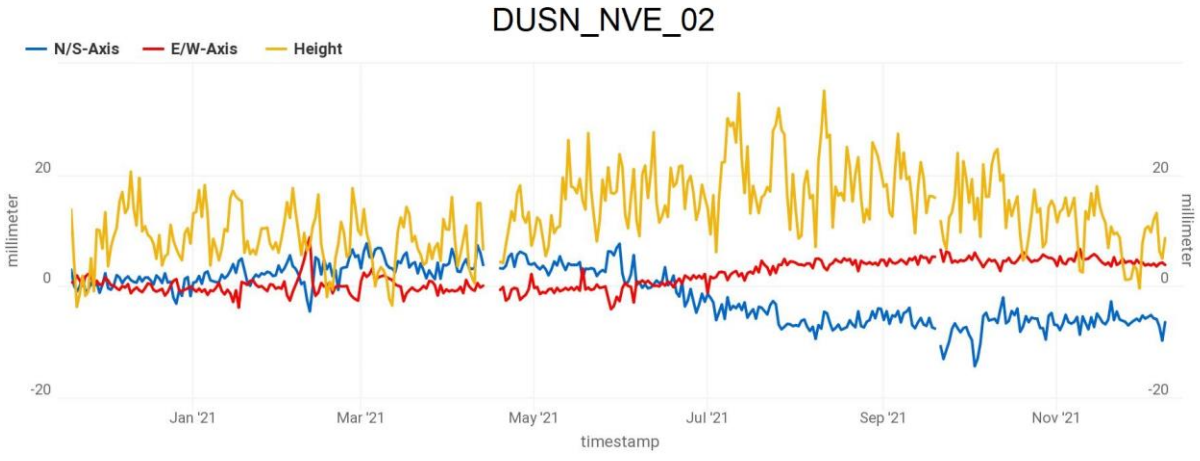

*Figure 50: Time series of location **DUSN_NVE_02.** Some chaotic vertical measurements while a clear trend is shown for the horizontal displacement. Time displayed on x-axis and displacement (mm) on y-axis. Provided by NGU.*

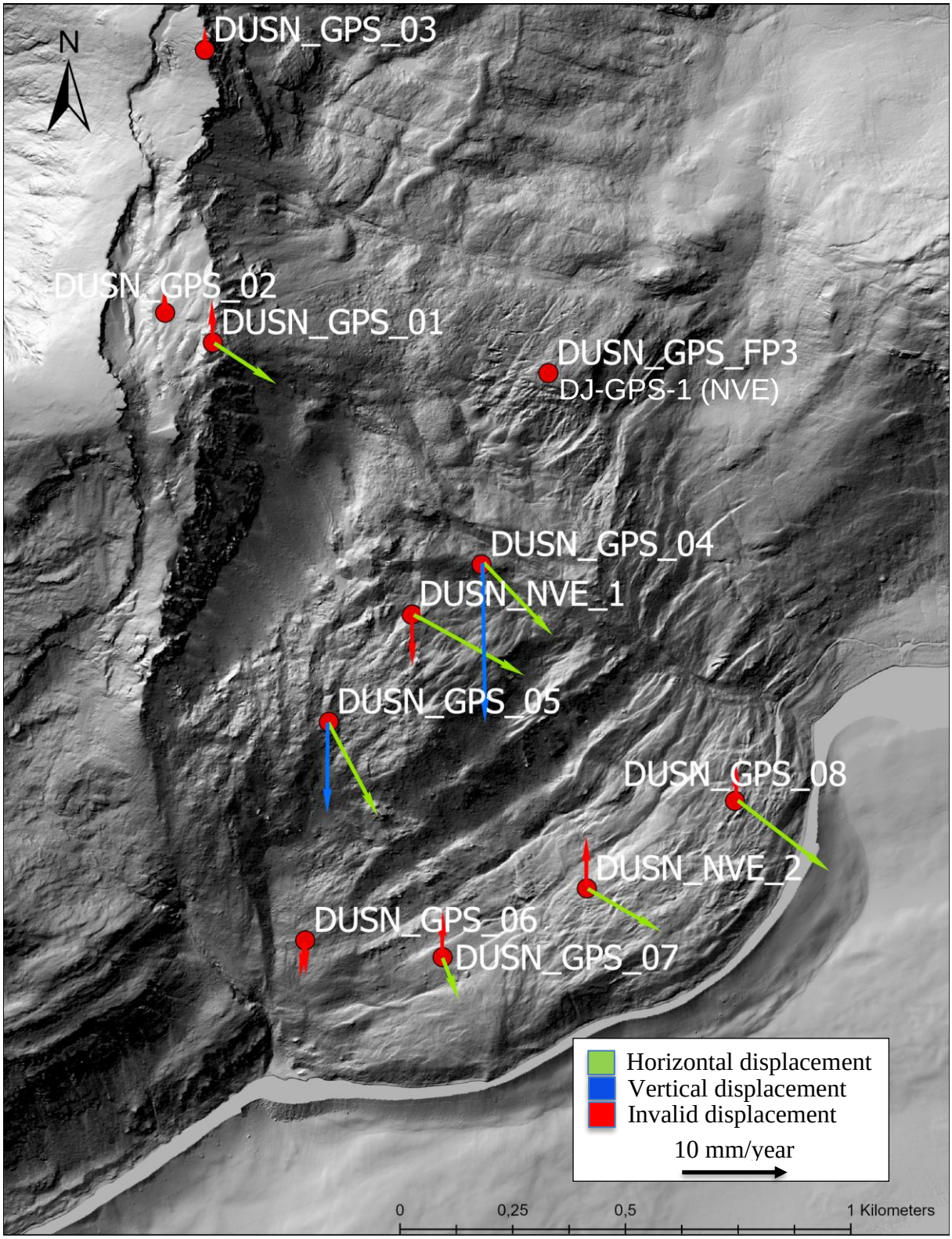

Figure 51: dGNSS points with vector-displacement on a hillshade map. Displaying each dGNSS point as red dots with green vectors as horizontal movement, blue vectors as vertical movement and red vectors as invalid measurements due to lower displacement than the uncertainty. Hillshade from 1 m DEM (Kartverket, 2021).

5.4 2D InSAR

2D vectors from InSAR have been displayed along terrain profiles (fig. 52). The cross sections have been drawn parallel to the interpreted displacement for each profile.

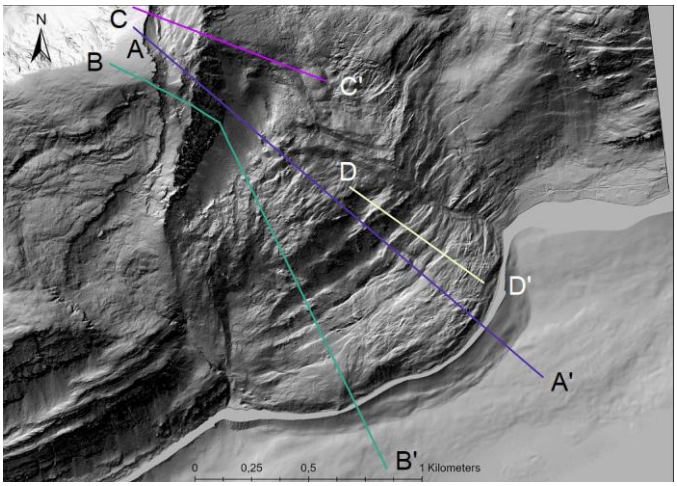

Figure 52: Profiles plotted on a hillshade map from 1 m DEM (Kartverket, 2021).

Four different profiles have been chosen. Two covering the length of slope from top to bottom (A – A' and B – B'), one crossing the unstable area in the northern head domain (C – C') and the last one extending over the transition zone (D – D').

Variations in displacement data between each InSAR dataset were tested for certain areas, where average estimates within polygons were compared for both the ascending and descending geometries. Comparisons showed little to no difference in mean velocity values, where all 3 ascending and all 3 descending datasets had less than 1 mm/year in difference from the others. This was also tested in multiple 2D InSAR profiles, comparing different datasets, ending up with the same result.

Ascending 1 combined with descending 1 were used for profile C – C', as they covered the head domain and the slope below better than the other datasets, while also intersecting with the GB-radar dataset. Ascending 2 and descending 2 had the best spatial coverage along profile D – D', while ascending 3 and descending 3 were used for profile A – A' and B – B'.

Inputs used when creating 2D InSAR profiles are displayed in table 4. Minimum point spacing (distance between displayed points) of 10 were set for the visual presentation of the profiles, while minimum point spacing was set to 1 for the graphs, showing vertical, horizontal, and total displacement (displayed in figs. 53, 54, 55, 56). This was done to get as many displacement-points as possible for the interpretation-graph, while having a visually pleasing figure with less

points for referencing. A reference vector length of 10 mm/year is used for the interpreted cross sections in chapter 5.7.

Table 4: Inputs used in GIS-tool for the 2D InSAR method.

Profile	A - A'	B - B'	C - C'	D - D'
Maximum projection distance	20	20	20	20
Calibration	Selected area	Selected area	Selected area	Selected area
Alignment, sample intersection radius	20	20	20	10
Interpolator	Weighted neighbourhood	Weighted neighbourhood	Weighted neighbourhood	Weighted neighbourhood
Neighbourhood radius	50	50	50	50
Neighbourhood weight	Uniform	Uniform	Uniform	Uniform
Regularisation (bearing)	Constant zero (38)	Constant zero (65)	Constant zero (20)	Constant zero (25)
Reference vector length	5 mm/y	5 mm/y	5 mm/y	5 mm/y
Style minimum point spacing	10	10	10	10
Vector scale factor	1	1	1	1

Along profile A – A' (fig. 53) there are large gravitational-driven lineaments which run perpendicular to the profile. The head domain shows little to no movement. In the upper part of the central domain one can see that the dip of displacement is at a high angle, facing down-slope. The dip of displacement decreases down-slope to about 400 m.a.s.l., before it has a slight increase towards the start of the Transition zone. From around 400 m.a.s.l. to around 120 m.a.s.l. the mean velocity is decreasing. The lack of CSDs in the toe domain makes it difficult to view SAR-based displacement data in this area. But a small sample of CSDs towards the outer parts of the toe shows that there is an increase in velocity somewhere between the transition zone and the toe. It seems that displacement rates decrease down to the same point where displacement vectors start to dip above the horizontal plane.

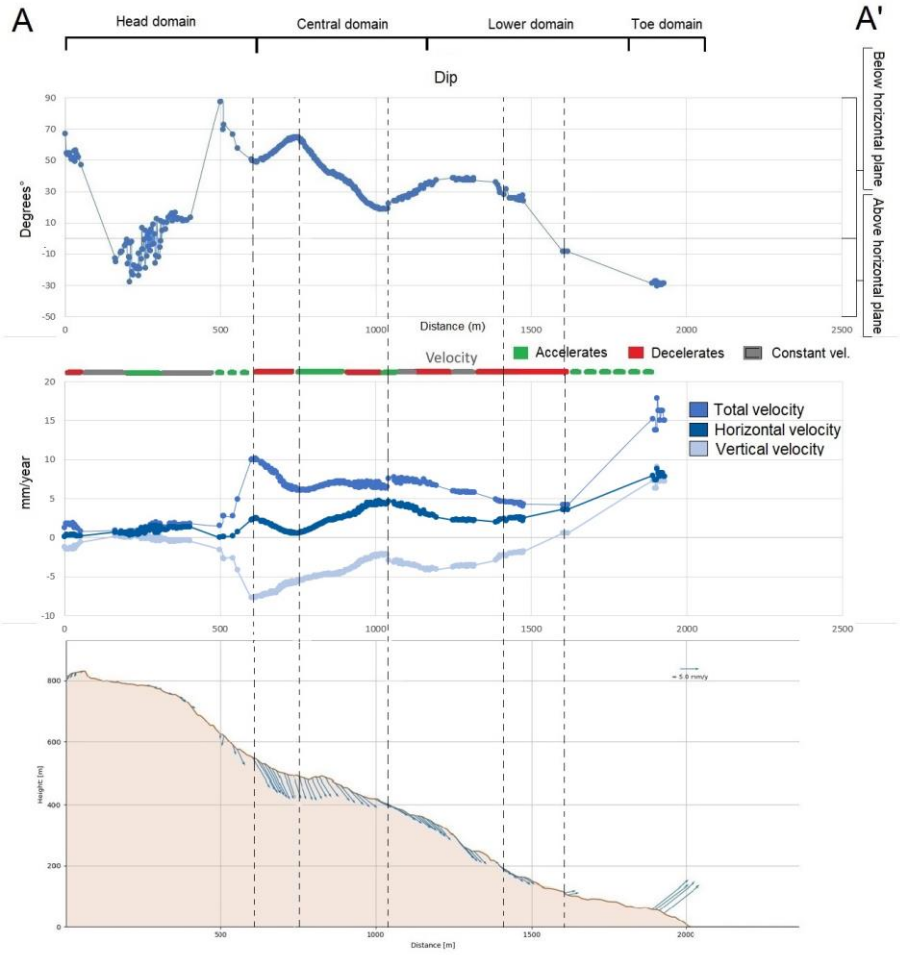

*Figure 53: 2D InSAR displacement profile **A – A'**. From the top is dip of movement, velocity, and a cross-section with displacement vectors, showcasing movements from certain CSDs along the profile. A line showing change in acceleration, deceleration and constant movement down the slope can be found in the velocity-section. Black lines are drawn on sudden changes of either velocity or dip of movement.*

Profile B – B’ (fig. 54) runs perpendicular through several morphological structures on the western side. There is little to no movement in the head domain. A sudden peak in displacement rate happens at around 520 m.a.s.l. before it decreases down-slope to 400 m.a.s.l. Then a 200 meter stretch of the slope shows an increase in displacement rate, before it again decreases down to the same altitude as profile A – A’ at 120 m.a.s.l. The dip of movement along profile B – B’ show less variation than along profile A – A’, at least in the most active parts of the slope. As in profile A – A’, a line can be drawn through a point in the flat parts of the transition zone where velocity starts to increase while displacement vectors start to dip above the horizontal plane, at around 120 m.a.s.l.

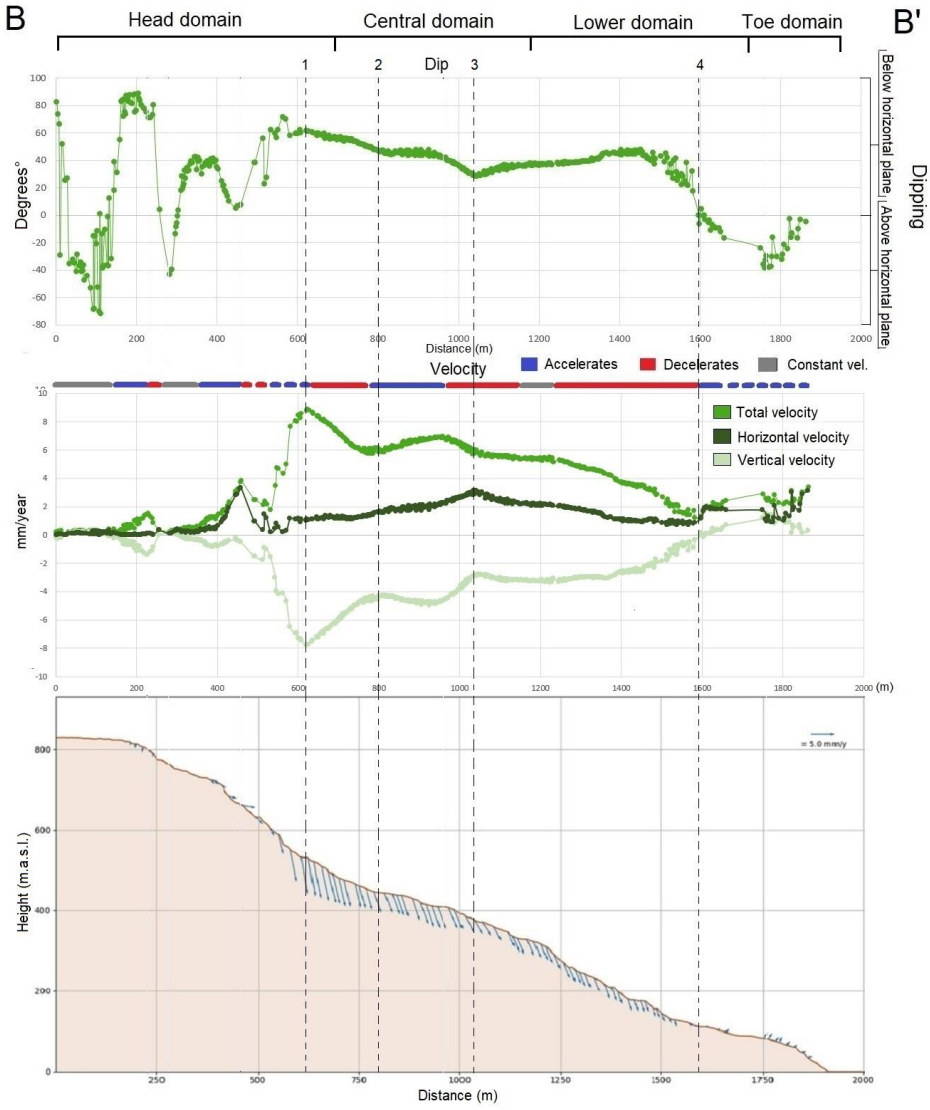

*Figure 54: 2D InSAR profile **B – B'** with associated dip of movement, changes in displacement rates down-slope, horizontal, vertical and total displacement velocities and vector-displacement down-slope.*

Profile C – C' (fig. 55) covers an area of the head domain that shows signs of movement on both dGNSS measurements and by InSAR. There is little to no movement along the major backscarp to the northwest, while towards the lower major scarp, a sudden spike in velocity is shown. The increase in velocity starts at about 790 m.a.s.l. and gradually decreases down-slope. Between 780–730 m.a.s.l. there is no InSAR coverage, so kinematic data is lacking.

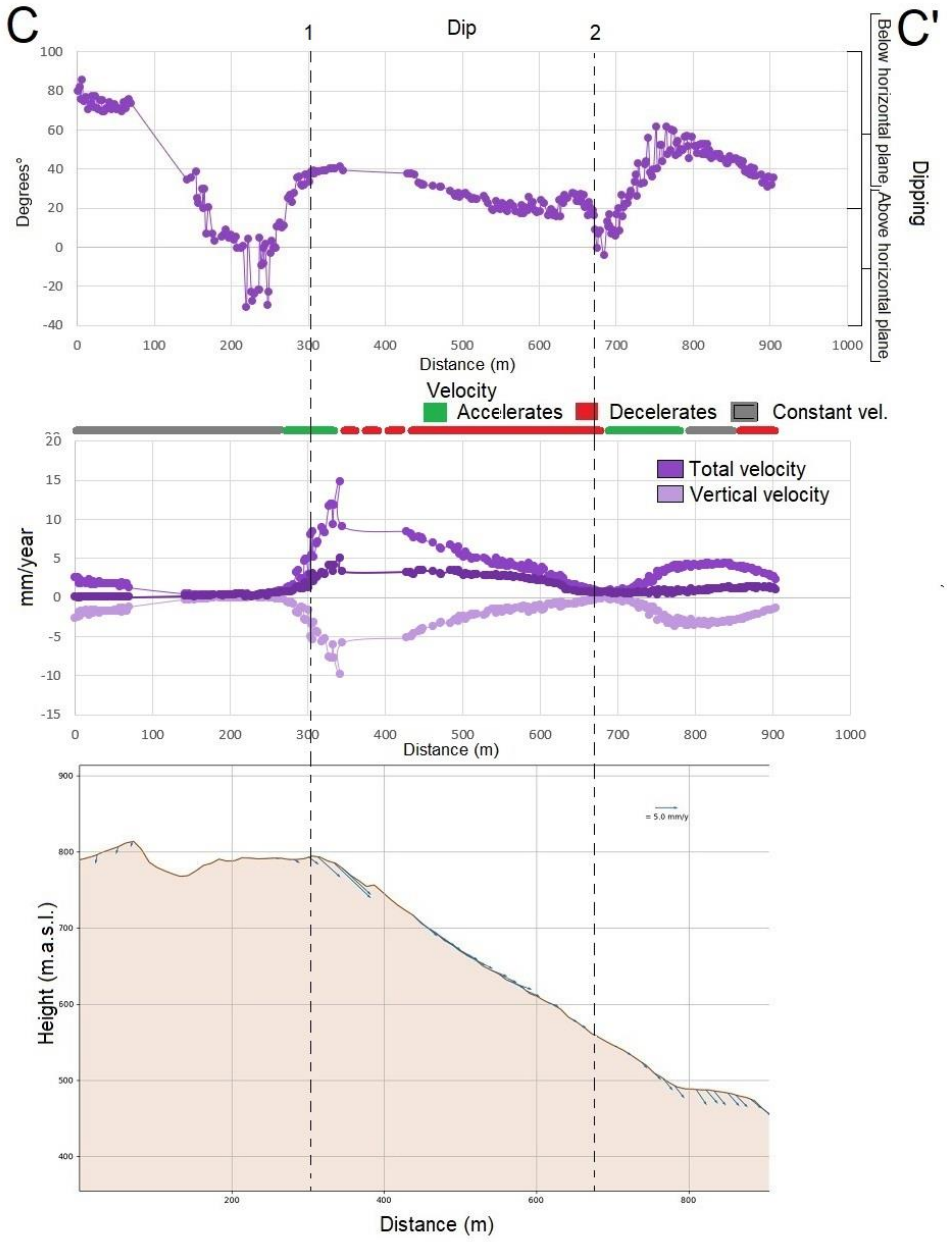

Figure 55: ***C – C':*** *2D InSAR data covering an unstable part of the head domain, displaying dip of slope movement, total velocity and velocity vectors along the slope.*

Profile D – D' (fig. 56) covers the transition zone, a zone where the slope has its biggest change in inclination and where most of the largest gravitational-driven lineaments occur. The dip of movement is at its highest at a terrace 250 m.a.s.l., in the steep section of the transition zone. The dip of movement is then gradually shallower downslope, while the movement starts to dip above the horizontal plane at around 130 m.a.s.l., approximately at the same elevation as in

profile A – A’ and profile B – B’. The displacement rates generally decrease down-slope until the point of change in dip at 130 m.a.s.l., in which it has a slight increase from then on.

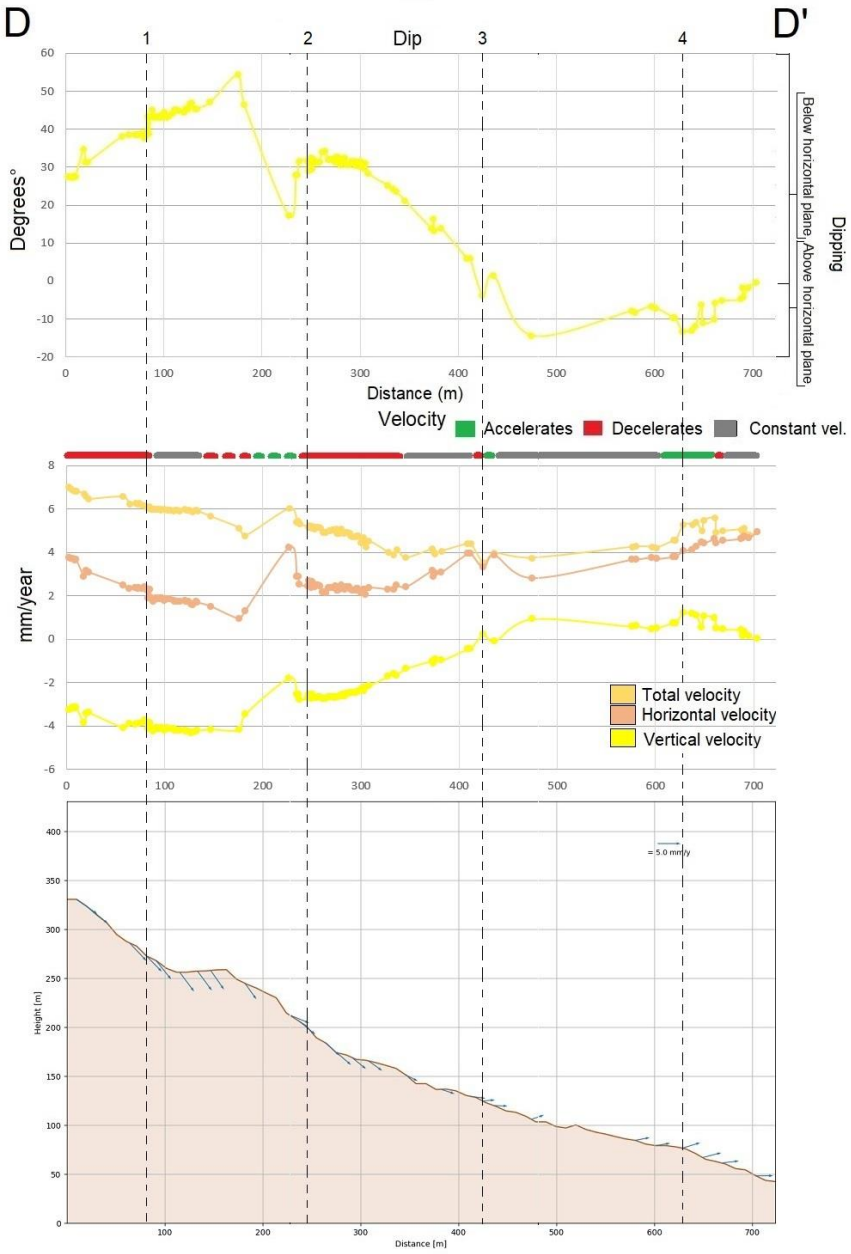

Figure 56: ***D – D’:*** *2D InSAR profile of the transition zone, located in the transition zone. Figures are displaying dip of movement, changes in acceleration, horizontal, vertical and total velocities and velocity vectors along the slope.*

5.5 3D InSAR

The 3D InSAR shows local variations in both dip of movement, velocity, and direction of movement in the upper parts of the slope. Dip of movement is steeper along the outer limits of the active slope (fig. 57). The change in dip follows the sub-circular scarp-structures in the central domain. Dip changes from around 35–50° in the uppermost parts of the central domain down to around 20–25° in the central parts. Based on 3D InSAR, the velocity at the central domain is on average between 10–14 mm/year, while the velocity decrease towards the lateral limits of the slide. Movement vectors point in the expected direction, towards the southeast.

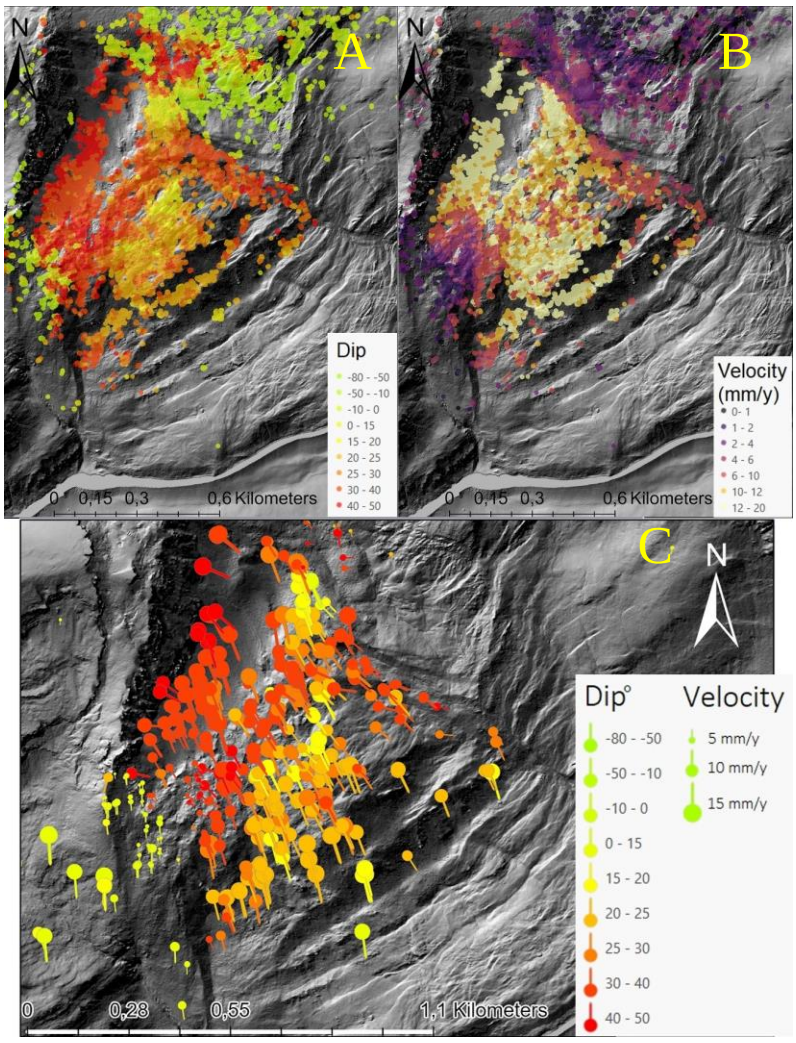

Figure 57: Velocity and dip is separated in A and B for a better view of each measurement. C: A 3D projection of displacement in the slope. The symbols point in the direction of movement, while vertical dip is displayed with changing colours and velocity is based on the size of the symbols. Negative dip represents an upwards movement, while positive dip represents a downwards movement. Background hillshade from 1 m DEM (Kartverket, 2021).

5.6 Paleo shoreline

As described in chapter 2.2, two different shorelines have previously been mapped along Lille Altafjord, where Dusnjárga resides. The lowest elevated shoreline mapped by Frederic Blau (Blau, 2020), was mapped at an elevation of 23–25 m.a.s.l., going beneath the rock slope Låvan and ending 200 meters from the eastern lateral limit of Dusnjárga. However, it seems that this shoreline can be traced further west, crossing the eastern lateral limit of Dusnjárga and traced for another 100 meters inside the deformed slope (fig. 58).

The shoreline follows an elevation of 24 m.a.s.l. east of Dusnjárga, until it crosses a lateral lineation with signs of displacement, interpreted from morpho-structures (Appendix 15). West of the lateral displaced limit, herby referred to as an inactive lateral limit, the shoreline is lowered to an elevation of 22–23 m.a.s.l., showing some downwards displacement inside the inactive lateral limit. As the shoreline crosses the active eastern lateral limit of Dusnjárga, its elevation gradually declines. The shoreline can be traced to an elevation of 16 m.a.s.l., before it is unrecognizable due to increased displacements towards the middle of the toe.

West of Dusnjárga the shoreline is again discovered as it runs with minimal vertical change, at an average elevation of 23 m.a.s.l. Traces of the shoreline cannot be seen crossing the western lateral limit, maybe due to the terrain there being very steep, and with less sediments than east of the slope.

As mentioned in chapter 2.2, the isobase-map (fig. 20) show that along the same isobase-line as Dusnjárga is Ullsfjorden in Lyngen, where paleo shorelines elevated at 21–22 m.a.s.l. were dated to the Tapes transgression (Corner and Haugane, 1993), which translates to being 7600–5600 cal BP (Bondevik et al., 2019). It can therefore be suggested that the paleo shoreline crosscutting the eastern lateral limit of Dusnjárga is of the same age as the shorelines in Ullsfjorden. The shoreline shows distinct changes in elevation at both the inactive and active lateral limit, while also being increasingly deformed towards the middle of the deformed slope before it gradually disappears. This suggests that Dusnjárga would be actively deforming in the years after the Tapes transgression, both for the present inactive parts and the active parts of the slope. However, the initial start of the deformation is unknown.

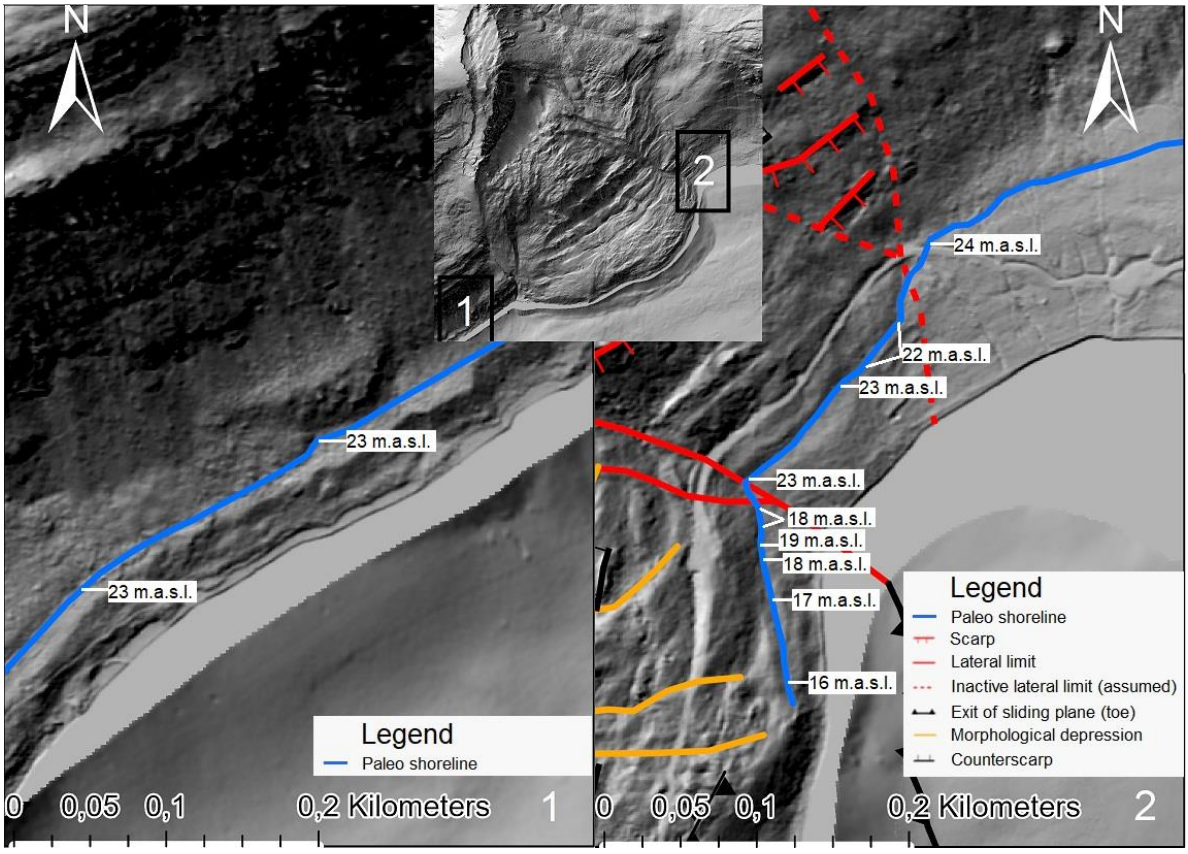

Figure 58: The paleo shoreline crosscuts the lateral limit on the eastern side of Dusnjárga. The elevation of the shoreline changes from east to west, as it gets gradually more displaced by the deformed slope. The shoreline can also be found on the western side of Dusnjárga, where it has a more consistent elevation. Hillshade from 1 m DEM (Kartverket, 2021).

5.7 Interpretation of rock slope kinematics

Results from the structural-, morphological- and displacement analysis are used for this interpretation. By combining displacement measurements, done by dGNSS and InSAR, with mapped morphological features, as well as identifying which structures are controlling each part of the slope, a kinematic interpretation is possible. The general trend of foliation is drawn as thin green lines in the cross-sections. However, the dip of foliation at the head domain is locally oriented 90° to the profiles, making the drawn foliation at the head domain flawed. In order to not abruptly end the drawn foliation in the cross sections, and to display the foliation as an interpreted step-fracture at the head domain, the foliation has been drawn sub-horizontally at the head domain in profile A – A' and B – B'. Structures drawn on the profiles has been adapted from their true dip to their apparent dip and controlling structures has been interpreted for the morphological elements present.

Profile A – A'

The backscarp (fig. 59-1) is steep and mainly controlled by joint sets 2 and 3. A large trench divides the backscarp from a series of counterscarps. The counterscarps are dipping into the slope, controlled by joint set 1. The head domain shows little to no displacement along profile A – A'.

Noticeable displacement first occurs at the start of the central domain (fig. 59-2), at the foot of the steep cliff from the frontal major-scarp. The first displacement vectors dip at 50° from horizontal**,** becoming steeper and with less velocity down-slope. A comparison can be done with fig. 26 h/i, where sudden variations in vertical dip and velocity can translate to movement of disconnected blocks. After the initial movement comes a section where displacement-dip is becomes, while the horizontal displacement gradually increases, and the vertical displacement gradually decreases. Displacement becomes gradually more horizontally dominated, until it stabilizes at around 20–25° (fig. 59-3), which matches the dip of foliation in the area. This gradual change (Fig. 26 c**)** in vertical and horizontal velocities is likely due to the rock slope transitioning from a large block moving along the rear-rupture surface, to a more coherent central domain that moves along the basal rupture.

Large scarp-like structures run across the slope in the upper parts of the central domain (fig. 59-2), matching the sudden change in 2D InSAR velocity. The rear rupture-surfaces in the central domain are controlled by both the foliation and joint set 1. These scarp-like structures in the central domain links up with the large lateral limits, running down each side of the slope. Transitioning from the scarps to the lateral limits, the structural control of joint set 1 gets replaced by perpendicularly oriented joint sets 2 and 3, which have a strike running parallel to the orientation of the lateral limits.

At parts of the central domain where 2D InSAR velocity seem to follow the foliation, a series of trenches, surface fractures and sudden slope changes running perpendicular to the slope movement occur at the surface (fig. 59-3). These morpho-structures are controlled by joint set 1 that dips steeply into the slope. Further down-slope, at the start of the transition zone, the slope-surface and the 2D superficial displacement data is steeper, follow the trend of foliation-dip. At the steep section of the transition zone, large extensional morphological lineaments in

the form of trenches, scarps and terraces mainly follow the structural orientation of foliation and joint set 1. The dip of scarps of the displaced blocks in the steep transition zone is believed to gradually decrease with depth, as described by e.g. (Vick et al., 2020), eventually becoming sub-parallel to the foliation.

From the top of the steep slopes in the transition zone to the point of zero vertical movement (fig. 59-4), hereby called “point of transition”, there is a steady decrease of the total velocity. A combination of joint set 1 and the foliation (likely by step-fracturing) are controlling the morphologic features present, with the dominant structure shifting between the two. From the point of transition, the vertical displacement starts to dip above the horizontal plane, following the foliation orientation, while the total velocity steadies before having a slight increase towards the toe. The point of transition does not mark an instant change from extension to compression, but rather a gradual change up until this point. There is likely a zone of high strain internal shearing at the point of transition, because of the change in direction of movement (Stead et al., 2011). A series of scarps and trenches, perpendicular to the direction of movement, can be found in this area, interpreted to be affected by a combination of extensional and compressional forces.

There are several sudden slope changes, morphological depressions, and small hills with less linear orientations than morphological structures further up the slope, probably due to compression in the toe domain (fig. 59-5). While the compressional morpho-structures are not as prominent as some of the larger extensional morpho-structures found in other parts of the slope, they occur more frequently. InSAR data and dGNSS measurements show displacement along the sub-horizontal foliation, while local features like counterscarps and steep trenches suggest that joint set 1 also has affected the morphology at the toe. The interpreted basal rupture surface daylights below sea-level, as can be seen on the geomorphological map (fig. 33), creating a trench in front of the toe.

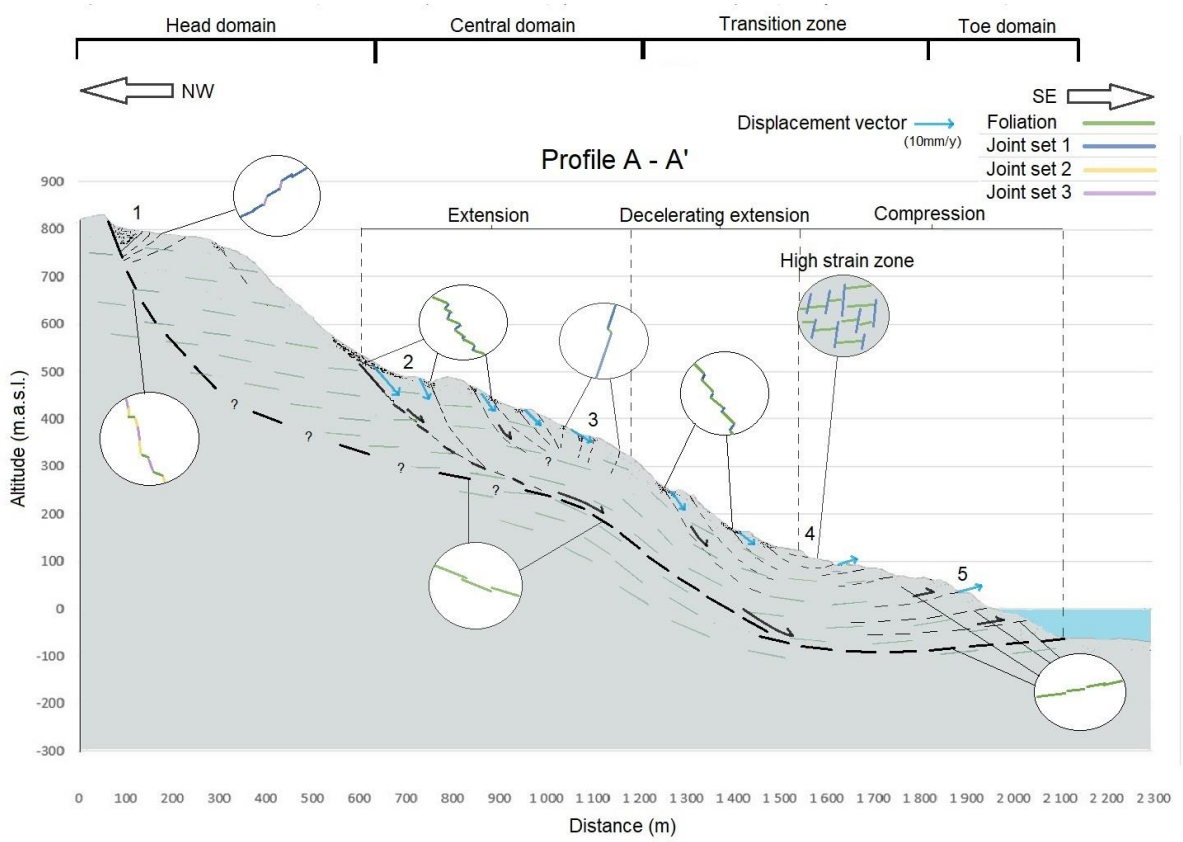

Figure 59: Profile A – A', a kinematic interpretation of the eastern side of Dusnjárga, Circles contain the interpreted dominant structure and step-fracture structure for the assigned parts of the slope. The zone with decelerating extension means a gradual transition from extension to compression.

Profile B – B'

The backscarp is structurally controlled by joint set 2 and 3, same as along profile A – A'. A block around 100 meters from the backscarp (fig. 60-1), show a few millimetres of annual displacement, while overall the head domain shows little movement.

Displacement starts at the upper section of the central domain with a dip of around 60°. Similarly to profile A – A', the vertical displacement rate gradually decreased while the horizontal displacement rate gradually increases to a point, interpreted as the transition between rupture surfaces. The horizontal displacement rate reaches a peak at around 400 m.a.s.l., at the same altitude as shown in profile A – A'. This supports the assignment of the point of transition between the rear and basal rupture surface in this area (fig. 60-2). Extensional morphological

features are also found along profile B – B’ in the central domain but are less prominent with a lot of the domain covered in disaggregated superficial material.

At the upper steeper section of the transition zone the foliation is steeper than the measured displacement-dip. This suggests that the foliation is not the sole controlling structure for the basal-rupture surface in the western part of the slope, but a combination of the foliation and joint set 1 (step-fracturing). The dip-direction of the foliation in the western part deviates with 30° from the overall slope movement, while slope movement and dip-direction of the foliation in the eastern parts are parallel.

Along the transition zone, the total velocity gradually decreases down-slope until the point of transition (fig. 60-3). After the point of transition, the 2D InSAR show variations in displacement-dip, varying from 40° to 5° above the horizontal plane, with the dip becoming more horizontal towards the end of the toe. Variations in displacement can be expected in an area of complex compressional activity such as in the toe of a large rock slope, where local buckling, compressional deformation or step-fracturing between prehistoric disjointed planes can occur (Stead and Eberhardt, 2013).

The western parts of the toe show less morpho-structural elements than in the eastern and middle parts of the slope. Bathymetry-data (fig. 33) show that the toe bulge extends further away from shore at the eastern and middle parts, while also showing higher density of mapped morphological features than in the west. The less favourable oriented foliation in the western parts of the slope, when compared to slope movement, could result in higher density of localised failures in that section. This could then be a major factor to why the western side is more disintegrated (fig. 32) and seemingly less displaced. Slope-movement in the eastern and middle parts runs parallel to the foliation and perpendicular to the strike of joint set 1, allowing morphological elements controlled by these structures to develop. While the slight deviation between direction of slope movement and dip-direction of the foliation in the western side means that these structures are less developed and could explain why the western side has more disintegrated superficial material than in the east.

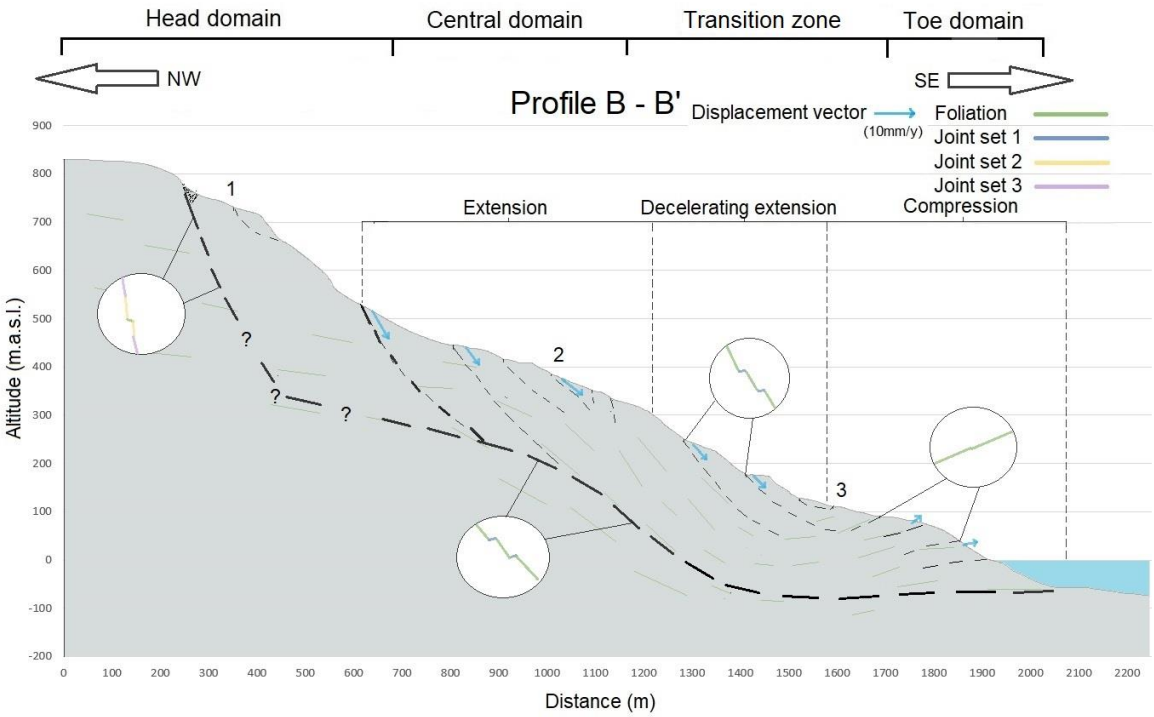

Figure 60: Interpretation of Profile B - B'. The foliation dips steeper than in the eastern and middle parts of the slope, which makes for slightly steeper displacement vectors. Circles contain the interpreted dominant structure and step-fracture structure for the assigned parts of the slope.

Profile C – C'

Profile C – C' shows a distinct backscarp controlled by joint set 2 and 3, with a trench and a series of counterscarps running in parallel. The counterscarps (fig. 61-1.) are mainly controlled by joint set 1 and there is close to zero movement in this part of the slope.

At the second major scarp (fig. 61-2) there is some movement. A previous investigation by Redfield et al., (2011), interpreted a local unstable block in this section of the head domain, displaying similar rates of displacement as the movement in the lower parts of the slide.

Movement is registered in the steep part between 700 and 600 m.a.s.l. (fig. 61). Dip and velocity of displacement in the steep section is very shallow and low (fig. 55) and seem unlikely to correlate with the block at the second major scarp (fig. 61-2), which had a noticeable higher displacement. Displacements in the steep section could instead be surficial slope processes due to the steepness of the slope. A combination of foliation and joint set 3 is likely the controlling structures of this block. Its rupture surfaces likely daylights directly beneath the second major

scarp, somewhere between 760–730 m.a.s.l. (fig. 61-2), but it does not register on InSAR measurements as there are no CSD points available on that part of the slope.

At the lower end of the profile there is a lobe shaped structure (fig. 61-3) showing movements of around 5 mm/year. This likely follows the same structures as at the second major scarp, foliation and joint set 3.

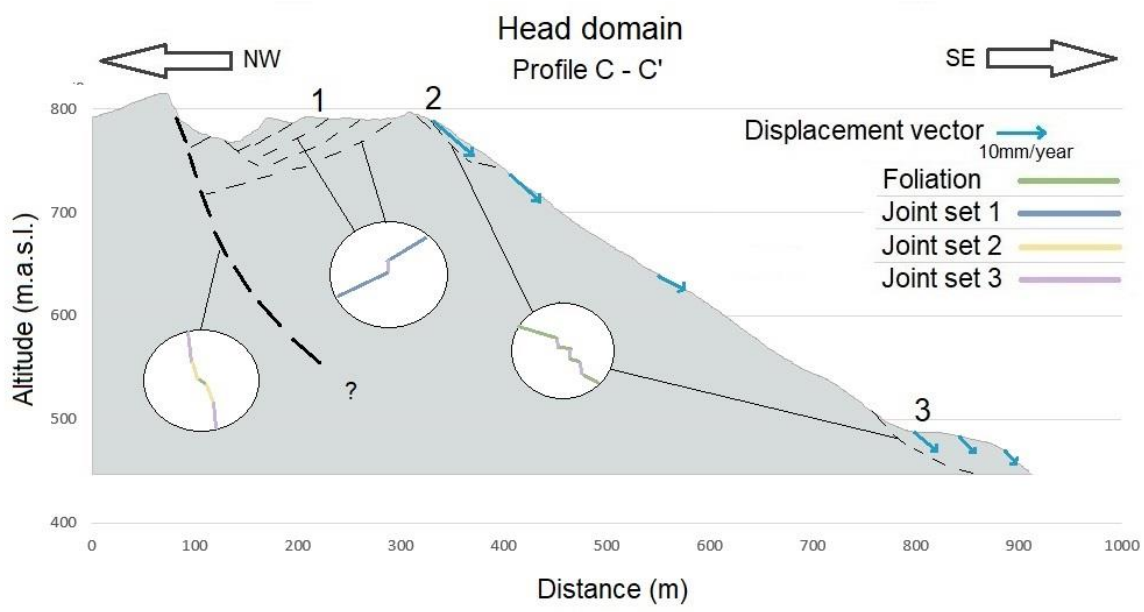

Figure 61: Profile C - C'. Interpreting the local instability at the head domain, as seen from InSAR data. Circles contain the interpreted dominant structure and step-fracture structure for the assigned parts of the slope.

Profile D – D'

The large, displaced block in the upper section of the transition zone (fig. 62-1.) show a displacement dip of 45° from horizontal, moving parallel to the foliation. Lower in the slope, the next large block in sequence has a displacement dip of 30°, reflecting the change in foliation. The two large blocks in the upper transition zone show distinct terraces and some local extensional features like secondary moving blocks and trenches along the terrace.

The change from a downwards slope movement to horizontal/upwards slope movement happens parallel with the change in orientation of the foliation, approximately at the point of transition (Fig. 62). The change from extension to compression is not instant, but it changes gradually from extensional to compressional along the first half of the transition zone, where

total velocity decreases (decelerating extension Fig. 59**).** After the point of transition, the total velocity stabilizes with a slight increase down-slope through the toe domain, as can be seen on Fig. 53, Fig. 54 and Fig. 56**.** A graben can be found at point "2" in Fig. 62, which is likely of extensional origin even though it is in a compressional part of the slope.

At the toe (fig. 62-3) there are compressional morphological features and a slight upwards slope movement according to displacement data. Just like profile A – A' and B – B', the velocity of slope movements seems to slightly increase towards the end of the toe. The slope kinematics depicting the lower area of profile B – B' and the transition zone D – D' corresponds well to a sub-circular rotation with an upwards thrusted toe area (fig. 26-j, fig. 27-i)

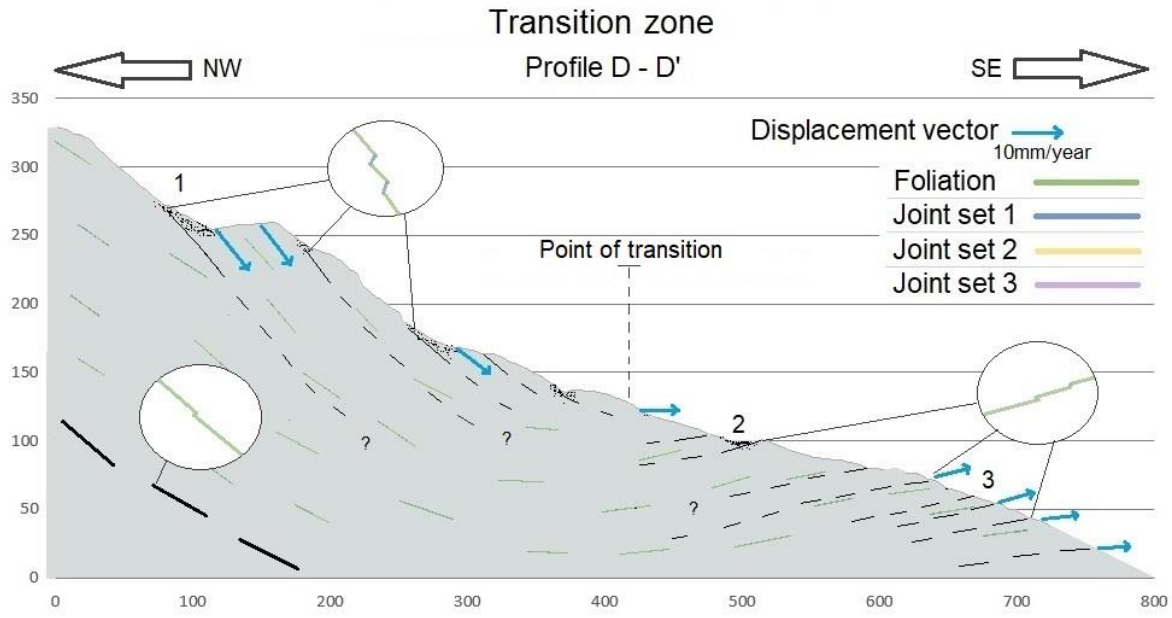

Figure 62: Interpreted kinematic cross section of the transition zone. Circles contain the interpreted dominant structure and step-fracture structure for the assigned parts of the slope

6 Discussion

6.1 Kinematic variability between data sources

InSAR and dGNSS are the two sources of displacement measurements in this thesis. The dGNSS data received from NGU is used and displayed without modification, while 2D/3D InSAR data combining multiple radar geometries had to be computed in the GIS-tool supplied by NORCE, for useful interpretation and visualization. InSAR Norway provides measurements from two different time series for the area of Dusnjárga, termed “Sentinel 1 Deformation” and “Sentinel 1 Deformation Old”, measuring years 2015–2020 and 2015–2019 respectively. The 2015–2019 dataset was selected for use in the interpretation of Dusnjárga. As the paths of the SAR satellites overlap increasingly towards the pole, 6 different datasets, 3 ascending and 3 descending, were available for Dusnjárga (fig. 63).

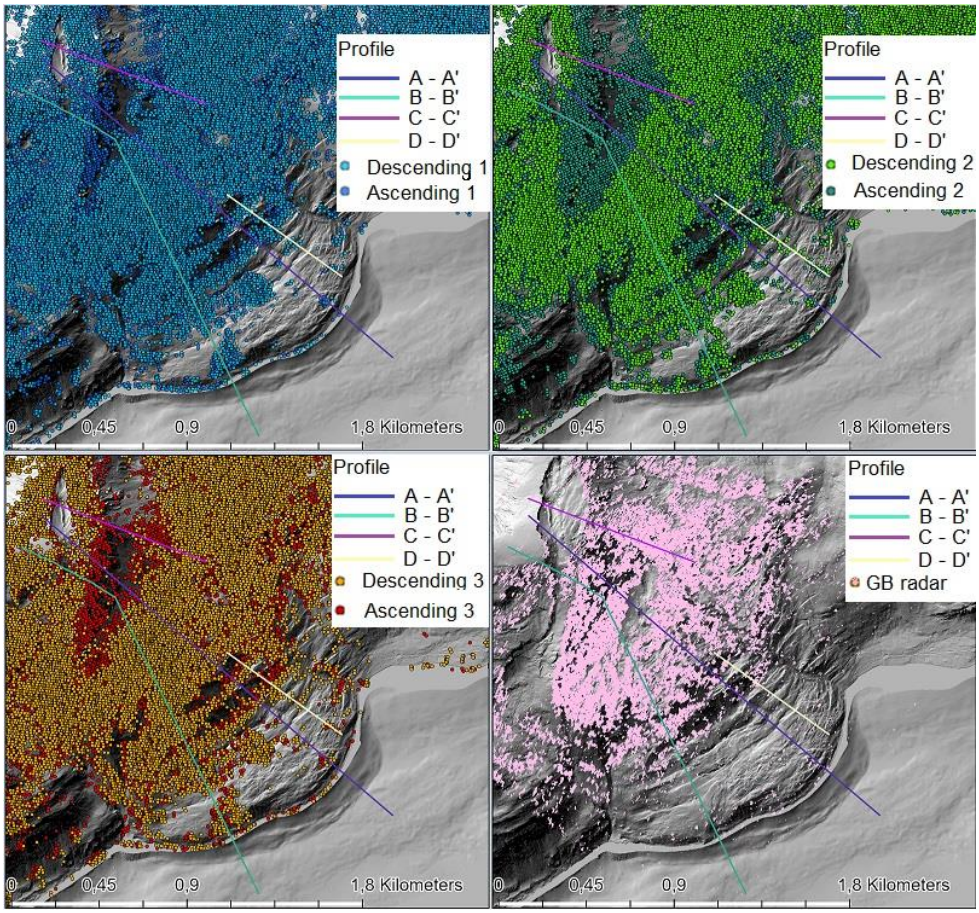

Figure 63: Registered distribution of measured displacement-points from all six Sentinel 1 Deformation Old (2015–2019) datasets and the GB-radar in relation to the four drawn profiles. Hillshade from 1 m DEM (Kartverket, 2021).

The datasets were tested to find which one suited the 2D profiles best, and what worked best with the GB-radar for 3D InSAR. If all 6 datasets were combined, the visualized InSAR data would have been quantitatively better, but would register less CSD points in parts of the slope with bad InSAR coverage. Since datasets were tested and showed similar displacement rates, datasets were chosen based on their spatial coverage along the slope.

6.1.1 InSAR limitations at Dusnjárga

Shadowing occurs mainly around the head domain at Dusnjárga. Shadowing can be observed on figure 63, where only one InSAR geometry (ascending) is able to document displacements. The steepest slope below the head domain, and the steep slopes in the transition zone are affected by both shadowing and layover, where no persistent scatterers are available. The most noticeable limitation is the vegetation in lower elevated areas, as shown in figure 32. Finally, the descending LOS and the GB-radar LOS share a similar direction looking from the southeast towards the northwest, which can be suboptimal as it can reduce the complementarity of the data for 3D calculation. However, the angle from the descending satellite is much steeper than the sub-horizontal angle of the GB-radar, causing a satisfying offset between their LOS. The GB-radar is placed like this to have an ideal LOS, by looking parallel to the anticipated direction of movement of the rock slope.

6.1.2 2D InSAR method

Interpretations of the kinematic cross-sections were based on horizontal and vertical velocities, decomposed from the combined 2D InSAR results. By visualizing the spatial variations of each decomposed displacement rate along terrain-profiles, a kinematic interpretation could be done by comparing them with the simple finite element simulations (Frattini et al., 2018), mentioned in chapter 4.2.1, as well as with mapped morphological structures. It should be noted that the simple finite element simulations are based on simple geometries, not large complex slopes such as Dusnjárga. These simulations have been compared to displacement data from large landslides (Frattini et al., 2018), and other slope processes (Sandbakken, 2021) in the past, but to make sense of the comparisons, there is a need for some individual interpretation. For large landslides, it can be useful to interpret separated parts of the slope before merging them into a final interpretation.

When using the 2D InSAR method it can be wise to experiment with different sample intersection radiuses, as done for Profile D – D' in this thesis. A radius of 20 was used for all profiles except profile D – D' which had a radius of ten. As described in chapter 4.2.1, the average displacement is calculated from all data points within the sample intersection radius. For local and sudden spatial variations in displacement, it is advantageous to have an intersection radius as small as possible. However, it is still important that both descending and ascending InSAR points can be found within the set radius, since both geometries are needed to calculate CSD points along the slope. If the sample intersection radius is set too small, compared to amounts of InSAR points nearby, the coverage of displacement points will be reduced.

Since there was a need for examining the transition zone in higher detail, a kinematic visualization with more detailed spatial variations was made for profile D – D'. Experimentation with smaller sample intersection radius has been proved useful for a more detailed coverage of kinematics in the central domain too, where noticeable displacement patterns and several morphological structures were discovered. However, a radius of 20 m was sufficient for interpreting general characteristics of this deformed slope.

6.1.3 3D InSAR method

A key factor when producing a 3D InSAR map is calibration of the GB-radar dataset to be compared with satellite InSAR. The calibration of the GB-radar data was challenging, due to the large discrepancy between the observation time windows of the satellite and GB datasets, and because the deformation rates seem to be largely nonlinear throughout the year.

Displacement vectors calibrated from a continuous annual displacement had a sub-southern orientation and minimal spatial change over the deformed rock slope, while displacement vectors calibrated from a 2-month active period were more southeast oriented and followed the slope morphology better. The fact that 3D displacement vectors seem to align better with the slope after seasonal active calibrations, supports the theory of a seasonal-driven deformation.

It must be taken into consideration that these calibrations are based on visual interpretation of the displacement data from NVEs dGNSS station. Also, the dGNSS time series is from January to December 2021, while the satellite InSAR spans 5 years, and the GB-radar measurements

were taken during a campaign in 2019, which means data is not from the same time series which means data can be affected by seasonal and yearly variations. Annual time series of climate/weather from the nearby weather station Sopnesbukt has been checked from the year 2019 and 2021, and they are found to be similar in temporal temperature variations, and quite similar in major rainfall events (Meterologisk institutt, 2022). However, it is hard to judge factors like thawing from a changing snow cover and change in the hydrostatic pressure etc. from historical weather forecasts. The periods in 2019 and 2021 are interpreted to be similar, but displacement data spanning over several years would have been needed to verify this trend.

6.1.4 Comparison between dGNSS and InSAR data

Due to little vegetation and favorable orientation in relation to LOS of both the GB-radar and the spaceborne geometries, the central domain is the best suited location for comparing different methods for measuring displacement. For comparison, average measurements from 2D and 3D InSAR CSD points were taken near the dGNSS stations "DUS_GPS_5" and DUS_GPS_4" (fig. 51), located in the central domain. The dGNSS stations show higher velocities than the 2D and 3D InSAR results (Table 5).

It seems like InSAR slightly underestimates displacement rates at Dusnjárga, while still staying within 0.4–1 cm (excluding uncertainty margin) of the dGNSS measurements (except for 2D InSAR at GPS_4). InSAR data has been compared to dGNSS measurements in previous studies, e.g. Eriksen et al., (2017), which has proven to correlate well. Most dGNSS data from both NGU and NVE span over a one-year period. A one-year period is not adequate to confirm exact displacement rates, since displacement rates can have annual fluctuations, as can be seen from dGNSS point DUSN_GPS_01 (Appendix 2). Many of the dGNSS points do not have measurements exceeding the uncertainty along both the horizontal and vertical vectors.

Even though there is a slight difference between dGNSS and InSAR displacement rates, the spatial variations within each dataset validate one another. 2D InSAR, 3D InSAR and dGNSS data show generally steep displacements at the central domain, with increased vertical displacement along the sub-circular large scarps of the central domain. Both datasets show horizontally dominated displacement at the toe domain, and dip angle slightly above the horizontal plane.

Table 5: Comparison of InSAR and dGNSS displacement data from both the western and eastern side of the central domain.

Western side of the central domain (at dGNSS point DUS_GPS_5)		Eastern side of the central domain (at dGNSS point DUS_GPS_4)	
Method	Total displacement	Method	Total displacement
dGNSS (DUS_GPS_5)	14.0 mm/y (+-5.8)	dGNSS (DUS_GPS_4)	19.1 mm/y (+-5.4)
2D InSAR	6.8 mm/y	2D InSAR	7.1 mm/y
3D InSAR	10.0 mm/y	3D InSAR	11.0 mm/y

From comparing the three different displacement methods, 3D InSAR-data is closer to the dGNSS-data, than what the 2D InSAR-data is. 3D InSAR is expected to have more accurate measurements than 2D InSAR since it has a more comprehensive integration of movement components, by utilizes three geometries instead of two. This highlights that 3D InSAR gives an improved accuracy in displacement-data, which then should be utilized if conditions allow it.

6.2 Advantages and challenges of photogrammetry for large rock slope deformations

It is imperative to plan every aspect of the field trip when gathering optical imagery by drone. Weather and light conditions can greatly affect the picture quality. Apps like DroneDeploy make it a lot easier to get consistent data, both from planning a flight route and setting consistent camera settings. Even if pre-selected settings were set, it seems like the angle of incident might have changed a little during the flight, which caused a “double” ground level that was hard to filter out. Vegetation proved difficult to filter out, and it would be very time consuming to get a result any better than what was produced.

The DEM created was of 0.2 m resolution, certainly more detailed than the 1m DEM, available from the Norwegian Mapping Authorities, but included some noise. The new detailed DEM proved not to be very useful for morphological mapping of this scale. The 1 m DEM proved sufficient, as any finer detailed structures discovered on the 0.2 m DEM only repeated the orientation of the larger structures without finding any new information. That is not to say that photogrammetry would not be useful in projects focusing on smaller areas, but for the sake of a large unstable rock slope, it was sufficient with the 1 m DEM. Other than the DEM, the drone photos taken in free flight, overlooking different parts of the slope, were useful for the morphological mapping.

6.3 Characteristics and classification of Dusnjárga

6.3.1 Active and inactive parts of the rock slope

The backscarp at the head domain has a large offset to the block underneath, which clearly suggests previous displacement. The head domain (170000 m^2) is inactive (not moving). There are displacements of 3–4 mm/year along a scarp at profile B – B' (fig. 60), but generally displacement rates are as low as 0–2 mm/year, except for the moving block depicted in profile C – C' (fig. 61-2). The block shows displacement rates up to 10–15 mm/year from the InSAR data and 7 mm/year from dGNSS measurements. Differences between InSAR and dGNSS measurements can be due to the placement of the dGNSS device, which measures an exact point instead of a pixel measurement with a 5x20 m initial resolution from an average of chosen sample intersection radius. Nonetheless, this particular block can be considered actively deforming.

Noticeable displacement at the active part of Dusnjárga begins in the scree slope between the head and central domain. Measured displacement in the scree is uniform in terms of displacement rates and dip for profile A – A' and B – B'. The dip-angle of displacement is steep, similar to the dip of the visible sub-circular scarps below the scree-slope, supporting the theory of displacement underneath, as opposed to a superficial process in which displacement would be aligned with the slope.

The lateral limits of the active rock slope deformation are clearly defined both from InSAR data (fig. 24, fig. 57) and from morphological structures (Appendix 15). The eastern lateral limit

shows an abrupt change in velocity between the actively deforming slope and the inactive eastern parts. The eastern limit northeast of the central domain consists of two scarps, where both scarps seem to be actively deforming. The western lateral limit is also morphologically clearly defined, while having a more gradual transition from active to inactive slope deformation than the eastern side, based on InSAR velocity. Morphological evidence such as scarps and counterscarps, as seen on appendix 9, shows that there are inactive lateral limits on both sides of the deforming slope.

The total area of the active slope is 1.32 km^2, including the central domain, transition zone and toe domain. Displacement rates for the active rock slope of Dusnjárga seem to be between 10 and 15 mm/year on average, with high velocities in higher altitude areas and a gradual decrease down-slope. Along the backscarp of the central domain, displacement rates might be up to 20 mm/year according to dGNSS measurements. As mentioned previously, most of the measurements at Dusnjárga are based on one-year measurement-periods. For quality assurance, in regard to displacement data and for validating seasonal trends, measurements spanning over several years would be necessary.

6.3.2 Structural control in the active parts of the deformed rock slope

The lithology at Dusnjárga is mainly made up of metagabbro, some amphibolite and a thin layer of mylonite at the head domain. In addition to the structural mapping (chapter 5.2) and interpretation (chapter 5.7) from this thesis, a simultaneous master-project focusing on the structural geology at Dusnjárga has been done by Emilie Jensen Aamodt (unpublished). Thin sections revealed that at least two distinct micro fracture sets are commonly found throughout the slope, where one has a parallel orientation to the foliation, while the other is oriented normal to the foliation. Point Load tests and Uniaxial Compressive Strength tests were performed, which implied that the slope of Dusnjárga had anisotropic properties. The rock strength was naturally high at samples with little to no inherited fractures, while in most samples the rock failed relatively early along the weak inherited fracture-sets. The thin sub-horizontal mylonite layer (chapter 5.2.5) discovered in the backscarp, could have impacted the initial deformation at the head domain, although it does not follow the orientation of the rear rupture surface.

Head domain block

The head domain is relatively stable but has one active block with noticeable displacement. This block is likely controlled by step-fracturing between joint set 3 and the foliation (fig. 61). The rupture-surface of this block should exit in the slope somewhere between 730–760 m.a.s.l. where there is a lack of CSD points to confirm displacement.

Rear rupture surface

From displacement dip angles based on the 2D InSAR method and validated with the 3D InSAR results, the rear rupture surface starts dipping underneath the scree slope at an angle of 50–60° (fig. 59, 60). The scree is a disintegrated superficial material which overprints the kinematics from the solid bedrock underneath. Which can somewhat alter the true deformation beneath the scree. For this reason, the dip from the underlying rear rupture surface might differ slightly from the superficial measurements. Displacement vectors of the rear rupture surface can be compared with the simple finite element simulations from Frattini et al., (2018) (fig. 27) to interpret the rupture surface geometry.

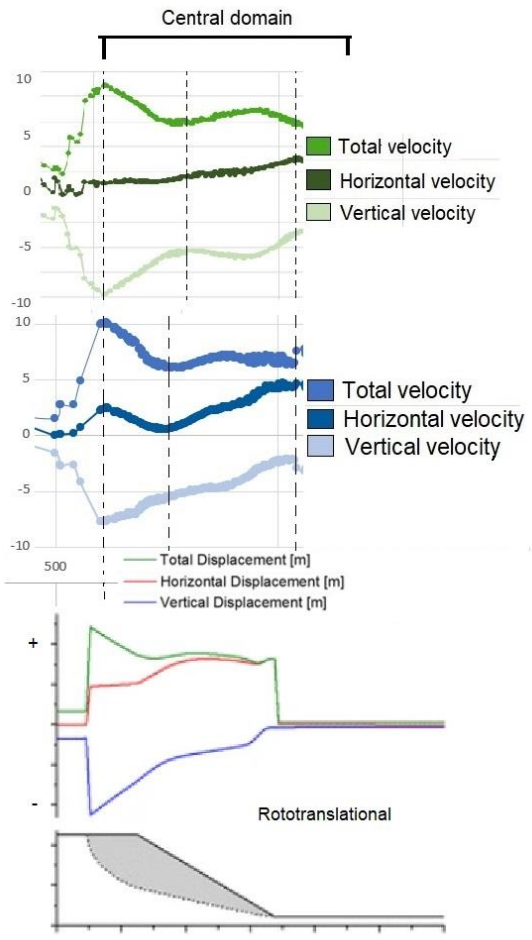

Figure 64: Kinematic displacement from profile A – A' (blue) and profile B – B' (green) compared with a roto-translational simple finite element simulation from Frattini et al., (2018).

The rear rupture surface at Dusnjárga is similar to the roto-translational simple finite element simulation (from fig. 27-c). The vertical displacement is dominant at the backscarp, in the upper parts of the central domain. The vertical velocity is gradually decreasing down the slope, while the horizontal velocity becomes more dominant as the rear rupture surface gradually dips shallower. The velocity graph (fig. 64) is cut off where the rear rupture surface is interpreted to transition to the basal rupture surface, since kinematic patters follow the foliation from that point on. The sub-rotating kinematic pattern at the backscarp is not necessarily true rotational geometry, but rather step-fracturing between joint set 1 and the foliation, where the dip of rupture surface decreases with depth and becomes more listric (Vick et al., 2020, Stead and Eberhardt, 2013).

Basal rupture surface

Kinematics from the 2D InSAR method show that displacement vectors follow the foliation from the lower end of the central domain and down to the toe. It seems like the foliation has a gentle anticlinal fold between the central domain and the start of the transition zone. Subsequently the geometry of the basal rupture surface is proposed to follow an anticlinal fold at this section of the slope. Such a geometry would cause this section of the slope to have extensional features at the slope surface, which would explain the numerous morphologic depressions and surface fractures found at the lower part of the central domain (fig. 37). Scanline 5 suggests a highly extensional area at the top of the transition zone (fig. 48), showing

the highest density of joints per meter, almost double the amount of joints compared to scanlines 2 and 6 taken in the compressional toe, which have a similar density of joints.

Down-slope from the gentle anticlinal fold is the transition zone, in which the basal rupture surface follows the foliation in an open non-cylindrical synclinal fold (fig. 43). The strike of foliation turns more W-E-oriented towards the western parts of the slope, making the fold hinge-line non-cylindrical. The fold limb is steep, 50–60° at its steepest in the upper parts of the transition zone. The other fold limb, going through the toe area, dips gently into the slope at 10–20°, and gets gradually more horizontal towards the end of the toe. Foliation seems to be the main controlling pre-existing structure along the basal rupture surface, validated by strength tests from co-student Emile Jenssen Aamodt. Joint set 1 is also linked to some features such as counterscarps and morphological depressions at the toe domain.

As seen on cross section A – A' and B – B' from chapter 5.7, it is uncertain whether the inactive backscarp at the head domain could be linked with the active slope of Dusnjárga. The head domain has had substantial displacement with its offset from the back scarp, however no clear exit of its rupture surface can be traced along the mountainside north of active Dusnjárga. The path of the rear-rupture surface at the head domain remains therefore speculative, but it remains inactive for now.

6.3.3 Relative dating and development of slope deformation

Relative dating

The identified shoreline cross-cutting the eastern lateral flank at the toe domain has previously been mapped further east of Dusnjárga and was proposed as a Tapes shoreline by Frederic Blau (2020). As mentioned in section 5.6, isobase lines matching dated Tapes transgression shorelines at Ullsfjord, Lyngen (Corner and Haugane, 1993) go through Lille Altafjord. Additionally, isobase maps depicted for 8000 years BP (fig. 65) (Møller, 1987) show that the 20-meter elevated isobase line is just north of Dusnjárga, further suggesting an early Tapes origin.

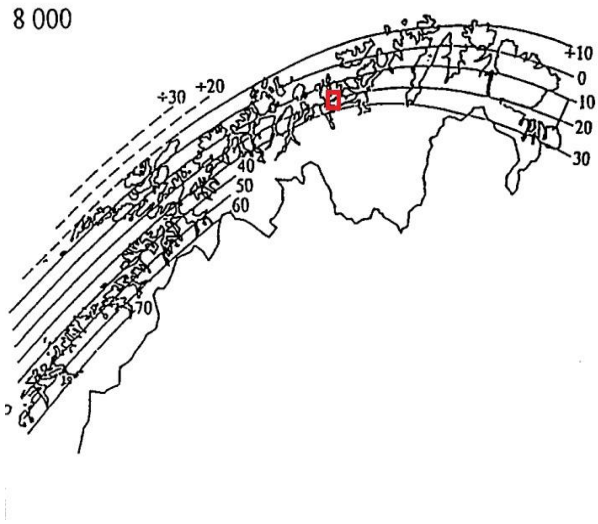

Figure 65: Isobase map of northern Norway at 8000 BP, depicting relative sea level surfaces to the set age. Red square marks the approximate location of Dusnjárga. Adapted from (Møller, 1987).

Based on dating of nearby Tapes shorelines with a shared isobase line, as well as matching the elevation of a relative dated isobase map (Møller, 1987), a proposed age of 7000–8000 years BP old is set for the shoreline. Note these dates are uncalibrated due to uncertainties in the reporting convention from source material. As seen on figure 58, the shoreline elevation is affected by the cross-cutting of both the inactive lateral limit (1–2 m offset) and the active lateral limit (8 m+ offset), which means that both stages of deformation were active sometime after 7000–8000 years BP.

Studies dating prehistoric catastrophic avalanche deposits from southwestern Norway (Böhme et al., 2015, Hermanns et al., 2017) have shown that the majority, and especially the large rock slope failures >5x10^6 m^3, have had their initial failure directly after deglaciation of the area. Even though those studies focused on catastrophic rock slope failures, it is not unlikely that slow deforming rock slopes had their initial activation following the deglaciation, as they are often initiated by similar factors like inherited weak structures, mass erosion and increased hydrostatic pressure. In addition to a large number of failures happening directly after the deglaciation, another peak of high avalanche frequency was recorded after 9000 years BP.

From sediment logs containing a high degree of slope debris, within sediment layers suggested to have a near Tapes origin (Blau, 2020), high deformation has been suggested for the eastern parts of the transition zone. Which further suggests an active deformation in the time following the Tapes transgression, but without evidence to when the initial deformation started.

Based on the retreat of ice sheets at Dusnjárga, visualized in chapter 3.3.3 (fig.18), and the fact that many catastrophic rock slope failures seem to be related to deglaciation, it can be assumed that the initial deformation of Dusnjárga started close to 13–14 ka. But this is indeed speculative

and further research with more precise dating methods is needed to confirm any age of initiation.

The relative dating between the inactive and active lateral limits is difficult to determine. Even though one is currently active, and the other is not, their relative start of deformation could have happened simultaneously or by one failure influencing the other.

Structural development within the slope

The active parts of Dusnjárga have an uncommon flow-like geometry with well-developed morphological features. It was hard to find similar deformed rock slopes in the literature. In fact, a rock slope with similar appearance and lithology, as well developed as Dusnjárga, and with a rotational fold-element in the toe, has to my knowledge not been documented.

The lower half of the transition zone and the toe domain has a slightly upwards-inclined movement, as can be seen on cross sections in chapter 5.7, which translates to compression in these areas. However, local morphological structures found at the toe domain, mapped in chapter 5.1.3, and shown by examples in figure 66, suggest that there has previously been extensional movement in the toe domain. This is further supported by mapping of the paleo shoreline, discussed in chapter 5.6, which shows a distinct overall downward movement of the shoreline, in an area with presently upwards movement.

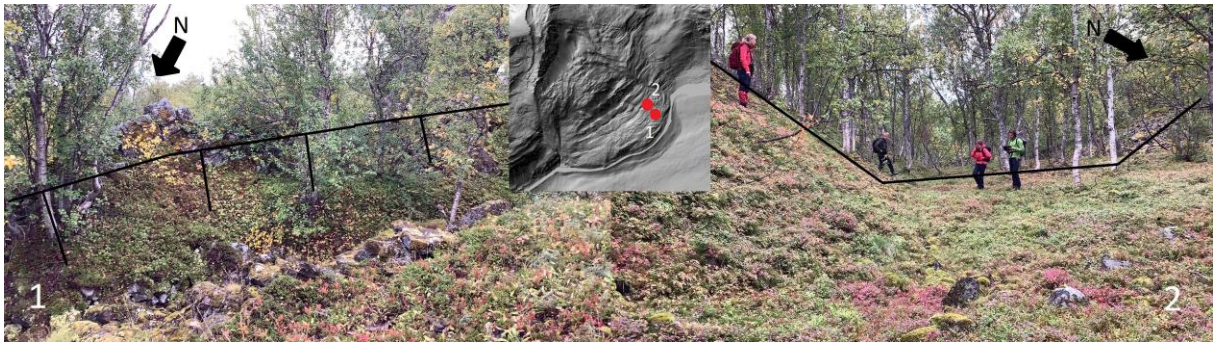

Figure 66: Extensional structures from the transition zone/toe domain. 1: A counterscarp in the toe domain, joint controlled and dipping steeper the foliation. 2: Between the transition zone and the toe domain there was a graben structure with 30° steep walls. Photos: Simen Bekkevoll

The presence of extensional features in the compressional toe can be due to the slope evolution, as shown in figure 67. At initial release (fig. 67-1), the slope from the transition zone and further down, would have been steeper than it is today. When the scarps began to develop (fig. 67-2),

most of the transition zone and upper parts of the present-day toe would have had extension, while only a small part of the toe would have been compressed. These initial scarps would not have followed the sub-horizontal foliation at lower elevated parts of the slope but would have developed along joints. As the slope continued to deform (fig. 67-3), more material would be pushed through the toe area, resulting in a larger toe and more material in the zone of compression. The previously joint controlled parts of the slope would now have gotten displaced to the toe domain, resulting in a transition from joint to foliation-structural control. At present day (fig. 67-4), the toe area has gotten substantially larger, and parts of the slope with initial extension have been moved down to compressed parts of the slope.

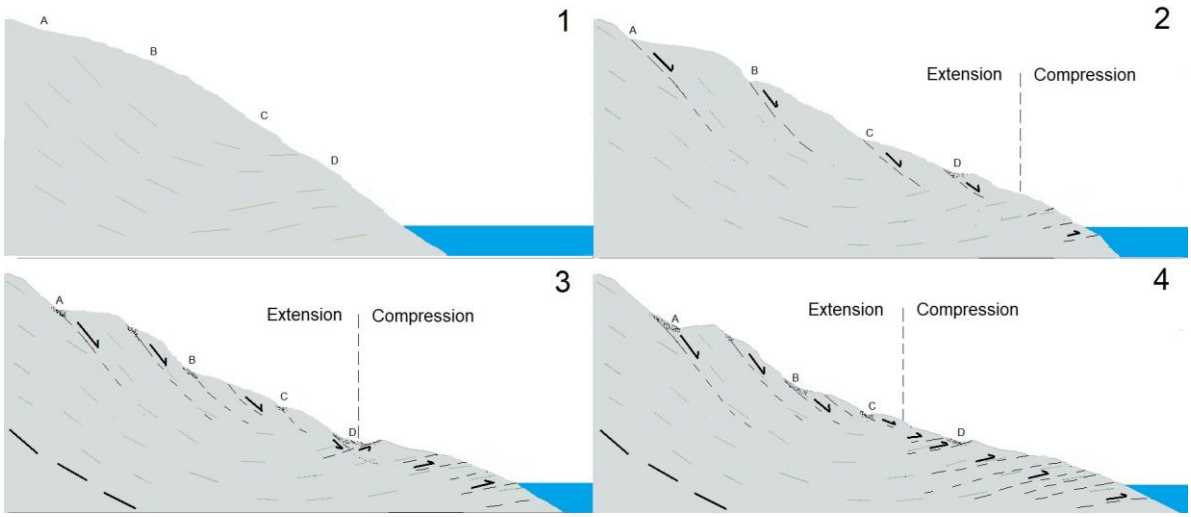

Figure 67: A figure suggesting how the transition zone and the toe domain could have evolved from initial failure (1) to present day (4). The transition between extension and compression happens gradually, but it gets further away from the fjord as more material builds up in the toe domain. Letters A-D are visual references placed to easier follow slope evolution.

There has been a substantial total displacement of the slope, with somewhat higher displacements in the lower half of the rock slope than the upper half, based on the large morphological structures and the extended toe. The slope also seems to have had higher displacements towards the middle of the slope, based on the shoreline evolution and general shape of the toe. Due to the short measurement series, there are still uncertainties with respect to present day displacement rates, especially in the toe area. A conclusion can therefore not be taken before a longer time series has been obtained.

A rough estimation of an average displacement rate at Dusnjárga was done by measuring the assumed distance of displacement at the toe. This distance was measured to be 300 horizontal meters, which probably underestimates the displacement, as this is the 2D horizontal component of the displacement, and not accounting for the overall 3D displacement. If a maximum timeline of deformation is set to 14 ka, following the deglaciation, annual displacement would be around 2.1 cm/year, which seems to be slightly more than today. If the initiation of the deformation was later than this, the average velocity would increase, which means that present displacements would be noticeably lower than the overall average. It should be noted that this was an estimate of the average displacement in the toe domain, which do not necessarily translate directly to the other domains.

At present time, the central domain of the active rock slope deformation shows higher displacement rates than the lower elevated parts. Which is contradictory to the overall displacement of the slope, where morphological structures suggest a larger displacement in the transition zone/toe domain than in the central domain. This could suggest some retrogressive characteristics, where large displacements in the transition zone/toe domain destabilized the central domain and allowed for increased displacement in the upper elevated parts. All while the toe domain received more displaced material on a shallower basal rupture surface which gave a stabilizing effect.

As can be seen on figure 41, there are several morphological depressions that have a 40–50° offset from the direction of slope movement. These depressions could be shear fractures, related to the increased displacement toward the middle of the slope. As mentioned in chapter 6.3.2, two small scale fracture sets were commonly observed in thin sections, from co-student Emile, one parallel to the foliation and one normal to the foliation. The fracture set normal to foliation is probably related to joint set 2 or 3 and could be the one allowing for higher displacement in the central parts of the slope.

In the western parts of the slope, displacement is generally less than in the east, while the grade of disintegration on the surface is higher (fig. 32). This could be explained by the change in foliation dip-direction (fig. 43), which happens along the western side of the slope. The change of foliation dip-direction at the western side is less optimal relative to slope movement than

dip-direction in the eastern parts of the slope is. This offset between orientation of the weak foliation and the gravitational strain in the western part, could explain why the western area is more disintegrated and has less developed morphological features. It could also explain why the lateral change in displacement is less abrupt along the western lateral limit compared to the eastern lateral limit. Since a more disintegrated mass will be displaced more gradually when moving away from the main body than a coherent mass with strong bonds.

On the geomorphological map (fig. 33) a lineament can be seen in the bathymetry data, going obliquely from the middle of the slope and upslope towards west. This lineament has the same features as the paleo shoreline, as it gradually has lower elevation towards the middle of the slope, which could suggest it has a pre-failure origin.

6.3.4 Classification of Dusnjárga

According to the Varnes classification system, updated by Hungr et al.,(2014) (table 1), both RSDs and MSDs occur in large mountainous areas. Morphological structures like scarps, trenches, bulges, terraces, and surface cracks can be found in both deformation types, but without confirmation of a fully defined rupture surface. It is stated that MSDs and RSDs share a lot of common characteristics, with the main difference being their size (Hungr et al., 2014). Movements in MSDs are usually in the order of unmeasurable to extremely slow, while RSDs usually move from extremely slow to slow (table 2). While MSDs typically start from the mountain peak and deforms all the way down to the valley floor at 1 kilometer in relief or more, RSDs typically start somewhere within the slope and can range between a few tens to a few hundreds of meters in relief.

The active part of Dusnjárga runs from the start of the central domain (520 m.a.s.l.) and down to the basal rupture surface exit at the toe (approximately 100 m.b.s.l.). Overall displacement rates are in the extremely slow category, with certain areas moving slow (table 2). With these observations in mind, it seems logical to classify the active slope of Dusnjárga as a large RSD. Had the head domain been a part of the actively deforming slope it would probably have been classified as an MSD.

The slope can also be classified as a DSGSD, which can be very large in size, up to hundreds of millions of cubic meters in volume and a few hundred meters thick (Soldati, 2013). A rough

volume-estimate of the maximal extent of the active Dusnjárga, based on the average thickness of the deforming slope, gave a total volume of 180 million m^3, which is indeed a large rock slope. A well-developed drainage network is often found in DSGSDs (Crosta et al., 2013), as seems to be the case for Dusnjárga. Multiple gullies run along the slope (fig. 33, Appendix 15), but none of them contains running water, suggesting they might have a morphological origin rather than a water-eroded one.

Dusnjárga is a complex slope, where deforming-mechanisms in the slope are challenging to classify. Based on kinematic data presented in this thesis, the rear-rupture surface shows some roto-translational characteristics, but as the backscarp of the active RSD is located underneath scree deposits, it cannot be validated by field measurements. Because of typically strong rocks in Norway, true rotational slides are rare since they typically form in weathered or softened clay shales (Singh and Goel, 2011). But in this case the "rotational" movement in the backscarp is interpreted as step fracturing, following inherited weak fracture-zones in the rock, identified by co-student Emilie.

The basal-rupture surface is complex, following the foliation through both a gentle anticlinal and an open synclinal fold, making it an irregular basal rupture surface (Clague and Stead, 2012). Displacement has a dip similar to the foliation, almost without any abrupt changes from the lower half of the central domain and down to the toe, suggesting a generally coherent mass-movement along the basal rupture surface. Which would imply that the RSD has some translational characteristics as well. In the transition zone however, there is some change to the velocity vectors, which correlates to movement at the large scarps present.

We can assume that the RSD is a bi-planar slope deformation, as the start of the rear rupture surface is controlled by a joint set that is steeper than the foliation and would not daylight by itself at the toe. There is also compression at the toe due to a sub-circular motion preferring the direction of the weak foliation in the synclinal fold. Movement along the rupture surface can therefore be classified as a complex, biplanar and irregular compound deformation.

6.4 Hazard analysis of Dusnjárga

Interpretations and results from this study are inserted into the recommended hazard classification system from NGU (Hermanns et al., 2012b). A total of nine categories

corresponding to the possible failure of the slope are assessed (table 6). It is possible to add an uncertainty to each criterion in the different categories.

Backscarp

The backscarp at Dusnjárgas active slope is under masses of scree, but several secondary scarps run across the whole area and transitions into the lateral limits on each side. The backscarp gets one point for a fully open backscarp over the whole width of the slope.

Potential sliding structures

In the upper part of the slope, the foliation is generally steeper than 20°, but it gets shallower towards the toe and eventually dips into the slope at the toe, at a lower angle than 20°. The foliation has parallel weak shear zones developed, with visible planar failures within the slope. The two fields of penetrative structures both got three points.

Lateral release surfaces

The lateral release surfaces are very well developed at Dusnjárga, giving this category one point for fully developed on both sides.

Kinematic feasibility test

The software called Dips8 (from: https://www.rocscience.com/) was originally used for simple slopes like roadcuts (Stead and Wolter, 2015), and not well adapted for the complex structures and failure mechanisms found at Dusnjárga. Therefore, the kinematics are interpreted by comparing 2D InSAR and structural measurements. Since tests of different failure processes have not been done in Dips8 or other softwares, one point for uncertainty is set in the first field which does not allow sliding of any sort. Then three points are set in the field stating: that failure is kinematically possible along persistent discontinuities (foliation).

Morphologic expression of the rupture surface

Continuous deformation is observed along the whole RSD, at both lateral limits and at the end of the basal rupture surface. Therefore, one point is given to the field displaying high morphological expression.

Displacement rates

Displacement rates at Dusnjárga vary throughout the slope from <10 mm/year to close to 20 mm/year for certain places, therefore one point is given to each corresponding field.

Acceleration (if velocity is between >0.5 cm/year to <10 cm

The assumed distance of displacement at the toe of Dusnjárga was measured to be 300 horizontal meters, which was used to get a rough estimation of the total average displacement rate. Average displacements rates were based on the maximum timeline at 14 ka, following the deglaciation, which resulted in 2.1 cm/year, which seems to be slightly more than what it is today. However, this is probably an underestimation of the average displacement, at least for the toe, as it was based on the horizontal 2D displacement and not the total 3D displacement. If the deformation started before the deglaciation of the area, an acceleration could be present in the central domain, however that seems unlikely based on previous studies on the topic. A present acceleration of the slope deformation is therefore unlikely.

Increased rockfall activity close to the deformed slope

Examination of the surrounding areas showed that rock fall activity was active in all surrounding steep slopes. There is no evidence of specific increase of activity in the RSD area. One point was given for no increased rockfall activity.

Past events

No past events have been recorded at Lille Altafjord.

Table 6: Categories for hazard classification.

1. Back-scarp	Score	lorm. prob
Not developped	0	
Partly open over width of slide body (few cm to m)	0	
Fully open over width of slide body (few cm to m)	1	100,0 %
2. Potential sliding structures	**Score**	**lorm. prob**
No penetrative structures dip out of the slope	0	
Penetrative structures dip on average < 20 degree or steeper than the slop	3	50,0 %
Penetrative structures dip on average > 20 degree and daylight with the slo	3	50,0 %
3. Lateral release surfaces	**Score**	**lorm. prob**
Not developped	0	
Partly developped on 1 side	0	
Fully developped or free slope on 1 side or partly developped on 2 sides	0	
Fully developped or free slope on 1 side and partly developped on 1 side	0	
Fully developped or free slope on 2 sides	1	100,0 %
4. Kinematic feasibility test	**Score**	**lorm. prob**
Kinematic feasibility test does not allow for planar sliding, wedge sliding or t	1	25,0 %
Failure is partly feasible kinematically (movement direction is more than ±30	0	
Failure is feasible kinematically (movement direction is less than ±30° to slo	0	
Failure is partly feasible kinematically on persistent discontinuities (moveme	0	
Failure is feasible kinematically on persistent discontinuities (movement dire	3	75,0 %
5. Morphologic expression of the rupture surface	**Score**	**lorm. prob**
No indication on slope morphology	0	
Slope morphology suggests formation of a rupture surface (bulging, concav	0	
Continuous rupture surface is suggested by slope morphology and can be	1	100,0 %
6. Displacement rates	**Score**	**lorm. prob**
No significant movement	0	
>0 - 0.5 cm/year	0	
0.5 - 1 cm/year	1	50,0 %
1 - 4 cm/year	1	50,0 %
4 - 10 cm/year	0	
> 10 cm/year	0	
7. Acceleration (if velocity is >0.5 cm/yr and <10 cm/yr)	**Score**	**lorm. prob**
No acceleration or change in displacement rates	1	100,0 %
Increase in displacement rates	0	
8. Increase of rock fall activity	**Score**	**lorm. prob**
No increase of rock fall activity	1	100,0 %
Increase of rock fall activity	0	
9. Past events	**Score**	**lorm. prob**
No post-glacial events of similar size	1	100,0 %
One or several events older than 5000 years of similar size	0	
One or several events younger than 5000 years of similar size	0	

These inputs result in a hazard matrix seen on figure 68. The hazard classification is simulated to medium with an average 7 points and with a maximum of 8 points, which is high. It almost exceeds the 1/1000 nominal annual likelihood danger level, which could restrict new infrastructure in the area.

Locality	Dusnjárga
Performed by:	Simen Bekkevoll
County:	Troms
Date:	06.05.2022

Hazard classification	Likelyhood
Very low	0,0 %
Low	0,0 %
Medium	62,5 %
High	37,5 %
Very high	0,0 %

Hazard points	
Minimum	5,50
Maksimum	8,00
Modus	6,50
Gjennomsnitt	7,00
5% persentil	5,50
95% persentil	8,00

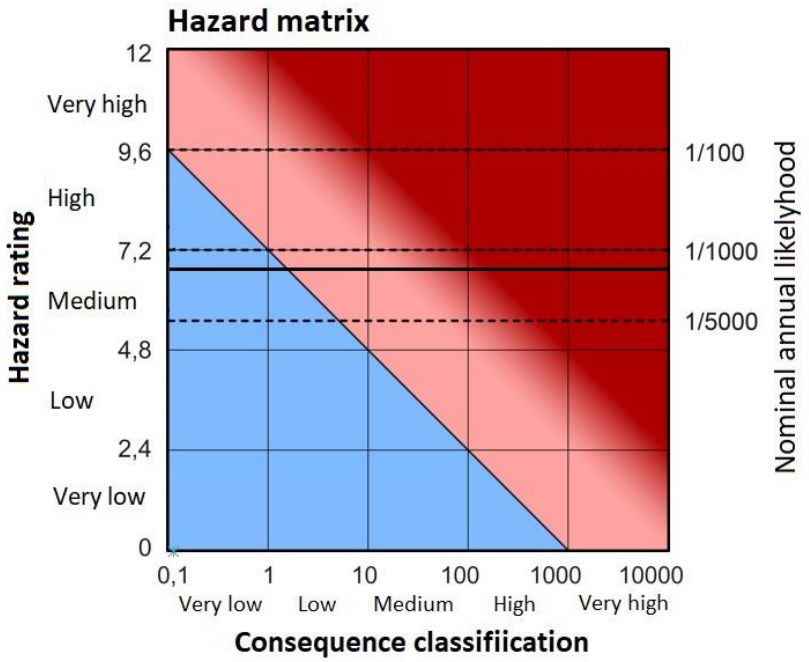

Figure 68: Hazard classification at Dusnjárga, based on table 6. Method for evaluating hazards was adapted from (Hermanns et al., 2012b) NGU.

Possible over-estimation of the hazard classification at Dusnjárga

The hazard rating does not consider the large, compressed toe area. With such a large area, and with a failure plane (foliation) dipping into the slope, an enormous amount of force will be needed to displace the wide toe area. A simple geotechnical method of interpreting stability in a slope is to compare driving forces that lead to failure in the slope (gravity/weight) with resisting forces (friction against rupture surface and counterweight) (fig. 69). Although this is most commonly referenced when dealing with soils (Abramson et al., 2001, Ishibashi and Hazarika, 2015), and is a simplified take on slope stability, the same principles apply for rock slopes.

As Dusnjárga further develops, increased load will be added to the toe, which works as a counterweight to the upper parts exerting force. This theoretically means that Dusnjárga should become more stable as the slope further develops, due to increased failure-resistant forces.

According to the Norwegian Centre for Climate Services, the future climate in Norway will likely not increase the risk of rock slope failures, however it is a prediction with some

uncertainty (Meteorologisk Institutt, 2021b). However, they also predict an increase in episodes with extreme precipitation, which is a triggering factor for certain landslides.

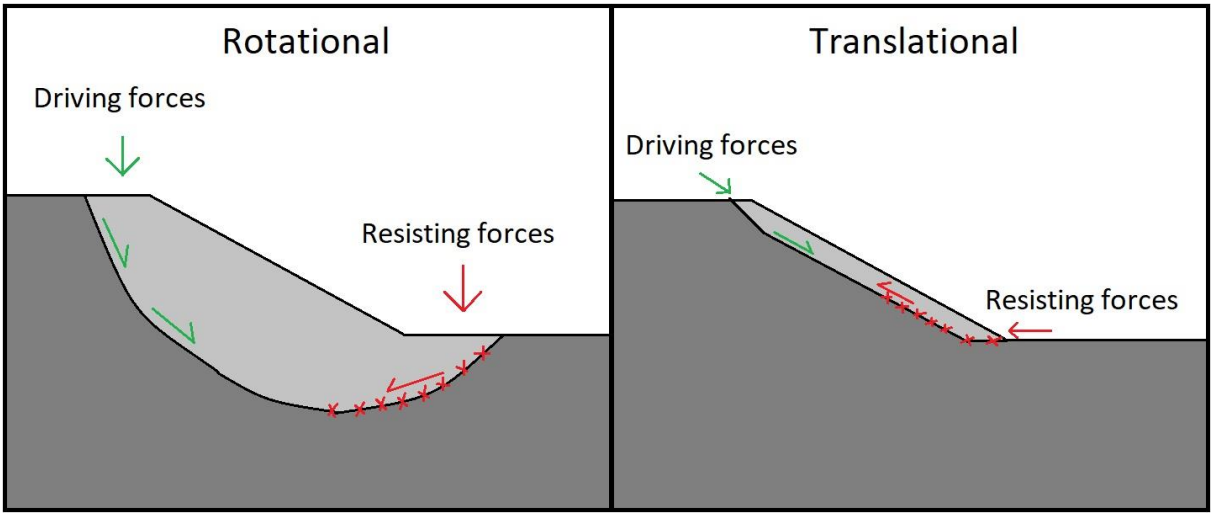

Figure 69: Simple sketch of how counterweight and friction along the rupture surface are resisting driving forces of a slope deformation.

6.5 Suggestions for future research

The hazard analysis presented above did not include consequence/risk classification, which is normally done by NGU. This hazard analysis can therefore serve as a basis for any further risk assessment of Dusnjárga.

The overall displacement estimates at Dusnjárga are still somewhat uncertain, as there is a lack of measurements during longer timeframes. More data should be gathered to better interpret and calibrate InSAR data and to try to explain the seasonal variations of deformation with respect to triggering factors like thawing, melting, heavy rainfall or increased porewater pressures. Additionally, experiences from this study have shown the importance of long and continuous time series when it comes to measuring displacement of rock slopes in general, as shorter periods of activity can increase the uncertainty of measured InSAR displacement and make it challenging to calibrate extra datasets to match. Especially when it comes to merging satellite and ground based InSAR data for 3D InSAR, data of seasonal displacement variations is important.

A future study could look for seasonal displacement trends from numerous rock slopes where dGNSS stations are present and have displacement rate measurements over annual time series.

If a trend in varying displacement could be documented to match seasonal trends, like thawing, temperatures, heavy rainfall or other factors, then annual calibrations of InSAR data could be improved for rock slopes on a larger scale, instead of relying on interpolations from linear displacement trends during the snow free months.

Dating methods, like cosmogenic nuclide dating could be applied to investigate the deformation chronology at Dusnjárga. By dating the backscarp at the head domain, local blocks in the central domain and the large scarps found in the transition zone, a general idea of chronology could be established. In the valley north of Dusnjárga called Tverrbotn, there are several large structures that look like parallel faults running down from the backscarp. It would be interesting to figure out if these large faults could be correlated to deformation of the large backscarp at the head domain, which could lead to a better understanding of the relation between the head domain and the active RSD.

The 2D InSAR and 3D InSAR methods used in this thesis to interpret kinematic spatial variations along terrain profiles showed very promising results. It was a good way of interpreting kinematics in large complex areas where the Dips8 method may be too simplified. By comparing InSAR displacement data with mapped morphological structures and simple finite element simulations from (Frattini et al., 2018), most of the slope characteristics of Dusnjárga could be interpreted. InSAR coverage is at its worst in the toe domain of Dusnjárga, where the installation of corner reflectors or additional dGNSS stations could provide better information of the present deformation at the toe.

7 Conclusion

Fieldwork and photogrammetry have been combined to produce geomorphological maps and perform a structural analysis of the rock slope. Both 2D InSAR and 3D InSAR methods have been utilized to document kinematic spatial variations along the rock slope surface. An interpretation of the rupture surface, internal deformation and failure mechanism has then been done by combining displacement data with simple finite element simulations, morphology and measured structures. The following conclusions are derived from the results and interpretations presented in this thesis:

- Based on InSAR and dGNSS measurements, the active RSD of Dusnjárga starts at an elevation of 520 m.a.s.l. and continues down to 100 m.b.s.l., covering an area of ca 1.32 km^2. The most active parts of the RSD are in the upper parts of the slope (central domain), with velocities peaking at 15–20 mm/year, followed by a gradual decrease of velocity down the slope, until it is halved at the toe domain. The head domain shows little to no current displacement, except for a smaller block moving in the range of 7–15 mm/year.

- By comparing 2D InSAR kinematics to analyzed structures, the movement of the slope seems to favor the orientation of foliation. A weakness along foliation was further suggested from strength tests and thin sections, showing anisotropic properties and weak shear zones developed along the foliation. The foliation is affected by both a gentle anticlinal fold and an open synclinal fold, which makes the basal rupture surface irregular. The RSD has increased deformation along both fold hinges, extensional at the anticlinal and compressional at the synclinal, due to the sub-rotational movement caused by the folds.

- The rear rupture surface of the active RSD is joint controlled. The movement vectors are dipping at 50–60°, based on 3D InSAR and 2D InSAR. The dip of the combined 2D displacement vectors gets gradually shallower down-slope until a certain point in the central domain (ca 400 m.a.s.l.), interpreted as the transition between rear and basal rupture surface. Based on simple finite element simulations, the rear rupture surface

follows a roto-translational movement, interpreted to be the result of step-fracturing. The basal rupture seems to have a complex irregular shape as it follows the foliation through a fold system. From the geometry of the rear and basal rupture surfaces, the RSD can be classified as an irregular complex bi-planar compound slide.

- The RSD was likely actively deforming in the time following 7000–8000 BP, based on sediment records and a displaced shoreline, both correlating to the Tapes transgression. The initial start of the deformation remains highly speculative but could correlate to the deglaciation of the area, at around 13–14 ka, based on previous studies.

- Displacement seems to decrease towards the lateral limits of the toe, at least for the middle and eastern parts, creating the toe bulge structure. In the western parts of the toe, there are less morphological features but a higher grade of disintegration, probably related to the less favorable foliation orientation compared to slope orientation. There are frequent morphological depressions in the toe domain, both in the direction of movement and some with an offset of 40–50°, thought to be joint controlled shear fractures, enabling the flow-like bulging structure of the RSD.

- There is evidence of morphological extensional features in the toe, even though the toe domain is currently compressed with a slight upward displacement. This suggests a mature development of the slope, where previous extensional features have been transferred down–slope, adding mass to the compressed toe. The mapped shoreline supports this evolution with morphological signs supporting a downward displacement in the currently compressed toe.

- Results from this thesis highlight the value of combining different methods when interpreting failure mechanisms and kinematics of a rock slope. Although remote data like InSAR, DEMs and aerial photos are great for covering large areas, fieldwork investigations are highly necessary to complement findings and new observations. All methods have their limitations, where one method fails another one might succeed.

References

ABRAMSON, L. W., LEE, T. S., SHARMA, S. & BOYCE, G. M. 2001. *Slope stability and stabilization methods*, John Wiley & Sons.

AGLIARDI, F., CROSTA, G. & ZANCHI, A. 2001. Structural constraints on deep-seated slope deformation kinematics. *Engineering Geology,* 59**,** 83-102.

AGLIARDI, F., CROSTA, G. B. & FRATTINI, P. 2012. 18 Slow rock-slope deformation. *Landslides: Types, mechanisms and modeling***,** 207.

AGLIARDI, F., SCUDERI, M. M., FUSI, N. & COLLETTINI, C. 2020. Slow-to-fast transition of giant creeping rockslides modulated by undrained loading in basal shear zones. *Nature communications,* 11**,** 1-11.

AGUADO, L., O'DRISCOLL, C., XIA, P., NURUTDINOV, K., HILL, C. & O'BEIRNE, P. 2006. A low-cost, low-power Galileo/GPS positioning system for monitoring landslides. *Navitec (October 2006),* 194.

AMBROSI, C. & CROSTA, G. B. 2006. Large sackung along major tectonic features in the Central Italian Alps. *Engineering geology,* 83**,** 183-200.

BERTOLO, D. 2017. A decision support system (DSS) for critical landslides and rockfalls and its application to some cases in the Western Italian Alps. *Natural Hazards and Earth System Sciences Discussions***,** 1-31.

BLAU, F. 2020. *The rock slope failures at Låvan and Dusnjarga, Northern Norway. A comprehensive Quaternary, morphological and structural analysis.* UiT Norges arktiske universitet.

BLIKRA, L. H., BRAATHEN, A., ANDA, E., STALSBERG, K. & LONGVA, O. 2002. Rock avalanches, gravitational bedrock fractures and neotectonic faults onshore northern West Norway: Examples, regional distribution and triggering mechanisms. *Geological Survey of Norway Report*.

BLIKRA, L. H., FASANI, G. B., ESPOSITO, C., LENTI, L., MARTINO, S., PECCI, M., MUGNOZZA, G. S., KALENCHUK, K. S., HUTCHINSON, D. J. & DIEDERICHS, M. 2012. 26 The Aknes rockslide, Norway. *Landslides: types, mechanisms and modeling***,** 323.

BONDEVIK, S., LØDØEN, T. K., TØSSEBRO, C., ÅRSKOG, H., HJELLE, K. L. & MEHL, I. K. 2019. Between winter storm surges–human occupation on a growing Mid-Holocene transgression maximum (Tapes) beach ridge at Longva, Western Norway. *Quaternary Science Reviews,* 215**,** 116-131.

BOVIS, M. J. 1990. Rock-slope deformation at affliction creek, southern Coast Mountains, British Columbia. *Canadian Journal of Earth Sciences,* 27**,** 243-254.

BROWN, J., FERRIANS JR, O., HEGINBOTTOM, J. A. & MELNIKOV, E. 1997. Circum-arctic map of permafrost and ground ice conditions.

BROWN, R. J. E. & KUPSCH, W. O. 1992. Permafrost terminology. *Biuletyn Peryglacjalny,* 32.

BRAATHEN, A., BLIKRA, L. H., BERG, S. S. & KARLSEN, F. 2004. Rock-slope failures in Norway; type, geometry, deformation mechanisms and stability. *Norwegian Journal of Geology/Norsk Geologisk Forening,* 84.

BUNKHOLT, H., REDFIELD, T., OSMUNDSEN, P. T., OPPIKOFER, T., HERMANNS, R. L. & DEHLS, J. 2013. The role of inherited structures in deep seated slope failures in Kåfjorden, Norway. *Landslide science and practice.* Springer.

BÖHME, M., BUNKHOLT, H., OPPIKOFER, T., DEHLS, J., HERMANNS, R., ERIKSEN, H., LAUKNES, T. & EIKEN, T. 2018. Using 2D InSAR, dGNSS and structural field data to understand the deformation mechanism of the unstable rock slope Gamanjunni 3, northern Norway. *Landslides and engineered slopes. Experience, theory and practice.* CRC Press.

BÖHME, M., HERMANNS, R. L., OPPIKOFER, T., FISCHER, L., BUNKHOLT, H. S., EIKEN, T., PEDRAZZINI, A., DERRON, M.-H., JABOYEDOFF, M. & BLIKRA, L. H. 2013. Analyzing complex rock slope deformation at Stampa, western Norway, by integrating geomorphology, kinematics and numerical modeling. *Engineering geology,* 154**,** 116-130.

BÖHME, M., OPPIKOFER, T., LONGVA, O., JABOYEDOFF, M., HERMANNS, R. & DERRON, M.-H. 2015. Analyses of past and present rock slope instabilities in a fjord valley: Implications for hazard estimations. *Geomorphology,* 248**,** 464-474.

BÖHME, M., SAINTOT, A., HENDERSON, I. H., HENRIKSEN, H. & HERMANNS, R. L. 2011. Rock slope instabilities in Sogn and Fjordane County, Norway: a detailed structural and geomorphological analysis. *Geological Society, London, Special Publications,* 351**,** 97-111.

CASCINI, L., FORNARO, G. & PEDUTO, D. 2010. Advanced low-and full-resolution DInSAR map generation for slow-moving landslide analysis at different scales. *Engineering Geology,* 112**,** 29-42.

CLAGUE, J. J. & EVANS, S. G. 1994. *Formation and failure of natural dams in the Canadian Cordillera,* Geological Survey of Canada.

CLAGUE, J. J. & STEAD, D. 2012. *Landslides: types, mechanisms and modeling,* Cambridge University Press.

CLARK, C. D., HUGHES, A. L., GREENWOOD, S. L., JORDAN, C. & SEJRUP, H. P. 2012. Pattern and timing of retreat of the last British-Irish Ice Sheet. *Quaternary Science Reviews,* 44**,** 112-146.

COLESANTI, C. & WASOWSKI, J. 2006. Investigating landslides with space-borne Synthetic Aperture Radar (SAR) interferometry. *Engineering geology,* 88**,** 173-199.

CORNER, G. D. & HAUGANE, E. 1993. Marine-lacustrine stratigraphy of raised coastal basins and postglacial sea-level change at Lyngen and Vanna, Troms, northern Norway. *Norsk Geologisk Tidsskrift,* 73**,** 175-197.

CRIPPA, C., VALBUZZI, E., FRATTINI, P., CROSTA, G. B., SPREAFICO, M. C. & AGLIARDI, F. 2021. Semi-automated regional classification of the style of activity of slow rock-slope deformations using PS InSAR and SqueeSAR velocity data. *Landslides,* 18**,** 2445-2463.

CROSTA, G. & AGLIARDI, F. 2003. Failure forecast for large rock slides by surface displacement measurements. *Canadian Geotechnical Journal,* 40**,** 176-191.

CROSTA, G., FRATTINI, P. & AGLIARDI, F. 2013. Deep seated gravitational slope deformations in the European Alps. *Tectonophysics,* 605**,** 13-33.

CROZIER, M. J. 2010. Deciphering the effect of climate change on landslide activity: A review. *Geomorphology,* 124**,** 260-267.

CRUDEN, D., VARNES, D., TURNER, A. & SCHUSTER, R. 1996. Landslide Types and Processes. Transportation Research Board, National Research Council. National Academy Press Washington DC.

CRUDEN, D. M. 1991. A simple definition of a landslide. *Bulletin of the International Association of Engineering Geology-Bulletin de l'Association Internationale de Géologie de l'Ingénieur,* 43**,** 27-29.

DEHLS, J., FISCHER, L., BÖHME, M., SAINTOT, A., HERMANNS, R., OPPIKOFER, T., LAUKNES, T., LARSEN, Y. & BLIKRA, L. 2012. Landslide monitoring in western Norway using high resolution TerraSAR-X and Radarsat-2 InSAR. *Landslides and Engineered Slopes: Protecting Society through Improved Understanding; Eberhardt, E., Froese, C., Turner, K., Leroueil, S., Eds***,** 1321-1325.

DEL SOLDATO, M., SOLARI, L., RASPINI, F., BIANCHINI, S., CIAMPALINI, A., MONTALTI, R., FERRETTI, A., PELLEGRINESCHI, V. & CASAGLI, N. 2019. Monitoring ground instabilities using SAR satellite data: A practical approach. *ISPRS International Journal of Geo-Information,* 8**,** 307.

DRONEDEPLOY. 2021. *DroneDeploy* [Online]. Available: https://www.dronedeploy.com/ [Accessed 1. October 2021].

EBERHARDT, E., WATSON, A. & LOEW, S. 2008. Improving the interpretation of slope monitoring and early warning data through better understanding of complex deep-seated landslide failure mechanisms. *Landslides and Engineered Slopes. From the Past to the Future, Two Volumes+ CD-ROM***,** 61-74.

ERIKSEN, H. Ø., BERGH, S. G., LARSEN, Y., SKREDE, I., KRISTENSEN, L., LAUKNES, T. R., BLIKRA, L. H. & KIERULF, H. P. 2017. Relating 3D surface displacement from satellite-and ground-based InSAR to structures and geomorphology of the Jettan rockslide, northern Norway.

EVANS, D. J., REA, B. R., HANSOM, J. D. & WHALLEY, W. B. 2002. Geomorphology and style of plateau icefield deglaciation in fjord terrains: the example of Troms ‐ Finnmark, north Norway. *Journal of Quaternary Science: Published for the Quaternary Research Association,* 17**,** 221-239.

EVANS, S. G. & CLAGUE, J. J. 1994. Recent climatic change and catastrophic geomorphic processes in mountain environments. *Geomorphology and Natural Hazards.* Elsevier.

EVANS, S. G., DELANEY, K. B., HERMANNS, R. L., STROM, A. & SCARASCIA-MUGNOZZA, G. 2011. The formation and behaviour of natural and artificial rockslide dams; implications for engineering performance and hazard management. *Natural and artificial rockslide dams.* Springer.

FARBROT, H., ISAKSEN, K., ETZELMÜLLER, B. & GISNÅS, K. 2013. Ground thermal regime and permafrost distribution under a changing climate in northern Norway. *Permafrost and Periglacial Processes,* 24**,** 20-38.

FRATTINI, P., CROSTA, G. B., ROSSINI, M. & ALLIEVI, J. 2018. Activity and kinematic behaviour of deep-seated landslides from PS-InSAR displacement rate measurements. *Landslides,* 15**,** 1053-1070.

FREDIN, O., BERGSTRØM, B., EILERTSEN, R., HANSEN, L., LONGVA, O., NESJE, A. & SVEIAN, H. 2013. Glacial landforms and Quaternary landscape development in Norway. *Quaternary Geology of Norway, edited by: Olsen, L., Fredin, O., and Olesen, O., Geological Survey of Norway Special Publication, Geological Survey of Norway, Trondheim,* 525.

FREDIN, O. & FOLLESTAD, B. 2011. Geometry and vertical extent of the late Weichselian ice sheet in northwestern Oppland County, Norway.

FURSETH, A. 2006. *Skredulykker i norge,* Tun.

GISNÅS, K., ETZELMÜLLER, B., LUSSANA, C., HJORT, J., SANNEL, A. B. K., ISAKSEN, K., WESTERMANN, S., KUHRY, P., CHRISTIANSEN, H. H. & FRAMPTON, A. 2017. Permafrost map for Norway, Sweden and Finland. *Permafrost and periglacial processes,* 28**,** 359-378.

GLASTONBURY, J. & FELL, R. 2000. *Report on the analysis of" rapid" natural rock slope failures*, University of New South Wales, School of Civil and Environmental Engineering.

GLASTONBURY, J. & FELL, R. 2010. Geotechnical characteristics of large rapid rock slides. *Canadian geotechnical journal,* 47**,** 116-132.

GRIFFITHS, D. & LANE, P. 1999. Slope stability analysis by finite elements. *Geotechnique,* 49**,** 387-403.

GRUBER, S. & HAEBERLI, W. 2007. Permafrost in steep bedrock slopes and its temperature‐related destabilization following climate change. *Journal of Geophysical Research: Earth Surface,* 112.

HANSEN, A. 1900. Skandinaviens stigning. *Vorges Geol. Under sakelse*.

HANSSEN-BAUER, I., DRANGE, H., FØRLAND, E., ROALD, L., BØRSHEIM, K., HISDAL, H., LAWRENCE, D., NESJE, A., SANDVEN, S. & SORTEBERG, A. 2009. Climate in Norway 2100. *Background information to NOU Climate adaptation (In Norwegian: Klima i Norge 2100. Bakgrunnsmateriale til NOU Klimatilplassing), Oslo: Norsk klimasenter*.

HEIM, A. 1932. Landslides and human lives (Bergsturz und Menschenleben). *Bi-Tech Publishers, Vancouver, BC***,** 196.

HENDERSON, I. H. & SAINTOT, A. 2011. Regional spatial variations in rockslide distribution from structural geology ranking: an example from Storfjorden, western Norway. *Geological Society, London, Special Publications,* 351**,** 79-95.

HERMANNS, R., HANSEN, L., SLETTEN, K., BÖHME, M., BUNKHOLT, H., DEHLS, J., EILERTSEN, R., FISCHER, L., L'HEUREUX, J. & HØGAAS, F. 2012a. Systematic geological mapping for landslide understanding in the Norwegian context. *Landslide and engineered slopes: protecting society through improved understanding. Taylor & Francis Group, London***,** 265-271.

HERMANNS, R. L., BLIKRA, L. H., ANDA, E., SAINTOT, A., DAHLE, H., OPPIKOFER, T., FISCHER, L., BUNKHOLT, H., BÖHME, M. & DEHLS, J. F. 2013. Systematic mapping of large unstable rock slopes in Norway. *Landslide science and practice.* Springer.

HERMANNS, R. L., FISCHER, L., OPPIKOFER, T., BØHME, M., DEHLS, J. F., HENRIKSEN, H., BOOTH, A. M., EILERTSEN, R., LONGVA, O. & EIKEN, T. 2011. Mapping of Unstable and Potentially Unstable Slopes in Sogne og Fjordane.

HERMANNS, R. L. & LONGVA, O. 2012. Rapid rock-slope failures. *Landslides: types, mechanisms and modeling***,** 59-70.

HERMANNS, R. L., OPPIKOFER, T., ANDA, E., BLIKRA, L., BÖHME, M., BUNKHOLT, H., CROSTA, G., DAHLE, H., DEVOLI, G. & FISCHER, L. 2012b. Recommended hazard and risk classification system for large unstable rock slopes in Norway. *NGU rapport***,** 0800-3416.

HERMANNS, R. L., SCHLEIER, M., BÖHME, M., BLIKRA, L. H., GOSSE, J., IVY-OCHS, S. & HILGER, P. Rock-avalanche activity in W and S Norway peaks after the retreat

of the Scandinavian Ice Sheet. Workshop on World Landslide Forum, 2017. Springer, 331-338.
HILGER, P., HERMANNS, R. L., CZEKIRDA, J., MYHRA, K. S., GOSSE, J. C. & ETZELMÜLLER, B. 2021. Permafrost as a first order control on long-term rock-slope deformation in (Sub-) Arctic Norway. *Quaternary Science Reviews,* 251**,** 106718.
HUGGEL, C., ALLEN, S., DELINE, P., FISCHER, L., NOETZLI, J. & RAVANEL, L. 2012. Ice thawing, mountains falling—are alpine rock slope failures increasing? *Geology Today,* 28**,** 98-104.
HUGHES, A. L., GYLLENCREUTZ, R., LOHNE, Ø. S., MANGERUD, J. & SVENDSEN, J. I. 2016. The last Eurasian ice sheets‐a chronological database and time‐slice reconstruction, DATED‐1. *Boreas,* 45**,** 1-45.
HUNGR, O., LEROUEIL, S. & PICARELLI, L. 2014. The Varnes classification of landslide types, an update. *Landslides,* 11**,** 167-194.
HUTCHINSON, J. H. General report, morphological and geotechnical parameters of landslides in relation to geology and hydrogeology. Landslides, Proceedings of the Fifth International Symposium on Landslides, 1988, 1988.
ISHIBASHI, I. & HAZARIKA, H. 2015. *Soil mechanics fundamentals and applications,* CRC Press.
KARTVERKET. 2014. *Norgeskart Stadnamn* [Online]. Available: http://norgeskart.no/ssr/ [Accessed February 7, 2022].
KARTVERKET. 2015. *Finnmark 2015* [Online]. Available: http://www.norgeibilder.no/?id=1861 [Accessed February 7, 2022].
KARTVERKET. 2021. *1 m Digital Terrain Model* [Online]. Available: https://hoydedata.no/LaserInnsyn/ [Accessed 01. October 2021].
KLEMAN, J. 1992. The palimpsest glacial landscape in northwestern Sweden: Late Weichselian deglaciation landforms and traces of older west-centered ice sheets. *Geografiska Annaler: Series A, Physical Geography,* 74**,** 305-325.
KLEMAN, J., HÄTTESTRAND, C., BORGSTRÖM, I. & STROEVEN, A. 1997. Fennoscandian palaeoglaciology reconstructed using a glacial geological inversion model. *Journal of glaciology,* 43**,** 283-299.
KRAUSKOPF, K. B. 1954. Igneous and metamorphic rocks of the Øksfjord area, Vest-Finnmark. Eruptive og metamorfe bergarter i Øksfjordområdet, Vest-Finnmark.
KRAUTBLATTER, M., FUNK, D. & GÜNZEL, F. K. 2013. Why permafrost rocks become unstable: a rock‐ice‐mechanical model in time and space. *Earth Surface Processes and Landforms,* 38**,** 876-887.
KRISTENSEN, L., CZEKIRDA, J., PENNA, I., ETZELMÜLLER, B., NICOLET, P., PULLARELLO, J. S., BLIKRA, L. H., SKREDE, I., OLDANI, S. & ABELLAN, A. 2021. Movements, failure and climatic control of the Veslemannen rockslide, Western Norway. *Landslides,* 18**,** 1963-1980.
KVERNDAL, A.-I. & SOLLID, J. L. 1993. Late Weichselian glaciation and deglaciation in northeastern Troms, northern Norway.
LAUKNES, T. R. 2011. Rockslide mapping in Norway by means of interferometric SAR time series analysis.
LAUKNES, T. R., GRAHN, J., ROYET, L., LARSEN, Y., BÖHME, M., DEHLS, J. F. & KRISTIANSEN, L. 2020. Mapping and characterization of unstable slopes with Sentinel-1 multi-geometry InSAR (activity line 2: public sector applications).

LEROUEIL, S., LOCAT, J., VAUNAT, J., PICARELLI, L. & LEE, H. Geotechnical characterization of slope movements. Landslides, 1996. 53-74.
LIMITED, P. E. 2021. Clino Fieldmove. 2.5.19. ed.
MAGNIN, F., ETZELMÜLLER, B., WESTERMANN, S., ISAKSEN, K., HILGER, P. & HERMANNS, R. L. 2019. Permafrost distribution in steep rock slopes in Norway: measurements, statistical modelling and implications for geomorphological processes. *Earth Surface Dynamics,* 7**,** 1019-1040.
MARTHINUSSEN, M. 1960. Coast and fjord area of Finnmark. *Geology of Norway,* 208**,** 416-429.
MCCOLL, S. T. 2012. Paraglacial rock-slope stability. *Geomorphology,* 153**,** 1-16.
METEOROLOGISK INSTITUTT, N. V.-O. E. N., NORWEGIAN RESEARCH CENTER AS NORCE, AND BJERKNES CENTER FOR CLIMATE RESEARCH,. 2021a. *Klimaframskrivninger* [Online]. Available: https://klimaservicesenter.no/climateprojections?index=precipitation_amount&period=Annual&scenario=RCP85&area=C19# [Accessed February 8, 2022].
METEOROLOGISK INSTITUTT, N. V.-O. E. N., NORWEGIAN RESEARCH CENTER AS NORCE, AND BJERKNES CENTER FOR CLIMATE RESEARCH,. 2021b. *Klimaprofil Troms* [Online]. Available: https://klimaservicesenter.no/kss/klimaprofiler/troms [Accessed February 8, 2022].
METEROLOGISK INSTITUTT. 2022. *Observasjoner og værstatistikk* [Online]. Available: https://seklima.met.no/observations/ [Accessed February 8, 2022].
MOORE, J. R., GISCHIG, V., KATTERBACH, M. & LOEW, S. 2011. Air circulation in deep fractures and the temperature field of an alpine rock slope. *Earth Surface Processes and Landforms,* 36**,** 1985-1996.
MØLLER, J. J. 1987. Shoreline relation and prehistoric settlement in northern Norway.
MØRK, M. & STABEL, A. 1990. Cambrian Sm-Nd dates for an ultramafic intrusion and for high-grade metamorphism on the Øksfjord peninsula, Finnmark, North Norway. *Norsk Geologisk Tidsskrift,* 70**,** 275-291.
NABAVI, S. T. & FOSSEN, H. 2021. Fold geometry and folding–a review. *Earth-Science Reviews,* 222**,** 103812.
NGU. 2017. *LØSMASSER N50/N250* [Online]. Available: https://geo.ngu.no/kart/minkommune/?kommunenr=5429 [Accessed 16. October 2021].
NGU. 2018. *InSAR Norway* [Online]. Available: https://insar.ngu.no/ [Accessed 2. September 2021].
NGU. 2019. *InSAR Norway - About the mapping service* [Online]. NGU. Available: https://www.ngu.no/en/topic/about-mapping-service [Accessed 10. March 2022].
NGU. 2020a. *Bedrock and structural measurements* [Online]. NGU. Available: https://geo.ngu.no/kart/berggrunn_mobil/ [Accessed 01. October 2021].
NGU. 2020b. *BERGGRUNN N250* [Online]. NGU. Available: http://geo.ngu.no/kart/berggrunn_mobil/ [Accessed 16. September 2021].
NGU. 2022a. *Unstable Rock Slope inventory map* [Online]. Available: www.ngu.no [Accessed 01. October 2021].
NGU. 2022b. *Unstable Rock Slopes - National Database for Unstable Rock Slopes* [Online]. NGU. Available: https://geo.ngu.no/kart/ustabilefjellparti_mobil/?lang=eng [Accessed 4. December 2021].

NITHIARASU, P., TAYLOR, R., ZHU, J. & ZIENKIEWICZ, O. 1977. The finite element method, Vol. 3. McGraw-hill, London.
NÄSLUND, J., RODHE, L., FASTOOK, J. & HOLMLUND, P. 2003. New ways of studying ice sheet flow directions and glacial erosion by computer modelling—examples from Fennoscandia. *Quaternary Science Reviews,* 22**,** 245-258.
OPPIKOFER, T., EIKEN, T., DAHLE, H., ANDA, E., HERMANNS, R., OTTERÅ, S. & SAINTOT, A. 2013. Investigations on unstable rock slopes in Møre og Romsdal-status and plans after field surveys in 2012.
PASTORE, Z., FICHLER, C. & MCENROE, S. 2018. Magnetic anomalies of the mafic/ultramafic Seiland Igneous Province.
PASTORE, Z., FICHLER, C. & MCENROE, S. A. 2016. The deep crustal structure of the mafic–ultramafic Seiland Igneous Province of Norway from 3-D gravity modelling and geological implications. *Geophysical Supplements to the Monthly Notices of the Royal Astronomical Society,* 207**,** 1653-1666.
PENNA, I. M., BÖHME, M., HERMANNS, R., EIKEN, T. & DEHLS, J. Large-Scale Rockslope Deformations in Sogn Og Fjordane County (Norway). Workshop on World Landslide Forum, 2017. Springer, 601-606.
RADBRUCH-HALL, D., VARNES, D. & SAVAGE, W. 1976. Gravitational spreading of steep-sided ridges ("sackung") in Western United States. *Bulletin of the International Association of Engineering Geology-Bulletin de l'Association Internationale de Géologie de l'Ingénieur,* 13**,** 23-35.
REDFIELD, T., HERMANNS, R., EIKEN, T., L'HEUREUX, J.-S., BUNKHOLT, H., OSMUNDSEN, P. T., OPPIKOFER, T. & LAUKNES, R. R. 2011. ROS fjellskred i Troms: status og analyser etter feltarbeid 2010.
RIVA, F., AGLIARDI, F., AMITRANO, D. & CROSTA, G. B. 2018. Damage‐based time‐dependent modeling of paraglacial to postglacial progressive failure of large rock slopes. *Journal of Geophysical Research: Earth Surface,* 123**,** 124-141.
ROBERTS, D. & ELVEVOLD, S. 2018. Berggrunnskart Øksfjord 1835-3 M 1: 50 000.
ROBERTS, D. & LIPPARD, S. J. 2005. Inferred Mesozoic faulting in Finnmark: current status and offshore links.
ROBERTS, R., CORFU, F., TORSVIK, T., ASHWAL, L. & RAMSAY, D. 2006. Short-lived mafic magmatism at 560–570 Ma in the northern Norwegian Caledonides: U–Pb zircon ages from the Seiland Igneous Province. *Geological Magazine,* 143**,** 887-903.
ROBERTS, R. J., CORFU, F., TORSVIK, T. H., HETHERINGTON, C. & ASHWAL, L. D. 2010. Age of alkaline rocks in the Seiland igneous province, northern Norway. *Journal of the Geological Society,* 167**,** 71-81.
ROMUNDSET, A., AKÇAR, N., FREDIN, O., TIKHOMIROV, D., REBER, R., VOCKENHUBER, C., CHRISTL, M. & SCHLÜCHTER, C. 2017. Lateglacial retreat chronology of the Scandinavian Ice Sheet in Finnmark, northern Norway, reconstructed from surface exposure dating of major end moraines. *Quaternary science reviews,* 177**,** 130-144.
ROTH, M. & BLIKRA, L. 2005. *Seismic monitoring of the unstable rock slope at Åknes, Norway,* na.
ROTT, H., SCHEUCHL, B., SIEGEL, A. & GRASEMANN, B. 1999. Monitoring very slow slope movements by means of SAR interferometry: A case study from a mass waste

above a reservoir in the Ötztal Alps, Austria. *Geophysical Research Letters,* 26**,** 1629-1632.
ROUYET, L., LAUKNES, T. R., CHRISTIANSEN, H. H., STRAND, S. M. & LARSEN, Y. 2019. Seasonal dynamics of a permafrost landscape, Adventdalen, Svalbard, investigated by InSAR. *Remote Sensing of Environment,* 231**,** 111236.
SAINTOT, A., HENDERSON, I. & DERRON, M.-H. 2011. Inheritance of ductile and brittle structures in the development of large rock slope instabilities: examples from western Norway. *Geological Society, London, Special Publications,* 351**,** 27-78.
SANDBAKKEN, H. 2021. *Characterizing slope processes along the Piggtind mountain ridge, using 2D InSAR.* UiT Norges arktiske universitet.
SCHLÖGEL, R., MALET, J.-P., DOUBRE, C. & LEBOURG, T. 2016. Structural control on the kinematics of the deep-seated La Clapière landslide revealed by L-band InSAR observations. *Landslides,* 13**,** 1005-1018.
SEEBER, G. 2003. Satellite Geodesy: Foundations, Methods and Applications. *INTERNATIONAL HYDROGRAPHIC REVIEW,* 4**,** 92-93.
SINGH, B. & GOEL, R. 2011. *Engineering rock mass classification*, Elsevier.
SOLDATI, M. 2013. Deep-seated Gravitational Slope Deformation. *In:* BOBROWSKY, P. T. (ed.) *Encyclopedia of Natural Hazards.* Dordrecht: Springer Netherlands.
SOLLID, J., ANDERSEN, S., HAMRE, N., KJELDSEN, O., SALVIGSEN, O., STURØD, S., TVEITÅ, T. & WILHELMSEN, A. 1973. Deglaciation of Finnmark, North Norway. *Norsk Geografisk Tidsskrift-Norwegian Journal of Geography,* 27**,** 233-325.
SONGBO, W., YONGYAO, L., LEI, Z. & XIAOLI, D. 2020. Multi-temporal InSAR for urban deformation monitoring: Progress and challenges. *雷达学报,* 9**,** 277-294.
STEAD, D. & EBERHARDT, E. 2013. Understanding the mechanics of large landslides. *Ital. J. Eng. Geol. Environ. Book Ser,* 6**,** 85-112.
STEAD, D., EBERHARDT, E. & COGGAN, J. 2006. Developments in the characterization of complex rock slope deformation and failure using numerical modelling techniques. *Engineering geology,* 83**,** 217-235.
STEAD, D. & WOLTER, A. 2015. A critical review of rock slope failure mechanisms: the importance of structural geology. *Journal of Structural Geology,* 74**,** 1-23.
STEAD, D., WOLTER, A. & CLAGUE, J. A Critical Review of Landslide Failure Mechanisms. AGU Fall Meeting Abstracts, 2011. NH11B-03.
STORE NORSKE LEKSIKON. 2009. *Burfjord* [Online]. Available: https://snl.no/Burfjord [Accessed February 8, 2022].
SVENDSEN, J. I., ALEXANDERSON, H., ASTAKHOV, V. I., DEMIDOV, I., DOWDESWELL, J. A., FUNDER, S., GATAULLIN, V., HENRIKSEN, M., HJORT, C. & HOUMARK-NIELSEN, M. 2004. Late Quaternary ice sheet history of northern Eurasia. *Quaternary Science Reviews,* 23**,** 1229-1271.
TANNER, V. 1915. *Studier öfver kvartärsystemet i Fennoskandias nordliga delar*.
TAPPIN, D. 2010. Mass transport events and their tsunami hazard. *Submarine mass movements and their consequences.* Springer.
VARNES, D. J. 1978. Slope movement types and processes. *Special report,* 176**,** 11-33.
VICK, L. M., BÖHME, M., ROUYET, L., BERGH, S. G., CORNER, G. D. & LAUKNES, T. R. 2020. Structurally controlled rock slope deformation in northern Norway. *Landslides,* 17**,** 1745-1776.

WASOWSKI, J. & BOVENGA, F. 2014. Investigating landslides and unstable slopes with satellite Multi Temporal Interferometry: Current issues and future perspectives. *Engineering Geology*, 174**,** 103-138.
WELKNER, D., EBERHARDT, E. & HERMANNS, R. 2010. Hazard investigation of the Portillo Rock Avalanche site, central Andes, Chile, using an integrated field mapping and numerical modelling approach. *Engineering Geology*, 114**,** 278-297.
ZHONGMING, Z., LINONG, L., XIAONA, Y., WANGQIANG, Z. & WEI, L. 2013. Climate change 2013: The physical science basis.
ZISCHINSKY, U. On the deformation of high slopes. 1st ISRM Congress, 1966. OnePetro.

Appendix

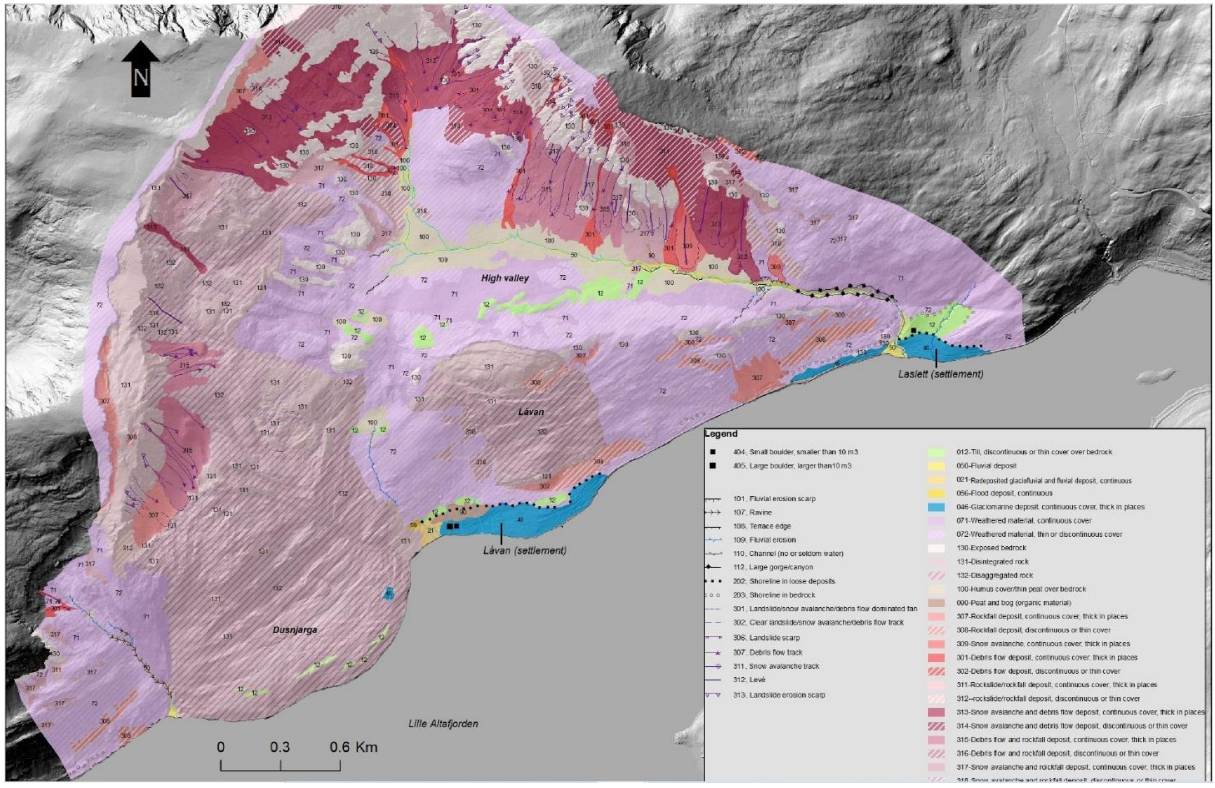

Appendix 1: Quaternary map of Dusnjárga, Låvan and the high valley to the north. Scale 1:20000. Source: (Blau, 2020)

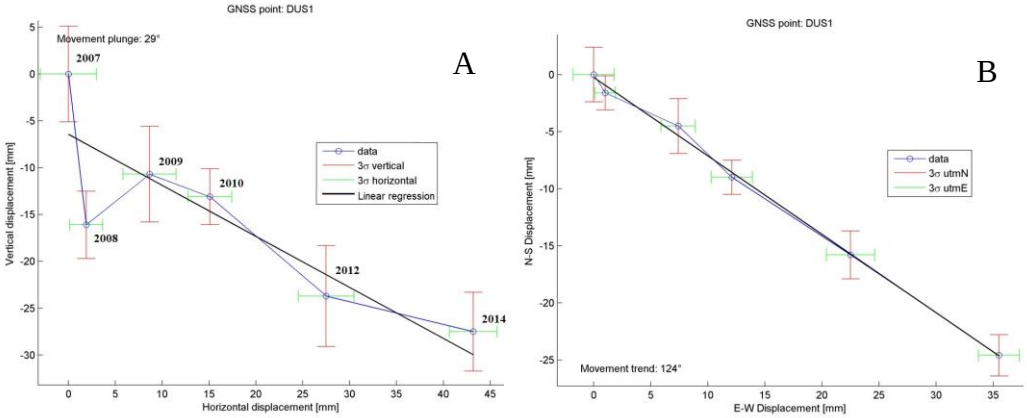

Appendix 2: A: Shows horizontal displacement (mm) on the x-axis and vertical displacement (mm) on the y-axis. Each point has a vertical and horizontal uncertainty, marked red and green respectively. A linear regression line has been drawn between the points which gives a movement plunge of 29 degrees. B: A graph depicting the horizontal deformation of this dGNSS point, in a N-S and E-W orientation, showing its movement trend of 124 degrees north. Uncertainties of N-S (red) displacement and E-W (green) are also depicted.

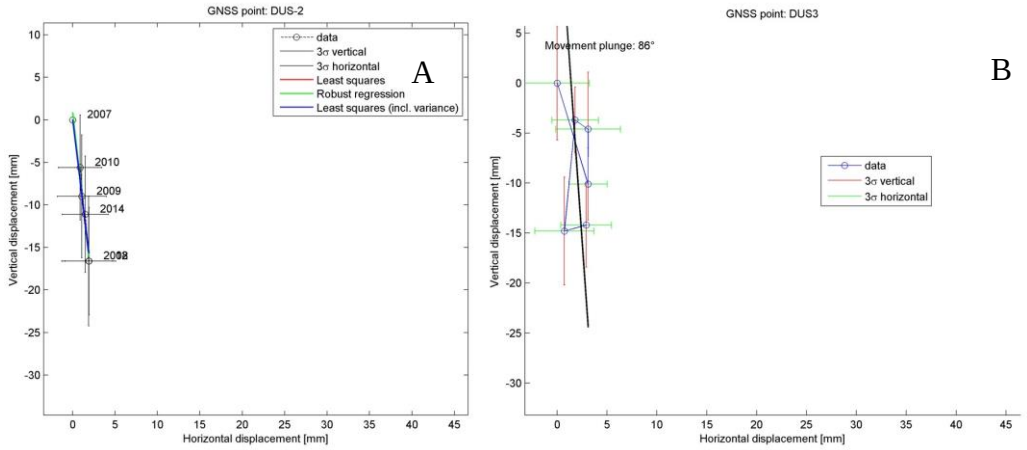

*Appendix 3: A: Graph displaying vertical and horizontal displacement (mm) for **DUSN_GPS_02**. Shows a trend of vertical movement down-slope, but with a very small annual movement. B: Graph showing vertical and horizontal displacement (mm) for **DUSN_GPS_03.***

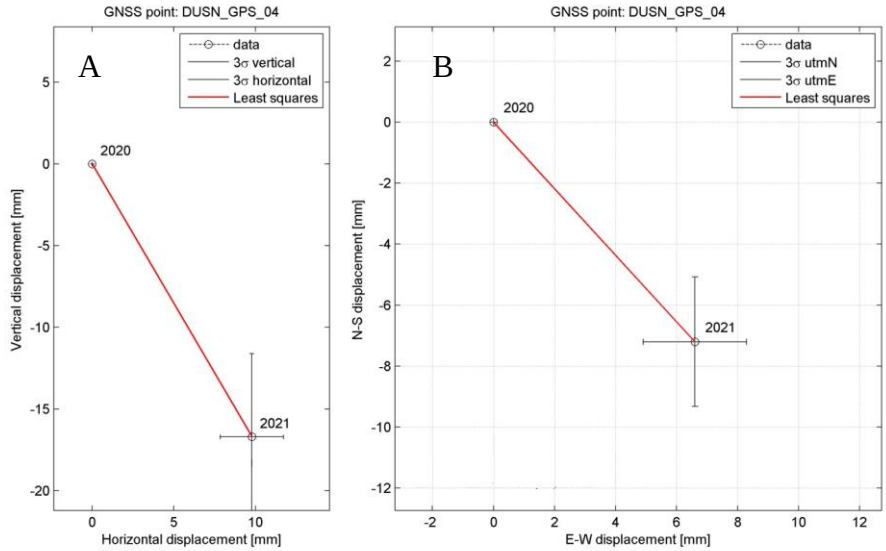

*Appendix 4: A: Vertical and horizontal displacement (mm) at location **DUSN_GPS_04**. B: Horizontal displacement for both N-S and E-W orientations. Displacement oriented to the southeast, 137 degrees north. Measured displacement far exceeds uncertainty for both graphs.*

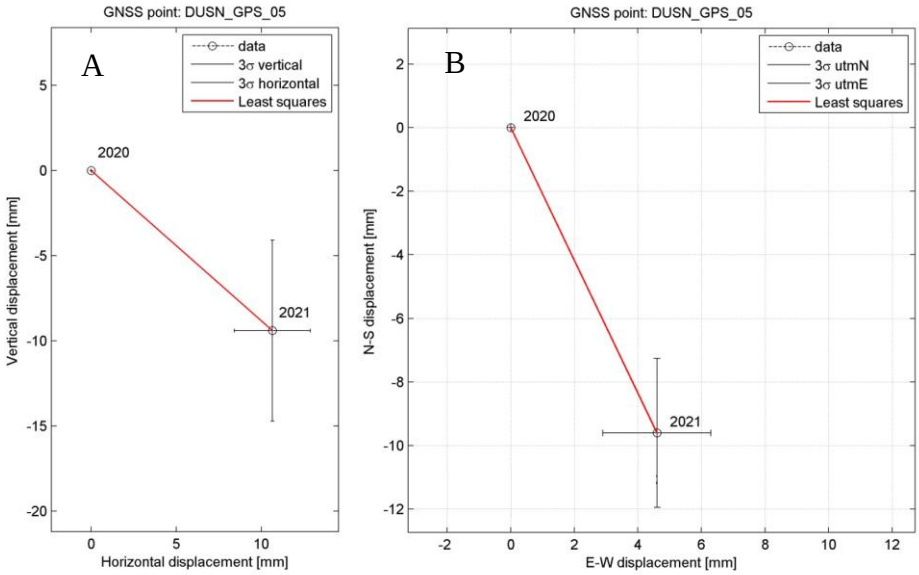

*Appendix 5: Location **DUSN_GPS_05** with vertical and horizontal displacements exceeding the uncertainty. A: Displaying vertical and horizontal displacement (mm) for this location. B: Displays the horizontal displacement in both N-S and E-W directions to visualize combined horizontal orientation.*

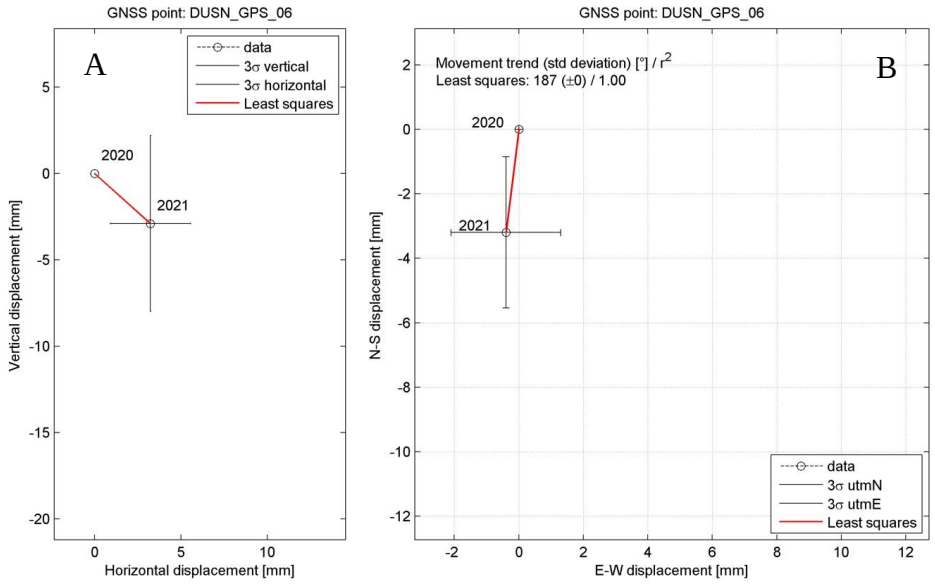

Appendix 6: A: Vertical and horizontal displacement graph, showing very little movement. B: Horizontal displacement graph showing some small movement towards the south, while displacement rates along other axis falls short of uncertainty.

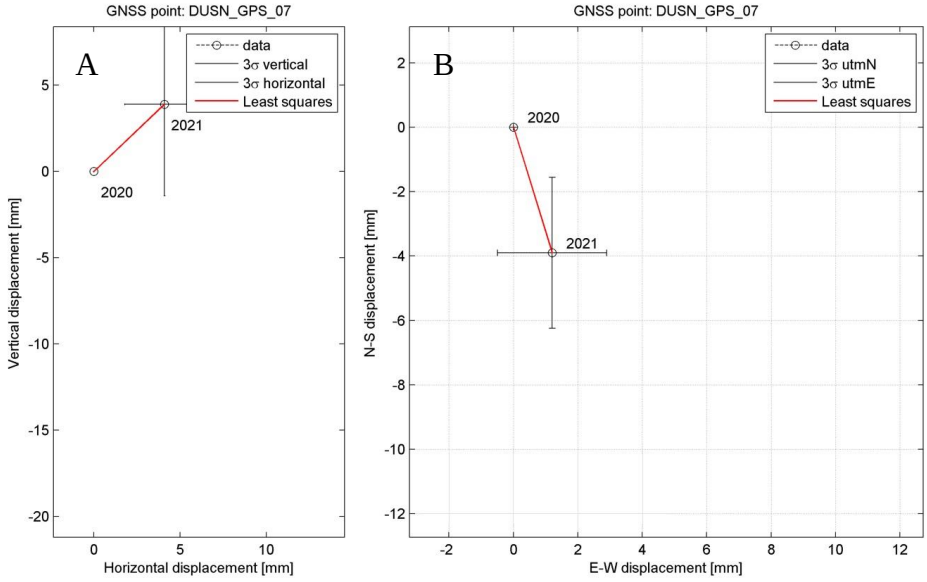

Appendix 7: A: Vertical and horizontal displacement-axis. B: Horizontal displacement where only displacement in the south direction is exceeding the uncertainty.

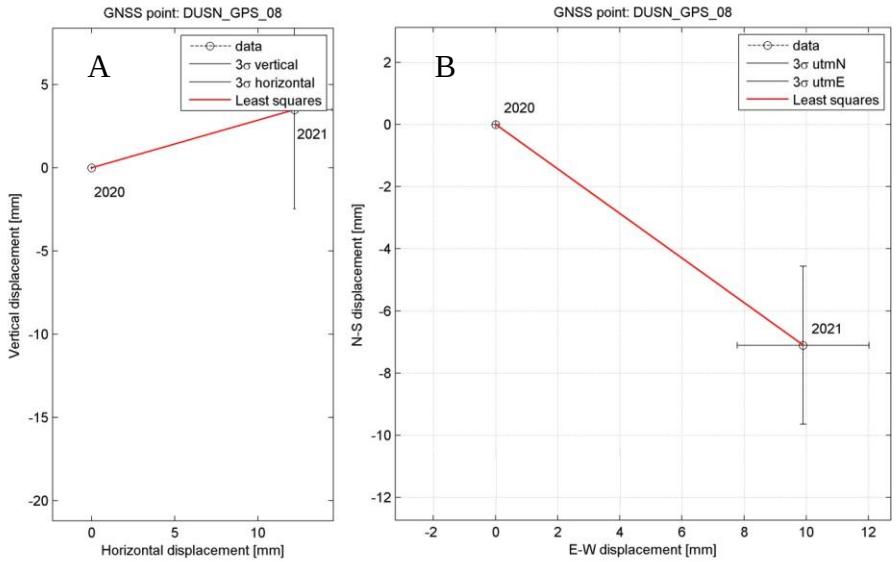

Appendix 8: A: Vertical and horizontal axis displaying annual displacement (mm). Uncertainty of vertical axis is larger than the measured vertical displacement. B: Horizontal displacement graph for the location, depicting displacement in N-S and E-W axis, where measurements are greater than the uncertainty for both axes.

Distance	Type	Dip	Dip/D	Length	Ends	Spacing	Water	Rough	Infill	Thick	ILA	λ	Litho	Strength	Comments
Distance	Type	Dip	Dip/D	Length	Ends	Spacing	Water	Rough	Infill	Thick	ILA	λ	Litho	Strength	Comments
0	JN	78	335	145		F	0	3	KL	3	4		MG	R5	coarse gneis, mg-made
8	JN	78	80	20		D	0	2	KL	1	6		MG	R5	coarse gneis, mg-made
20	JN	76	63	25		C	0	3	KL	1	0,3		MG	R5	coarse gneis, mg-made
51	JN	72	76	70		C	0	2	KL	3	2		MG	R5	coarse gneis, mg-made
94	JN	80	60	7		B	0	2	KL	1	0,2		MG	R5	coarse gneis, mg-made
110	JN	72	59	70		B	0	2	KL	2	2		MG	R5	coarse gneis, mg-made
110	CN	72	59	40			0	3	KL	150	2		MG	R5	magm.fine grained lense.
180	JN	72	66	40		C	0	3	KL	20	10		MG	R5	coarse gneis, mg-made
200	JN	43	302	35		C	0	3	KL	20	15		MG	R5	coarse gneis, mg-made
210	JN	34	298	25		A	0	2	KL	1	0		MG	R5	coarse gneis, mg-made
222	JN	27	300	35		A	0	3	KL	1	0		MG	R5	coarse gneis, mg-made
228	JN	66	95	10		C	0	3	KL	55	3		MG	R5	coarse gneis, mg-made
250	JN	63	68	15		A	0	2	KL				MG	R5	coarse gneis, mg-made
253	JN	64	77	8			0	2	KL	1			MG	R5	coarse gneis, mg-made
261	JN	60	76	5		G	0	2	KL	1	2		MG	R5	coarse gneis, mg-made
300	JN	22	257	10		B	0	3	KL		30		MG	R5	coarse gneis, mg-made

Appendix 9: Data from scanline 1.

Distance	Type	Dip	Dip/D	Length	Ends	Spacing	Water	Rough	Infill	Thick	ILA	λ	Litho	Strength	Comments
Distance	Type	Dip	Dip/D	Length	Ends	Spacing	Water	Rough	Infill	Thick	ILA	λ	Litho	Strength	Comments
15	JN	89	347	60		H	2	2	KL	20	50		MG	R5	Well foliated, felsic metagabbro
22	JN	83	58	4		A	2	2	KL	2	0		MG	R5	Well foliated, felsic metagabbro
23	JN	83	58	5		A	2	2	KL	2	0		MG	R5	Well foliated, felsic metagabbro
34	JN	85	180	10		A	2	2	KL	1	0		MG	R5	Well foliated, felsic metagabbro
50	JN	59	347	40		A	2	3	KL		0,5		MG	R5	Well foliated, felsic metagabbro
70	JN	41	193	5		A	2	2	KL	2	2		MG	R5	Well foliated, felsic metagabbro
80	JN	41	193	35		A	2	2	KL	2	2		MG	R5	Well foliated, felsic metagabbro
110	JN	77	351	30		F	2	2	KL	2	10		MG	R5	Well foliated, felsic metagabbro
124	JN	77	344	30		F	2	2	KL	10	10		MG	R5	Well foliated, felsic metagabbro
134	JN	88	344	40		F	2	2	KL	2			MG	R5	Well foliated, felsic metagabbro
150	JN	84	351	20		A	2	2	KL	1			MG	R5	Well foliated, felsic metagabbro
155	JN	72	178	60		E	2	2	KL	2	30		MG	R5	Well foliated, felsic metagabbro
160	JN	68	190	45		E	2	2	KL	20	30		MG	R5	Well foliated, felsic metagabbro
190	JN	72	356	50		F	2	3	KL	2	5		MG	R5	Well foliated, felsic metagabbro
196	JN	88	184	25		D	2	2	KL	1	4		MG	R5	Well foliated, felsic metagabbro
216	JN	83	181	10		C	2	2	KL	1	4		MG	R5	Well foliated, felsic metagabbro
228	JN	76	180	150		I	2	2	KL	15	30		MG	R5	Well foliated, felsic metagabbro
242	JN	89	180	10		A	2	2	KL	1	0		MG	R5	Well foliated, felsic metagabbro
262	JN	77	192	50		H	2	2	KL	10	1		MG	R5	Well foliated, felsic metagabbro
285	JN	87	163	70		A	2	2	KL	2			MG	R5	Well foliated, felsic metagabbro
312	JN	87	330	30		D	2	3	KL	5	0,5		MG	R5	Well foliated, felsic metagabbro
323	JN	36	319	2		B	2	3	KL		1		MG	R5	Well foliated, felsic metagabbro
392	JN	63	166	40		H	2	3	KL		1,5		MG	R5	Well foliated, felsic metagabbro
512	JN	78	348	80		G	2	4	KL		2		MG	R5	Well foliated, felsic metagabbro
520	JN	10	343	150		A	2	2	KL	1			MG	R5	Well foliated, felsic metagabbro
624	JN	51	182	50		B	2	3	KL	2	2		MG	R5	Well foliated, felsic metagabbro

Appendix 10: Data from scanline 2.

Distance	Type	Dip	Dip/D	Length	Ends	Spacing	Water	Rough	Infill	Thick	ILA	λ	Litho	Strength	Comments
Distance	Type	Dip	Dip/D	Length	Ends	Spacing	Water	Rough	Infill	Thick	ILA	λ	Litho	Strength	Comments
15	JN	69	118	5		A	2	3	KL	1	A	0	Mylonite	R5	Mafic mylonite
32	JN	77	118	60		D	2	3	KL	0	L	300	Mylonite	R5	Mafic mylonite
45	JN	88	110	50		D	2	4	KL	0	G	50	Mylonite	R5	Mafic mylonite
55	JN	88	295	7		A	2	4	KL	0	A	0	Mylonite	R5	Mafic mylonite
58	JN	73	120	10		A	2	4	KL	0	A	0	Mylonite	R5	Mafic mylonite
72	JN	88	117	50		G	2	4	KL	0	L	400	Mylonite	R5	Mafic mylonite
79	JN	79	104	25		D	2	3	KL	2	G	50	Mylonite	R5	Mafic mylonite
98	JN	78	121	50		G	2	3	KL	0	I	100	Mylonite	R5	Mafic mylonite
113	JN	81	118	20		D	2	4	KL	1	G	40	Mylonite	R5	Mafic mylonite
119	JN	75	123	40		D	2	4	KL	1	G	50	Mylonite	R5	Mafic mylonite
121	JN	87	127	10		D	2	4	KL	1	G	50	Mylonite	R5	Mafic mylonite
123	JN	89	126	12		D	2	4	KL	1	G	50	Mylonite	R5	Mafic mylonite
160	JN	88	115	35		F	2	4	KL	3	E	15	Mylonite	R5	Mafic mylonite
168	JN	66	286	30		G	2	3	KL	10	E	10	Mylonite	R5	Mafic mylonite
240	JN	89	279	200		K	2	5	KL	40	G	40	Mylonite	R5	Mafic mylonite
253	JN	89	279	10		D	2	5	KL	10	D	10	Mylonite	R5	Mafic mylonite
270	JN	89	279	40		H	2	5	KL	10	D	10	Mylonite	R5	Mafic mylonite
287	JN	58	106	100		G	2	5	KL	40	G	40	Mylonite	R5	Mafic mylonite
310	JN	58	106	50		H	2	5	KL	10	D	10	Mylonite	R5	Mafic mylonite

Appendix 11: Data from scanline 3.

Distance	Type	Dip	Dip/D	Length	Ends	Spacing	Water	Rough	Infill	Thick	ILA	λ	Litho	Strength	Comments
20	JN	60	335	10		A	2	3	KL	0	A	0	MG	R5	Metagabbro well foliated
30	JN	55	310	500		H	2	2	KL	400	M	200	MG	R5	Metagabbro well foliated
20	JN	60	145	115		I	2	2	KL	10	M	100	MG	R5	Metagabbro well foliated
62	JN	87	199	100		F	2	3	KL	10	L	40	MG	R5	Metagabbro well foliated
85	JN	33	181	35		D	2	3	KL	1	G	5	MG	R5	Metagabbro well foliated
108	JN	20	21	200		H	2	3	KL	50	M	100	MG	R5	Metagabbro well foliated
204	JN	82	57	60		E	2	3	KL	1	I	10	MG	R5	Metagabbro well foliated
266	JN	73	297	130		H	2	3	KL	3	M	100	MG	R5	Metagabbro well foliated
295	JN	80	9	100		F	2	3	KL	2	G	5	MG	R5	Metagabbro well foliated
376	JN	66	382	150		G	2	3	KL	20	J	20	MG	R5	Metagabbro well foliated
416	JN	60	341	600		J	2	3	KL	10	M	100	MG	R5	Metagabbro well foliated
470	JN	86	274	130		G	2	3	KL	5	I	10	MG	R5	Metagabbro well foliated
500	JN	86	284	50		E	1	4	KL	1	G	3	MG	R5	Metagabbro well foliated
538	JN	84	113	200		D	2	1	KL	3	A	0	MG	R5	Metagabbro well foliated
557	JN	56	327	600		H	2	3	KL	10	M	100	MG	R5	Metagabbro well foliated

Appendix 12: Data from scanline 4.

Distance	Type	Dip	Dip/D	Length	Ends	Spacing	Water	Rough	Infill	Thick	ILA	λ	Litho	Strength	Comments
20	JN	83	32	40		D	1	2	KL	1	20		MG	R5	Metagabbro, mafic, fine grained, good foliation
30	JN	83	32	45		D	1	2	KL	1	20		MG	R5	Metagabbro, mafic, fine grained, good foliation
50	JN	85	34	50		A	1	2	KL	1			MG	R5	Metagabbro, mafic, fine grained, good foliation
52	JN	85	34	50		A	1	1	CA	1			MG	R5	Metagabbro, mafic, fine grained, good foliation
54	JN	85	34	50		A	1	1	CA	1			MG	R5	Metagabbro, mafic, fine grained, good foliation
56	JN	85	34	50		A	1	1	CA	1			MG	R5	Metagabbro, mafic, fine grained, good foliation
60	JN	85	34	50		A	1	1	CA	1			MG	R5	Metagabbro, mafic, fine grained, good foliation
75	JN	66	60	35		H	1	1	KL	1	30		MG	R5	Metagabbro, mafic, fine grained, good foliation
80	JN	50	35	25		G	2	2	KL	2	25		MG	R5	Metagabbro, mafic, fine grained, good foliation
95	JN	85	220	130		F	1	2	KL	2	50		MG	R5	Metagabbro, mafic, fine grained, good foliation
110	JN	80	40	100		D	2	2	KL		30		MG	R5	Metagabbro, mafic, fine grained, good foliation
118	JN	81	47	60		A	1	1	CA	1			MG	R5	Metagabbro, mafic, fine grained, good foliation
135	JN	85	23	50		A	2	2	CA	2	0		MG	R5	Metagabbro, mafic, fine grained, good foliation
156	JN	84	29	120		G	1	2	CA	2	20		MG	R5	Metagabbro, mafic, fine grained, good foliation
170	JN	80	34	400		H	2	3	KL	5	80		MG	R5	Metagabbro, mafic, fine grained, good foliation
174	JN	84	35	15		A	2	2	KL				MG	R5	Metagabbro, mafic, fine grained, good foliation
185	JN	82	39	20		D	2	3	CA		15		MG	R5	Metagabbro, mafic, fine grained, good foliation
192	JN	88	46	25		E	2	3	CA		10		MG	R5	Metagabbro, mafic, fine grained, good foliation
202	JN	74	26	70		D	2	4	CA	5	5		MG	R5	Metagabbro, mafic, fine grained, good foliation
235	JN	81	44	200		D	2	2	CA	20	10		MG	R5	Metagabbro, mafic, fine grained, good foliation
250	JN	86	48	60		G	1	2	CA	4	2		MG	R5	Metagabbro, mafic, fine grained, good foliation
267	JN	85	96	30		C	2	2	CA	1	10		MG	R5	Metagabbro, mafic, fine grained, good foliation
273	JN	81	289	100		E	1	2	CA	2	2		MG	R5	Metagabbro, mafic, fine grained, good foliation
287	JN	83	208	300		G	2	4	CA	10	10		MG	R5	Metagabbro, mafic, fine grained, good foliation
303	JN	77	14	40		G	2	4	CA	2	10		MG	R5	Metagabbro, mafic, fine grained, good foliation

Appendix 13: Data from scanline 5.

Distance	Type	Dip	Dip/D	Length	Ends	Spacing	Water	Rough	Infill	Thick	ILA	λ	Litho	Strength	Comments
22	JN	70	289	130		J	2	4	KL	5	M	110	MG	R4	Metagabbro light coloured, course grained
57	JN	78	271	400		L	2	3	KL	30	M	70	MG	R4	Metagabbro light coloured, course grained
75	JN	62	275	20		A	2	4	KL	0	G	5	MG	R4	Metagabbro light coloured, course grained
104	JN	80	115	80		D	2	4	KL	100	K	30	MG	R4	Metagabbro light coloured, course grained
116	JN	74	130	100		G	2	5	KL	0	J	20	MG	R4	Metagabbro light coloured, course grained
190	JN	76	278	10		D	2	5	KL	15	G	3	MG	R4	Metagabbro light coloured, course grained
205	JN	66	291	120		K	2	5	KL	50	K	30	MG	R4	Metagabbro light coloured, course grained
234	JN	75	326	40		G	2	4	KL	2	J	20	MG	R4	Metagabbro light coloured, course grained
240	JN	88	158	15		G	2	4	KL	2	I	10	MG	R4	Metagabbro light coloured, course grained
257	JN	42	294	125		I	2	4	KL	10	M	70	MG	R4	Metagabbro light coloured, course grained
265	JN	52	345	300		K	2	4	KL	20	M	120	MG	R4	Metagabbro light coloured, course grained
270	JN	49	335	100		H	2	5	KL	10	M	80	MG	R4	Metagabbro light coloured, course grained
298	JN	88	160	60		H	1	5	KL	5	I	10	MG	R4	Metagabbro light coloured, course grained

Appendix 14: Data from scanline 6.

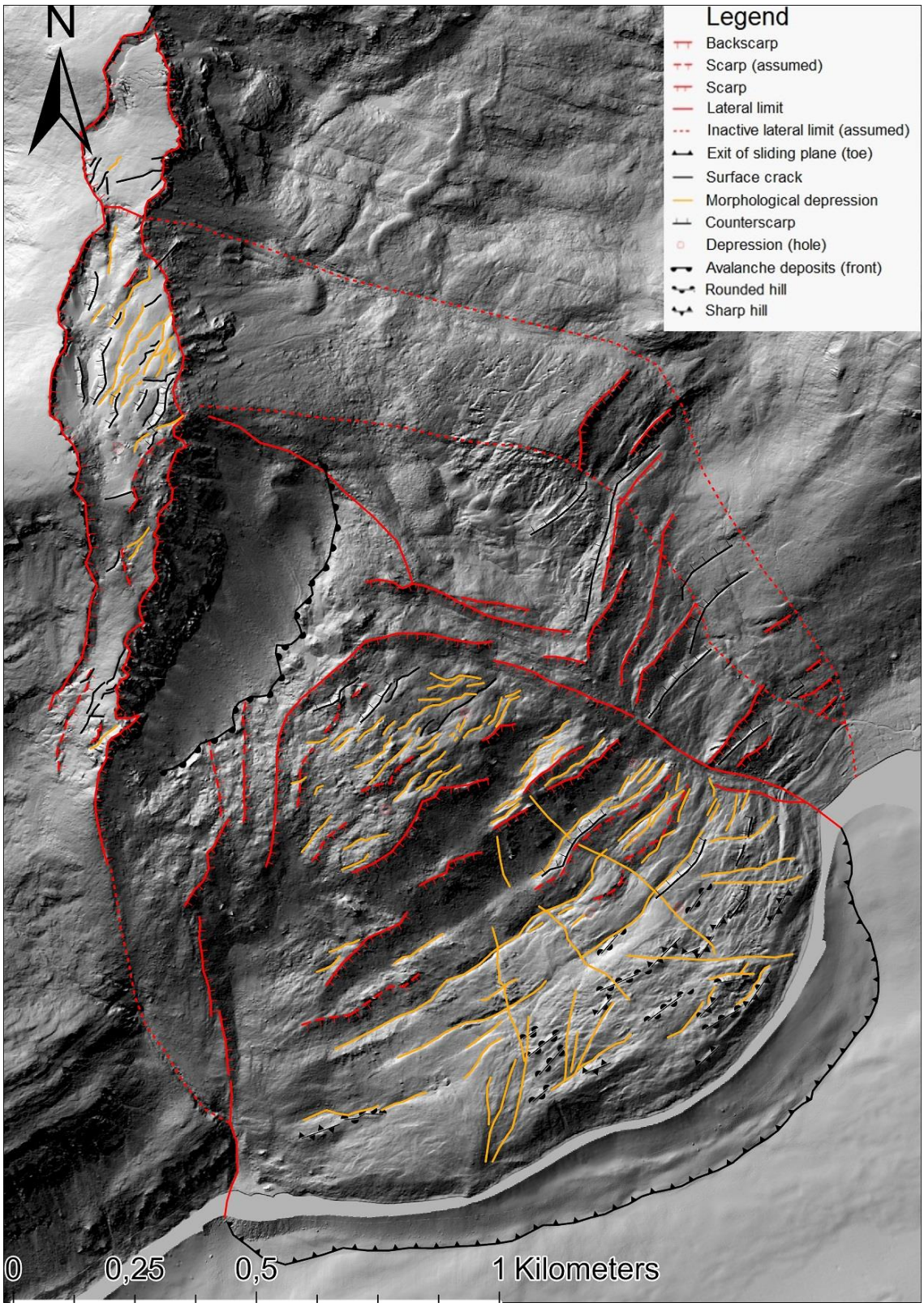

Appendix 15: Morpho-structural map. Hillshade from 1 m DEM (Kartverket, 2021).